Decoherence and Dynamical Decoupling of Shuttled Spins: towards Modelling of Ge Devices

by

Wiggert Vermeer

A thesis presented in partial fulfilment of the requirements for the degree of Master of Science in Quantum Information Science & Technology

Defense committee:	Dr. Miriam Blaauboer
	Dr. Maximilian Rimbach-Russ
	Dr. Viatcheslav Dobrovitski
Supervisors:	Dr. Viatcheslav Dobrovitski
	Yu-Ning Zhang, MSc

Delft, Netherlands
July 2, 2025

Abstract

Shuttling is expected to play a vital role in scaling up quantum computing based on semiconductor spin qubits. Decoherence, caused by interactions between the qubit and its environment, remains a major obstacle to maintaining qubit fidelity. For stationary qubits, decoherence is typically described using standard random processes. However, trajectories such as forth-back shuttling give rise to random processes with nontrivial correlations. We develop and benchmark a numerical method to analyse the effect of 3D random magnetic fields on shuttled spins, particularly relevant to Ge-based devices where the direction of the effective magnetic field varies significantly. Building on this, we design new dynamical decoupling (DD) sequences for shuttling, incorporating a central pulse to suppress the effect of mirror symmetry between the forward and backwards paths. Using realistic parameters for Si and Ge devices with the developed numerical method, we evaluate the effectiveness of DD sequences at suppressing decoherence during shuttling. In particular, we find that the XY8-Z sequence significantly improves fidelity during forth-back shuttling, and outperforms the standard XY8 sequence commonly used for stationary qubits.

Preface

Three years ago, as I was nearing the end of my Bachelors degrees, I came upon the dilemma of choosing to further pursue applied physics, or applied mathematics. This decision proved so challenging that I ended up spending a year doing neither. Fortunately, by the end of that year, a new path had emerged, one that aligned perfectly with my interests: anything quantum. This new path was the Master's programme Quantum Information Science & Technology. I have thoroughly enjoyed the opportunity to explore the whole quantum computing stack, as well as the chance to converse with a diverse group of students who also decided to embark on this adventure.

Now, nearing the end of this journey, I want to thank those who made it worthwhile. I am very grateful to my supervisor, Slava Dobrovitski, for making this project possible, and for his incredible support and enthusiasm throughout. I would also like to thank Yuning for always being open to provide feedback, share resources or simply listen. It is not an exaggeration when I say that the weekly meetings with Slava and Yuning were always a highlight of my week, and they consistently left me feeling energised and motivated.

I am very lucky to have had such a great group of fellow QIST students accompanying me on my journey. A Masters' programme and thesis are daunting ventures, so it's nice not to be alone. A special thanks to Julian, Priya, Rohan, Willow, Wout, and Zack. I wish you all the best of luck in finishing your own projects and hope that we keep in touch as our paths diverge.

Finally, a heartfelt thanks to my family, especially my parents, who have always shown enthusiastic support for anything I pursue, and made it possible for me to live life with the knowledge that if I fall, I will not fall far.

Contents

Chapter 1

Introduction

The ability to leverage the quantum properties of fundamental particles has the potential to allow novel methods in computing, communication, and sensing. Since the turn of the 21st century, significant progress has been made toward quantum applications on the basis of of different qubit platforms such as superconducting qubits [1], spin qubits in diamonds [2, 3], trapped ions [4], neutral atoms [5], and more. Within the field of quantum computing, the implementation of many useful algorithms will require a quantum computer with anywhere from thousands to millions of logical qubits, which translates to millions of physical qubits when error correction is included [6]. Current quantum processors have reached over 1000 qubits [7], a significant achievement, but still far from the millions of high-quality qubits with high-fidelity qubit operations that will be required.

Fidelity is a measure of the accuracy and reliability of qubits and qubit operations, and many factors will reduce fidelity, such as random effects or imperfect gate operations, which may lead to the system being unusable as a basis for quantum applications. Developing an understanding of how different factors affect qubit fidelity is important to improve the quality of a qubit platform. It is yet to be determined which qubit platform will prove most effective, and each platform has unique advantages and disadvantages for different applications. Research on improving these platforms focuses on increasing qubit coherence times, increasing gate fidelity, improving qubit connectivity, and pushing the fault tolerance threshold- all while also scaling up the number of qubits.

Among the possible qubit platforms, semiconductor spin qubits have become a leading contender for large-scale quantum computation due to their scalability, long coherence times, and compatibility with existing semiconductor technologies [8, 9]. In semiconductors, qubits are typically formed by confining electrons or holes in a quantum dot using electric potentials. In the early stages of research on quantum dots, gallium arsenide (GaAs) was the material of choice; however, over the past decade, silicon (Si) has emerged as the leading platform for quantum computing based on electrons in quantum dots. Electron spins in Si benefit from long coherence times, primarily due to a reduced hyperfine interaction resulting from a high abundance of net-zero nuclear spin isotopes, which can be further improved through isotopic enrichment. Significant progress has been made in Si-based qubits, including the demonstration of long coherence times [10], fast, high-fidelity gates [11], and "high-temperature" operation (above 1K) [12]. More recently, germanium (Ge) has emerged as a promising candidate for quantum computing, where hole spins are used

as a basis for qubits. Like Si, Ge benefits from net-zero nuclear spin isotopies, minimizing hyperfine-induced decoherence. In addition, the low effective mass of holes enables larger quantum dots, which relaxes fabrication restrictions [13]. Crucially, holes in Ge exhibit a strong intrinsic spin-orbit interaction. This feature enables fast, purely electrical operation of hole qubits without the need for the additional micromagnet used in Si to generate extrinsic spin-orbit coupling. Furthermore, in Ge, the g-tensor, which describes how the spin couples to magnetic fields via Zeeman splitting, will fluctuate in magnitude and direction.

When considering the scaling up of the number of qubits in quantum dot arrays, an important consideration is how to connect distant qubits. Two-qubit gates can occur between qubits via exchange coupling between neighbouring spins, but long-range interactions are more complex. One approach to enable two-qubit gates between distant qubits is to first shuttle the qubits between quantum dots, bringing them into the same vicinity and allowing them to interact. This approach can also be applied to quantum links between sparse qubit arrays [14]. Recent shuttling experiments in Si [15–17] and Ge [18] have demonstrated high shuttling fidelities, demonstrating the feasibility of this technique.

Both electrons in Si and holes in Ge suffer from decoherence due to noise present during shuttling. This noise may result from nuclear spins randomly located along the shuttling path, randomly flipping in time, or it may result from fluctuating charge defects leading to charge noise, which couples to the spin via spin-orbit coupling. These effects lead to a random magnetic field $\mathbf{B}(\mathbf{r}, t)$ acting on the spin, which varies in both time and space. For a *stationary* qubit, the random field can be described as a standard random process dependent only on time; however, during shuttling, the resulting random field is correlated both in time t and space $\mathbf{r}$. In Si, the direction of the effective magnetic field is almost uniform in space and time [19], meaning that longitudinal relaxation can be neglected and only dephasing occurs. However, in Ge, the variation of the g-tensor leads to a significant variation of the effective magnetic field. This means that we must account for both longitudinal and transversal relaxation, resulting in decoherence. Importantly, dephasing is a measure of purely transversal relaxation, while decoherence includes both transversal and longitudinal relaxation.

The effects of random magnetic fields on dephasing during shuttling have been studied previously [19–23]. However, the scenario involving a varying direction of the magnetic field with nontrivial correlations resulting from the chosen shuttling path has not been investigated. This consideration is particularly relevant to shuttling in Ge, where the anisotropic g-tensor causes significant variation in the effective magnetic field direction. Addressing this effect is an essential component of this thesis.

The suppression of decoherence is important when trying to increase the quality of qubits and qubit operations. There are various approaches, including the use of dynamical decoupling (DD), where well-timed pulses can refocus the spin, as well as encoding a logical qubit into multiple physical qubits to protect the logical state. The use of qubit encodings to increase shuttling fidelity is an approach that is expected to be effective for various encodings and shuttling procedures [19, 24]. However, sequences that have been very successful at suppressing decoherence in *stationary* qubits are expected to be less effective for *shuttled* qubits [25]. The ability to simulate and understand decoherence during shuttling allows the analysis

of the effectiveness of these decoherence mitigation techniques. We will analyse existing DD sequences as well as novel sequences designed for use during shuttling.

1.1 Thesis objectives

In this thesis, we model the random magnetic field along a shuttling path that varies in both magnitude and direction, as is the case in Ge. We asses a method to calculate the average effect of such a magnetic field, and benchmark the method's accuracy and performance under realistic circumstances. We apply this model to simulate decoherence during shuttling in situations where the direction of the magnetic field can vary significantly. Subsequently, we analyse the effectiveness of existing DD sequences, such as the XY4 and XY8 sequences, at suppressing decoherence in the case where there is noise along all three axes. We devise novel DD sequences designed for shuttling in which an X or a Z pulse is included halfway during an XY4/XY8 sequence. This pulse allows refocusing as the shuttled spin returns to its original point. These sequences are studied analytically using Average Hamiltonian theory, and subsequently simulated for an Si-based system with a strong preferred magnetic field direction. Finally, we simulate Ge-based systems where the magnetic field direction varies significantly.

Research on quantum technology is inherently interdisciplinary, which is reflected throughout this thesis. This work centres on using theoretical models to understand how fundamental physical principles manifest themselves at the level of material science & engineering as observable characteristics of decoherence. This requires not only an acute understanding of the underlying physics, but also on the mathematical methods used for studying these models analytically and numerically. The subsequent implementation of these methods requires a good understanding of coding principles. The limitations of the model must be critically assessed by considering practical aspects of semiconductor spin qubits, including material science engineering challenges related to device fabrication, and engineering challenges involved in applying operations on the spins. Finally, the overarching motivation is to reach high-fidelity spin shuttling, guided by an understanding of how such fidelities impact the feasibility of quantum algorithms.

1.2 Thesis structure

This thesis is structured as follows:

Chapter 2 discusses the basics of a qubit and how it evolves, followed by a description of electron and hole spins in semiconductors, with a focus on Si and Ge.

Chapter 3 introduces the Hamiltonian model used for a spin qubit undergoing shuttling, and key concepts required to understand the problems we address during the thesis.

In Chapter 4, we discuss known results on decoherence of qubits due to random effects, in order to develop familiarity with important concepts surrounding decoherence, random processes, and the random sheet required to understand decoherence

during shuttling.

In Chapter 5, we present methods used to numerically calculate the average effect of the random effects present in the model, and demonstrate numerical stability. We follow this with a discussion of certain limiting cases of the model for further verification.

Chapter 6 begins with the introduction of new DD sequences designed for shuttling, compared to existing DD sequences. These sequences are subsequently applied in simulations of forth-back shuttling in a Si-based system where the direction of the effective magnetic field is almost uniform along the shuttling path.

In Chapter 7, we perform similar simulations in a Ge-like environment where the direction of the effective magnetic field varies significantly along the shuttling path.

Finally, Chapter 8 concludes by summarising the results and outlining directions for future research.

Chapter 2

Spin qubits in semiconductor quantum dots

It is important to begin by developing an understanding of the systems that form the basis of the modelling performed in this thesis. This chapter dives into the physics required to understand the environment surrounding hole spin qubits. Firstly, an introduction to qubits and their operations is presented. Subsequently, the physics of electrons and holes in 2D semiconductor heterostructures is explained, with a focus on which factors will influence the decoherence of a spin used as a qubit. This will motivate the eventual model where the Hamiltonian acting on the qubit is considered as a 3D random magnetic field modelled as a random sheet. Throughout this thesis, we use the convention of $\hbar = 1$.

2.1 Qubits

Qubits form the basis for quantum information processing and can be defined by any two-level quantum system. In the cases of spin qubits, a principal example is an electron in the presence of a magnetic field. The two different spin states ($m_s = \pm\frac{1}{2}$) will experience Zeeman splitting according to the Hamiltonian

$$H_{Zeeman} = \mu_B g_0 B S_z, \tag{2.1}$$

where μ_B is the Bohr magneton, g_0 is the g-factor, and B is the strength of magnetic field. The axes have been chosen such that the magnetic field acts along the z-axis. This axis can be freely chosen due to the isotropy of the Zeeman splitting for a free electron. As a result of the magnetic field, the two previously degenerate spin states of the electron split and become nondegenerate, with an energy difference of $2\mu_B g_0 B$. These two states form the basis of a two-level system, usable as a qubit. The energy diagram is shown in Fig. 2.1(a). The two states are denoted by $|m_s\rangle = |+\frac{1}{2}\rangle \equiv |1\rangle$, $|m_s\rangle = |-\frac{1}{2}\rangle \equiv |0\rangle$. With these two energy levels as states, any pure state of a qubit can be written as a superposition given by

$$|\psi\rangle = \alpha|0\rangle + \beta|1\rangle = e^{i\delta}\left[\cos\left(\frac{\theta}{2}\right)|0\rangle + e^{i\phi}\sin\left(\frac{\theta}{2}\right)|1\rangle\right], \tag{2.2}$$

where δ is a global phase, θ encodes the relative magnitude of the two states, and ϕ encodes the relative phase. The state can be visualised on the Bloch sphere as seen

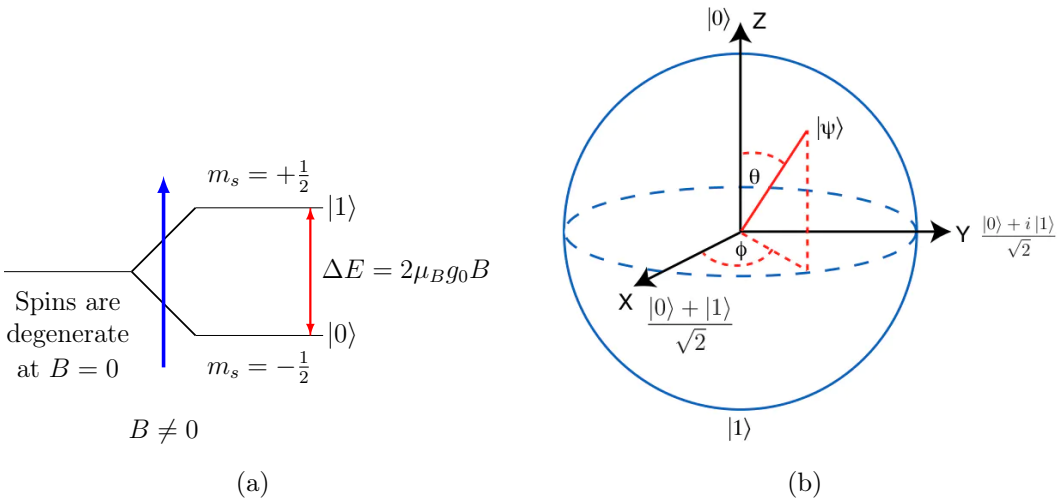

Figure 2.1: (a) Zeeman splitting of spin states. (b) Bloch sphere representation of a qubit. Image source: [26].

in Fig. 2.1(b). Changing the state of the qubit can be described as a rotation on the same Bloch sphere, using the rotation operator given by

$$R_{\hat{\boldsymbol{n}}}(\theta) = \exp\left[-i\theta(\hat{\boldsymbol{n}} \cdot \boldsymbol{\sigma})\right], \tag{2.3}$$

where $\hat{\boldsymbol{n}} \cdot \boldsymbol{\sigma} = n_x\sigma_x + n_y\sigma_y + n_z\sigma_z$ such that $\hat{\boldsymbol{n}}$ is a unit vector describing the axis of rotation, θ is the rotation angle, and the Pauli operators are

$$\sigma_x = \begin{pmatrix} 0 & 1 \\ 1 & 0 \end{pmatrix}, \quad \sigma_y = \begin{pmatrix} 0 & -i \\ i & 0 \end{pmatrix}, \quad \sigma_z = \begin{pmatrix} 1 & 0 \\ 0 & -1 \end{pmatrix}. \tag{2.4}$$

A Hamiltonian is used to describe the different effects acting on a quantum state and determines energy. Under the influence of a Hamiltonian, a state will evolve from an initial state to a final state according to

$$|\psi(t)\rangle = U(t)|\psi(0)\rangle, \quad U(t) = \mathcal{T}\exp\left(-i\int_0^t H(s)ds\right), \tag{2.5}$$

where $U(t)$ is the evolution operator. $\mathcal{T}$ is a time-ordering operator required in cases where $[H(s), H(s')] \neq 0$, i.e., if the Hamiltonian does not commute with itself at different times. If $[H(s), H(s')] = 0\ \forall s, s' \in [0, t]$, then the time ordering becomes trivial. The key concept to carry through to future chapters is the concept that a qubit is a two-level system that can be visualised on a Bloch sphere, and when considering operations acting on the single qubit, we can visualise them as rotations along the surface of this sphere.

2.2 Electron and hole spins in semiconductors

In this section the physics of electrons and holes in semiconductors (in particular 2D heterostructures) are outlined, with a goal that is twofold. Firstly, we define the manner in which a qubit is defined for Si and for Ge devices, based on their bands. Secondly, we consider the physical environment of the spin undergoing shuttling,

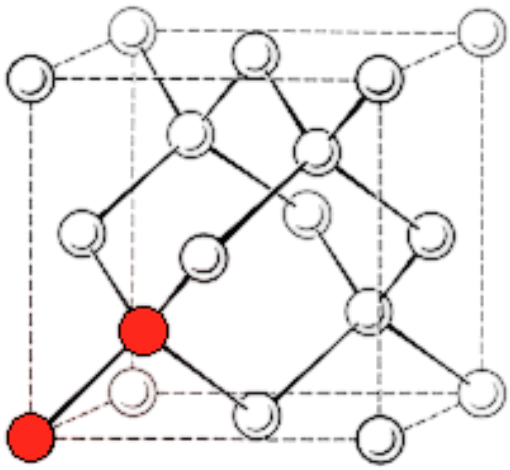

Figure 2.2: Diamond lattice. Red circles denote basis atoms. Image sourced from [28].

and which give context to the phenomena which lead to random effects acting on the spin, leading to decoherence.

2.2.1 Band structure

Si and Ge crystals both have the same diamond structure, which is based on an face-centred cubic Bravais lattice with a basis of two atoms at [000] and $[\frac{1}{4}\frac{1}{4}\frac{1}{4}]$, shown in Fig. 2.2 [27]. This structure has a cubic symmetry.

The bands that are of most interest are those at the band gap, specifically at the conduction band edge and the valence band edge. The energy bands of Si and Ge are shown in Fig. 2.3. For Si, the conduction band minimum is at the point $\mathbf{k} = \frac{2\pi}{a}[0.86, 0, 0]$ along the vector [1 0 0] and five other equivalent points due to the cubic symmetry, resutling in six equivalent minima. In Ge, the conduction band edges are at $\mathbf{k} = \frac{\pi}{a}[1, 1, 1]$, resulting in four equivalent minima per cell (one in each corner of the cube and compensating for overlap with other cells). For both Si and Ge, the valence band edge is at the Γ point at $\mathbf{k} = 0$, the centre of the Brillouin zone. The valence band edge is derived from the atomic p-like orbitals (p_x ,p_y, p_z) and is six-fold degenerate in the absence of spin-orbit coupling, due to the combination of orbital (threefold) and spin (twofold) degeneracies. In the next subsection, the lifting of these degeneracies will be discussed.

In Si, qubits are generally defined using electrons in the conduction band, which has six equivalent minima. Therefore, for bulk Si, there are twelve degenerate states (after including the two-fold spin degeneracy). To use an electron as a qubit, we require two states with distinct energies, and the other states to have a high enough energy separation to avoid leakage. The valley degeneracy contributes to complications in qubit energy levels and coherence. We discuss the separation of these states when we continue with quasi-2D structures.

For Ge, qubits are generally defined using holes at the valence band edge, where although there are no equivalent minima, there is the degeneracy of the p-like orbital to deal with. These will be split by including the effect of spin-orbit coupling, and subsequently considering quasi-2D structures.

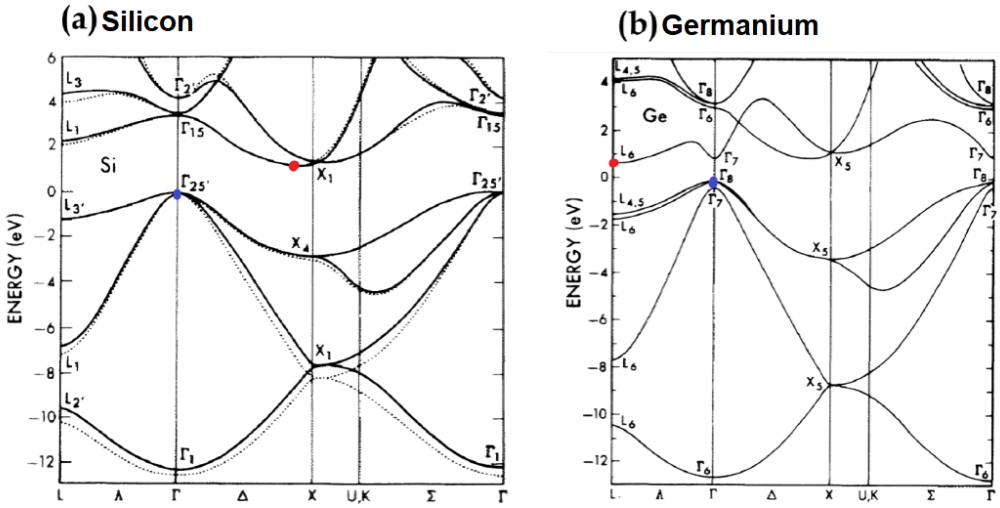

Figure 2.3: Electronic band structures of **(a)**: Si and **(b)**: Ge, plotted along high-symmetry directions in the Brillouin zone. In both materials, the valence band edge occurs at the Γ point (blue). In Si, the conduction band edge (red) occurs along the Δ direction near the X-point. In Ge, this is at the L-point. The numbering labels (Γ_i, X_i, L_i) are symmetry labels denoting crystal symmetry states for corresponding energy states. Image adapted from [29], via [30].

2.2.2 Role of spin-orbit coupling

Spin-orbit coupling is a relativistic correction, which leads to the quantum numbers l and s no longer being "good" quantum numbers, which requires a description in terms of the total angular momentum $J = L + S$. The effect of spin-orbit coupling can be derived from the Dirac equation and results in the following term in the Hamiltonian [31]:

$$H_{SO} = \delta_{SO}\mathbf{L} \cdot \mathbf{S}, \tag{2.6}$$

where $\mathbf{L}$ is the orbital angular momentum operator, and δ_{SO} determines the strength of the spin-orbit coupling. In general, larger nuclei lead to a higher δ_{SO} [32]. For the s-like conduction band edge where $l = 0$, $\delta_{SO} = 0$. For the valence band states for which $l = 1$, the spin-orbit coupling leads to the splitting of the six degenerate states based on their total angular momentum quantum number j, where $j = l \pm \frac{1}{2}$ and $m_j \in \{-j, ..., j\}$. These can be grouped into the following:

$$\text{Heavy Holes} : |j\ m_j\rangle = |\frac{3}{2}\ \pm \frac{3}{2}\rangle \tag{2.7}$$

$$\text{Light Holes} : |j\ m_j\rangle = |\frac{3}{2}\ \pm \frac{1}{2}\rangle \tag{2.8}$$

$$\text{Split off band} : |j\ m_j\rangle = |\frac{1}{2}\ \pm \frac{1}{2}\rangle \tag{2.9}$$

At $\mathbf{k} = 0$, the heavy holes and the light holes have the same energy E_0, while the split-off band is at a lower energy, with energy difference $\Delta_0 = 3\delta_{SO}/2$ [33]. This term is called the spin-orbit gap. For Ge, $\Delta_0 \approx 0.3$ eV, while for Si it is only 0.044 eV. Therefore, spin-orbit coupling is a much more important consideration in

Ge than in Si. Near the valence band edge, after projection on the subspace of the relevant states, the hole states can be described by the *Luttinger-Kohn* Hamiltonian in the spherical approximation [33–35]:

$$H_{LK} = -\frac{1}{2m_0}\left[\left(\gamma_1 + \frac{5}{2}\gamma_s\right)k^2 - 2\gamma_s(\mathbf{k}\cdot\mathbf{J})^2\right], \tag{2.10}$$

where $k^2 = \mathbf{k}\cdot\mathbf{k}$, m_0 is the free electron mass, and $\gamma_1, \gamma_2, \gamma_3$ and $\gamma_s = (2\gamma_2 + 3\gamma_3)/5$ are material-dependent Luttinger parameters. Parameter values for different semiconductors can be found in [36]. In the case of cubic symmetry rather than spherical symmetry, there is an extra invariant term quadratic in $\mathbf{k}$, leading to eigenvalues which are dependent on the direction of $\mathbf{k}$. For Ge, the anisotropy of the isoenergetic surface is rather weak, so the spherical approximation is feasible [34]. For crystal lattices without a centre of inversion (such as GaAs), another term linear in $\mathbf{k}$ needs to be considered, though this term is usually small.

Using the basis of the eigenstates of $J_z = \{|\pm\frac{3}{2}\rangle, |\pm\frac{1}{2}\rangle\}$, Eq. (2.10) can be written in matrix form as

$$H_{LK} = \frac{1}{2m_0}\begin{pmatrix} P+Q & L & M & 0 \\ L^* & P-Q & 0 & M \\ M^* & 0 & P-Q & -L \\ 0 & M^* & -L^* & P+Q \end{pmatrix}, \tag{2.11}$$

where

$$P = -\gamma_1 k^2, \tag{2.12}$$
$$Q = \gamma_s(2k_z^2 - k_x^2 - k_y^2), \tag{2.13}$$
$$L = 2\sqrt{3}\gamma_s k_z(k_x - ik_y), \tag{2.14}$$
$$M = \sqrt{3}\gamma_s(k_x - ik_y)^2. \tag{2.15}$$

The matrix form makes explicit that there is no coupling between the two HH states, but there is mixing between the LH states and the HH states. Neglecting this coupling by setting $k_x = k_y = 0$, the energies of the pure heavy holes and light holes can be approximated as

$$E_{HH} = \frac{-k^2}{2m_{HH}}, \quad m_{HH} = \frac{m_0}{\gamma_1 - 2\gamma_s}; \tag{2.16}$$
$$E_{LH} = \frac{-k^2}{2m_{LH}}, \quad m_{LH} = \frac{m_0}{\gamma_1 + 2\gamma_s}. \tag{2.17}$$
$$\tag{2.18}$$

In Ge, $\gamma_1 \approx 13$ and $\gamma_s \approx 5$ [33], resulting in $m_{HH} \approx 0.33m_0$ while $m_{LH} \approx 0.04m_0$, hence the heavy and light hole denomination.

2.2.3 Quasi-2D systems

The previous analysis has been for bulk Ge and Si, where there is cubic symmetry of the crystal. However, in a planar heterostructure, electrons/holes are confined to a quantum well layer, which results in a strong confinement in the z-direction.

The difference between a bulk structure and a planar heterostructure is illustrated in Fig. 2.4. The plane will be pure Si or Ge, while the layers on either side are SiGe alloys. The resulting system can be considered a quasi-2D system, where cubic symmetry is broken but in-plane symmetry is maintained.

For electrons in Si, the six-fold degenerate minima are split. Assuming a confinement along the [0 0 1] direction, the degeneracy splits into a two-fold degenerate ground state along $\pm\hat{k}_z$ and a four-fold degenerate state containing the four $\pm\hat{k}_x, \pm\hat{k}_y$ states at a higher energy. This is due to electrons with a different effective mass in the out-of-plane and in-plane directions [37, 38]. The two lower states further mix in the presence of disorder, and are subsequently split by an energy gap Δ_{VS} called the valley splitting [38]. As a result, there is a lowest energy state with two-fold spin degeneracy. This state can be split using a magnetic field to obtain two levels usable as a qubit. The size of Δ_{VS} is typically comparable to the Zeeman energy of electron spins in Si, which means that dealing with the interaction between these valley states is important to achieving good quality electron spin qubits in Si [39].

For holes in Ge, the degenerate states also split. The resulting eigenstates of the confined system are not identical to the original HH and LH states, however, due to the strong confinement in the z direction, the wave vector k_z will generally be much larger than the in plane wave vector $k_\parallel$, so the eigenstates are very close to the bulk LH and HH eigenstates. In the approximation of pure HH & LH states where coupling between HH states and LH states is neglected, there is splitting even at the valence band edge. In this approximation, the HH and LH dispersion relations are given by

$$E_{n_{HH}} = -\frac{1}{2m_0}\left(\frac{\pi^2 n_{HH}^2(\gamma_1 - 2\gamma_s)}{L_z^2} + (\gamma_1 + \gamma_s)k_\parallel^2\right), \tag{2.19}$$

$$E_{n_{LH}} = -\frac{1}{2m_0}\left(\frac{\pi^2 n_{LH}^2(\gamma_1 + 2\gamma_s)}{L_z^2} + (\gamma_1 - \gamma_s)k_\parallel^2\right), \tag{2.20}$$

where $k_\parallel^2 = k_x^2 + k_y^2$, and k_z has been quantised as $k_z^2 = \pi^2 n^2 / L_z^2$, assuming a hard wall confining potential, with n the subband index and L_z the width of the quantum well. There is splitting between the HH and LH states even at $k_\parallel = 0$ with an energy difference of

$$\Delta E_{LH-HH} = \frac{2\gamma_s \pi^2}{m_0 L_z^2}. \tag{2.21}$$

Furthermore, the in-plane effective masses of the HH and LH states are now $m_\parallel^{HH} = m_0/(\gamma_1+\gamma_s) \approx 0.055 m_0$ and $m_\parallel^{LH} = 0.125 m_0$. The light holes have a *heavier* effective mass. The exact values of the effective mass will depend on exact details such as strain, but in general, calculations and experimental results have confirmed the in-plane effective mass of about $0.05 m_0$ [33]. The low effective mass allows for larger quantum dots, thereby relaxing fabrication requirements [13]. Fig. 2.4 shows a diagram of the dispersion relations of the HH/LH states in Eqs. (2.19)-(2.20) Due to the lower effective mass of the HH band, it has a higher curvature, leading to it crossing over the LH band. When coupling between the bands is included, anticrossings appear in the dispersion relations [32]. Fig. 2.4 shows how the sixfold degenerate state at the valence band edge is separated into three separate bands

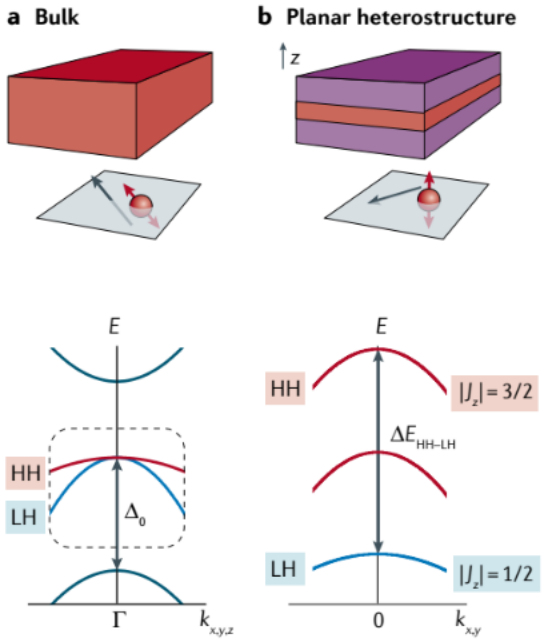

Figure 2.4: Illustration of bulk structures and planar heterostructures and their associated bands. **a**: A bulk structure is highly isotropic, leading to an invariance between x, y, and z directions. The HH-LH bands are illustrated as being split off from the split-off band due to the spin-orbit coupling. The LH band has a higher curvature due to its smaller effective mass. **b**: In a planar heterostructure, there is a difference between the in-plane and out-of-plane behaviour. The HH-LH band splits, with the HH band being higher energy level. Due to the HH states now having a smaller effective mass, their curvature is higher. Image sourced from [33].

due to the inclusion of the effect of spin-orbit coupling, followed by the inclusion of confinement in a planar heterostructure.

An additional facet that will affect the band energy levels is strain. The lattice parameters of Si and Ge are comparable; however, the small lattice mismatch leads to a compressive strain in the well, leading to the addition of a term to the Hamiltonian, which adds to the HH-LH splitting. This is described by the Luttinger-Kohn-Bir-Pikus Hamiltonian [40].

2.2.4 Rashba effect

The current HH state still exhibits spin degeneracy. Similar to electrons, this degeneracy is usually lifted by applying a magnetic field which breaks time inversion symmetry and results in Zeeman splitting. Spatial inversion asymmetry will also lift the spin degeneracy of the HH and LH states. Spatial inversion asymmetry will come either from structure inversion asymmetry (SIA) due to the confinement potential, or from bulk inversion asymmetry (BIA) due to the crystal structure. Due to the cubic structure of Ge and Si, BIA will not apply. SIA is commonly referred to as Rashba spin-orbit interaction, and will arise due to the asymmetric electric fields imposed on the quantum dot, which confine the spin. Due to being dependent on the local electric field, this effect will lead to nonconstant energy levels at different points in the structure [41]. The Hamiltonian that describes this effect at

the valence band edge is [32, 42]

$$H_R = \alpha_R(k_y J_x - k_x J_y), \tag{2.22}$$

where the weaker contribution due to $\mathcal{J} = (J_x^3, J_y^3, J_z^3)$ has been neglected, and the confining electric field is pointed along the z-axis. This term does not couple the HH states directly, only indirectly via the HH-LH coupling and the LH-LH coupling. This means that the HH-HH coupling is essentially a higher-order effect, being cubic in $k_\parallel$ rather than linear [32].

2.2.5 Zeeman splitting

For electrons in Si, the Zeeman splitting can be effectively described by the free-electron Zeeman Hamiltonian in Eq. (2.1), with a position-dependent effective g-factor. This enables the splitting of the lowest energy valley state by their spin, forming a two-level system which can be used as a qubit.

For a 2D hole system, the Zeeman splitting due to a magnetic field $\mathbf{B}$ is given by

$$H_Z = \kappa \mathbf{B} \cdot J + 2q\mathbf{B} \cdot \mathcal{J}, \tag{2.23}$$

where κ, q are Luttinger parameters. The first term is isotropic with an effective g-factor κ, while the second term is anisotropic, with q generally two orders of magnitude smaller than κ, and as such can be neglected. [32, 42]. For Ge, $\kappa = 3.41$, $q = 0.06$. The g-tensor manifests itself when restricting this Hamiltonian to the HH-subspace, where the Zeeman Hamiltonian is written as

$$H_{Z,HH} = \mathbf{B} \cdot \overleftrightarrow{g} \cdot \boldsymbol{\sigma}, \tag{2.24}$$

where $\boldsymbol{\sigma} = (\sigma_x, \sigma_y, \sigma_z)$ is a vector of Pauli matrices acting on the HH subspace. The component g_{ij} of the g-tensor represents how large the spin splitting is in the direction j when a magnetic field is applied along the direction i. Depending on details of the semiconductor structure and the confinement potentials, the g-tensor can be highly anisotropic, meaning the energy splitting is dependent on the direction of the magnetic field. Furthermore, the g-tensor may change at different points in the semiconductor, due to local charge variation. This enables charge noise to affect the spin, adding to decoherence. This anisotropy has been investigated theoretically for holes in Si [42], as well as experimentally in Ge [43].

2.2.6 Modelling anisotropic Zeeman splitting

We conclude this chapter by performing simulations of the energy level splitting of the HH states, depending on the orientation of an applied magnetic field. This will give an illustration of the anisotropy and variation of the g-tensor. We illustrate this using the Hamiltonian

$$H = H_{LK} + H_R + H_Z, \tag{2.25}$$

where the component Hamiltonians are given by Eqs. (2.10), (2.22), and (2.23) respectively. Fig. 2.5 shows the resulting energy level splitting for two different sets of wave vectors representing two spins, depending on the orientation of the magnetic

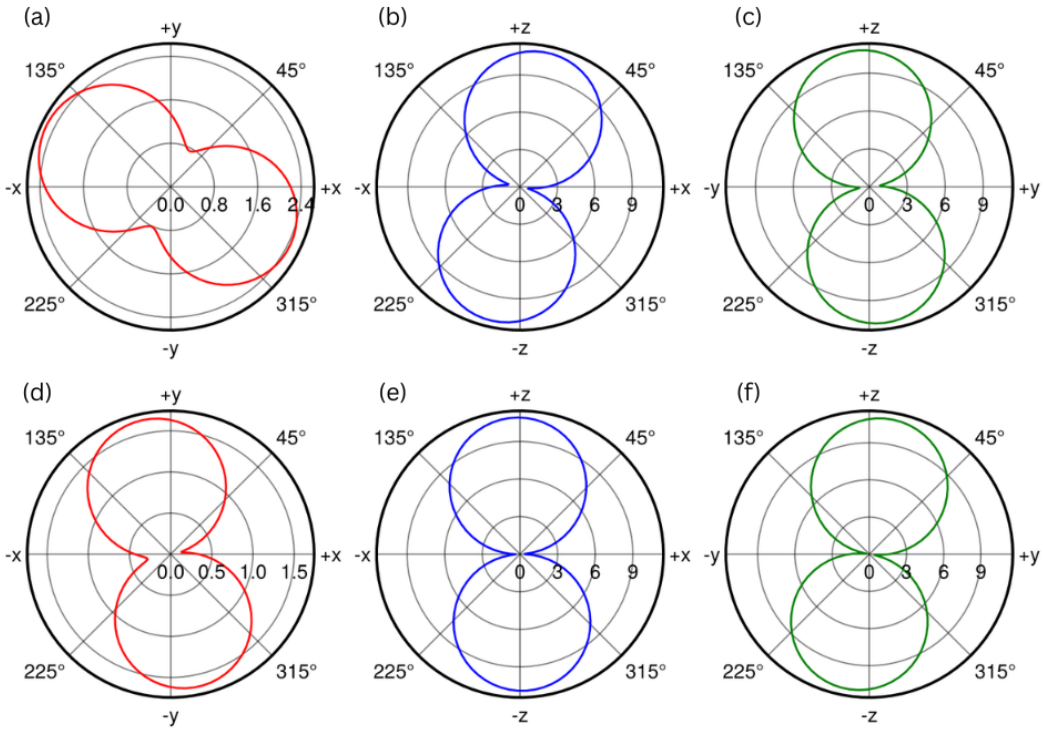

Figure 2.5: Plots representing the energy splitting depending on the orientation of an applied magnetic field, based on Eq. (2.25). In all figures, $m_0 = 1$, $\alpha_R = 100$, $|\mathbf{B}| = 1$. In columns from left to right, the orientation of the magnetic field is in the x-y plane, x-z plane, and the y-z plane respectively, with the magnetic field in the i-j plane being given by $B_i = |\mathbf{B}|\cos(\theta)$, $B_j = |\mathbf{B}|\sin(\theta)$, with $\theta \in [0, 2\pi)$. (a), (b), (c): $k_x = 10,\ k_y = -5,\ k_z = 50$, (d), (e), (f): $k_x = -3,\ k_y = 15,\ k_z = 100$.

field. We see that the splitting is largest when the magnetic field is oriented along the z-axis, and smaller when oriented in plane, representing the anisotropy. Even in-plane, the splitting is very anisotropic for both spins. For the two spins, the splitting shape varies significantly, especially in-plane. This represents how the g-tensor will vary at different points in a planar heterostructure. The values chosen for these simulations were chosen with the goal of illustration and not accurate simulation of the relevant structures. Measurements of the g-tensor for a Ge device show results that are visually very similar to these simulations [43].

We have discussed the qubit implementations in Si and Ge. In Si, confinement and valley splitting lead to a lowest energy conduction band, which can be split into a two-level system by applying a magnetic field, which can be used as a basis for the qubit. For Ge, spin-orbit coupling and confinement split the degenerate hole states at the valence band edge, leading to a lowest energy heavy hole state. A qubit is subsequently defined in the two-level system formed by applying a magnetic field. We now to turn to discussing the decoherence of these qubits during shuttling.

Chapter 3

Shuttled qubits

This chapter will introduce the main problem studied in this thesis: Decoherence during shuttling. We will introduce our model, discussing differences between Si and Ge, and how we model the random effects affecting the spin during shuttling. We will also discuss the difference between dephasing and decoherence, and how dynamical decoupling can be used to suppress decoherence. Throughout we will identify key differences between *stationary* qubits, which have been studied extensively, and *shuttled* qubits, which are more recently explored and present unique theoretical challenges.

3.1 Hamiltonian for a shuttled spin qubit

In this thesis, we consider conveyor-belt type shuttling of a spin along a one-dimensional channel of length L. At $t = 0$, a spin is loaded into the channel to $x = 0$, after which it is transported to the end of the channel at $x = L$ for a duration T. The shuttled spin forms a tightly localised wave packet whose carrier density is $\rho(\mathbf{r}, x_c)$ where x_c is the centre of the wave packet. The effective interaction between the spin and its environment can be described by the effective Hamiltonian

$$H_Z(x_c) = \mu_B S_z \left[\int g(\mathbf{r}) B_Q \, d^3\mathbf{r} + \int g_0 B_{\text{hf}}(\mathbf{r}) \rho(\mathbf{r}; x_c) \, d^3\mathbf{r} \right] \tag{3.1}$$

where $g(\mathbf{r})$ is the position-dependent effective g-factor of the carrier. We distinguish between the effect of interaction of the position-dependent g-factor with the quantising magnetic field B_Q, and the effect of the hyperfine splitting B_{hf}. We restrict ourselves to splitting along the z-axis, which is applicable to electrons in Si, where we assume that the direction of the effective magnetic field is almost uniform in space and time.

In an ideal system, the shape of the wave packet will stay constant, but in reality this is not the case. This is due to position-dependent material properties along the shuttling channel and charge defects affecting the electrostatic potential, which affect the shape of the confining potential and the shape of the wave packet. These effects result in a wave packet that is not only non-constant in space but is also dependent on time. Furthermore, the nuclear spin flip-flops make the hyperfine interaction time dependent as well, resulting in an effective Zeeman splitting given by

$$H_Z(x_c,t) = S_z \int d^3\mathbf{r}\ \mu_B[g(\mathbf{r})B_Q + g_s B_{\text{hf}}(\mathbf{r},\mathbf{t})]\rho(\mathbf{r},t;x_c) \tag{3.2}$$

This can be more familiarly written as

$$H_Z(x_c,t) = g_0\mu_B\left[B_0(x_c) + \tilde{B}(x_c,t)\right] S_z \tag{3.3}$$

where we distinguish between the deterministic magnetic field $B_0(x_c)$, and the random effective field $\tilde{B}(x_c,t)$. We will adopt natural units such that $g_0\mu_B = 1$

For holes in Ge, due to the anisotropy of the g-tensor, we must account for significant spatial variation of the direction of the effective magnetic field, which leads to the Hamiltonian

$$H_Z(x_c,t) = \left(\mathbf{B}_0(x_c) + \tilde{\mathbf{B}}_{\text{eff}}(x_c,t)\right)\cdot\mathbf{S} \tag{3.4}$$

where the g-tensor and magnetic field $\mathbf{B}$ in the heavy-hole Zeeman Hamiltonian described by Eq. (2.24) combine to give effective magnetic fields $\mathbf{B}_0$ and $\mathbf{B}_{\text{eff}}$. Analysing this model is more difficult due to the varying quantisation axis due to $\mathbf{B}_0$ and the noise in along all three axes due to $\tilde{\mathbf{B}}_{\text{eff}}$.

3.2 Dephasing & Decoherence

A powerful approach to studying the decoherence of *stationary* qubits is to model random magnetic fields as a random process. If we consider a single shuttling experiment of duration T along a path $x = x_c(t)$, the spin will have evolved according to

$$U(T) = \exp\left(-i\int_0^T H_Z(x_c(t),t)dt\right) \tag{3.5}$$

$$= \exp\left(-iS_z\left[B_0T + \int_0^T \tilde{B}(t)dt\right]\right) \tag{3.6}$$

$$= \exp(-i\alpha - i\phi(T)) \tag{3.7}$$

resulting in a deterministic phase $\alpha = B_0T$, and a random phase $\phi(T) = \int_0^T \tilde{B}(t)dt$. The deterministic phase α will be the same for every experiment, and can be accounted for by performing an appropriate rotation operator which negates the contribution of the deterministic field. The random phase ϕ cannot be accounted for as it will be different for every instance of $\tilde{B}(t)$. This means that after an experiment, the spin will have acquired some additional random phase ϕ, reducing its fidelity relative to the desired space. Although we cannot determine the exact random phase, we can calculate its average in the form of a dephasing factor. This is a useful indicator of, on average, how much the resulting state deviates from the desired state. Averaging over all possible realisations of $\tilde{B}(t)$ leads to a reduction of the off-diagonal elements of the density matrix by the dephasing factor

$$W(T) = \mathbb{E}\left[\exp(-i\phi(T))\right] \tag{3.8}$$

where $\mathbb{E}$ denotes the expected value. This dephasing factor quantifies, on average, how far the final state deviates from the initial state under the influence of a random magnetic field, after accounting for the deterministic phase.

Pure dephasing only applies when the random magnetic field is along only one axis and results in the phase (ϕ in (Eq. 2.2)) being randomised, as it is different in every realisation of the magnetic field. This can also be called transversal relaxation. During *pure dephasing*, a state on the equator of the Bloch sphere will stay on the equator of the Bloch sphere.

Decoherence includes both transversal *and* longitudinal relaxation, and occurs when the random magnetic field acts along all axes. This leads to an expected average rotation, and each realisation deviates from this average rotation, with the resulting state being anywhere on the surface of the Bloch sphere. The dephasing factor does not capture all of the relaxation that has occurred. Instead, we must use a decoherence factor that captures all of the relaxation.

The Hamiltonian describing the spin decoherence in Ge in Eq. (3.4) has a random magnetic field along all axes, and therefore we must look at *decoherence* rather than *dephasing*. Calculating decoherence for this Hamiltonian faces two important issues: Firstly, the deterministic component of the Hamiltonian does not commute with the random component, meaning that we cannot separate contributions of the deterministic magnetic field and the random magnetic field to the evolution. Secondly, the Hamiltonian does not commute with itself at different times, making the total evolution more difficult to analyse. These concepts make analysing decoherence for Ge much more difficult, where the direction of the effective magnetic field can vary significantly. Since there is no existing method to calculate the average effect of a Hamiltonian like Eq. (3.4), we are compelled to devise a method for numerically calculating the average effect, which we discuss in Chapter 5.

A decoherence factor can be obtained as follows. Firstly, we define the average projection of the final along the x-axis given by when a spin with initial state $|\psi\rangle = |+\rangle \ = \frac{1}{\sqrt{2}}(|0\rangle + |1\rangle$, $\rho_0 = \frac{1}{2}\begin{pmatrix} 1 & 1 \\ 1 & 1 \end{pmatrix}$, is allowed to evolve by a magnetic field, resulting in

$$W_x(T) = 2\mathbb{E}\left[\mathrm{Tr}\left(\rho_0 {U^\dagger}_\beta(T) S_x U_\beta(T)\right)\right] \tag{3.9}$$

where the $U_\beta(T)$ is the evolution operator for a single realisation of the magnetic field $\beta(t)$. We can similarly define $W_y(T)$ and $W_z(t)$ with the same ρ_0 but instead the projection along the y and z axes. The decoherence factor is given by

$$W = \sqrt{W_x^2 + W_y^2 + W_z^2} \tag{3.10}$$

It can be understood intuitively as follows: the random magnetic field acting along all axes will lead to an expected rotation, with each realisation deviating slightly from this rotation. Each individual resulting state will have a total projection of 1. However, if we average the projections along x, along y, and along z separately, and then calculate the total projection, the result may be less than 1. The visualisation behind this is that the average state of many points on the surface of a sphere does not lie on the surface of the sphere, but inside the sphere. The distance from the centre of the sphere to this average point quantifies the decoherence.

An alternative measure is the average fidelity defined as

$$F = \mathbb{E}\left[|\langle\psi|U_\beta|\psi\rangle|^2\right] \tag{3.11}$$

$$= \frac{1}{3} + \frac{1}{6}\mathbb{E}\left[|\mathrm{Tr}(U_\beta)|^2\right] \tag{3.12}$$

which averages over all possible initial state. A proof of this identity is provided in Appendix A.3. The two measures are closely related, however the advantage of the decoherence factor is that any deterministic rotation will not reduce decoherence, but will reduce fidelity (if not accounted for). For average fidelity, the deterministic rotation can be accounted for in the case that the magnetic field is only along one axis, by performing the appropriate inverse rotation. The angle of rotation is the shuttling duration multiplied by the strength of the magnetic field, and the rotation axis is the same direction as the magnetic field. However, when the deterministic magnetic field varies, determining the deterministic rotation is not as easy. Nevertheless, the average fidelity has the advantage that the results are not particular to one initial state. We will consider both measures in Chapter 6 and 7.

3.3 Magnetic field as a random process

For *stationary* qubits, the magnetic field is often modelled as a random process with favourable properties such as being Gaussian, stationary, and Markovian. These properties derive from considering the spin in a very large bath of spins whose average effect is Gaussian. The large nature of the bath means that the back-action of the spin on the bath is negligible, implying an unchanging bath and therefore a stationary process. This assumption also leads to a reasonable candidate for noise being a Markov process, as only the current state of the bath and the spin will affect future dynamics. These properties together lead to the random process being reasonably modelled as an Ornstein-Uhlenbeck (OU) process. The details of random processes will be addressed in the next chapter, but for considering the behaviour of the random magnetic field during shuttling, it is useful to be aware that for a *stationary qubit*, the correlation of the random magnetic field correlation decays over time (exponentially in the case of an OU process).

During shuttling, we expect the random effects to be correlated in both time and space. This means that non-trivial shuttling paths, such as a forth-and-back path, lead to non-trivial correlations, which are non-Markovian and maybe even non-stationary. As a result, the standard tools for time-dependent random processes are not sufficient. To provide an intuitive understanding of the non-trivial correlations during shuttling, consider the case where a spin is moved from a point $x = 0$ at $t = 0$, to a point $x = L$ at $t = T$, at a constant velocity v, as in branch 1 of Fig. 3.1. The spin will experience a magnetic field, which can be modelled as a random process, $B(t) = B(x_c(t), t)$, making standard approximations about $B(t)$, such as being Gaussian, stationary, Markovian, etc. The position function is given by $x_c(t) = vt$. This allows analysis of the decoherence behaviour of the spin based on this random process. Similarly, the magnetic field along a path from $x = L$ to $x = 0$, as in branch 2 of Fig. 3.1, can also be modelled as a random process using the standard assumptions. However, when the two paths are concatenated,

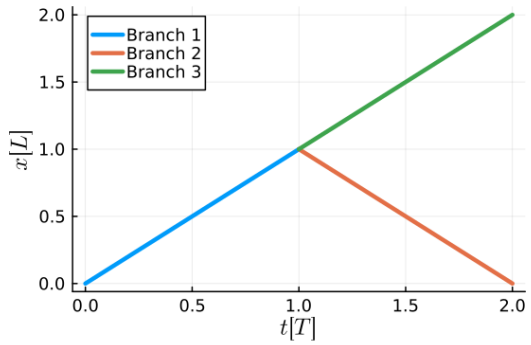

Figure 3.1: Paths representing the position of the spin over time for different shuttling paths. A forth-back path involves traversing branch 1 followed by branch 2, returning to the original point at the end of the shuttling time. A one-way path traverses branch 1 and branch 3.

i.e the path goes *forth* from $x = 0$ to $x = L$ from $t = 0$ to $t = T$, and then *back* from $x = L$ to $x = 0$ as time goes from $t = T$ to $t = 2T$, the magnetic field can no longer be described as a standard random process, due to the resurfacing correlations in space as the spin returns to its original point. The random magnetic field along this path is often non-stationary and non-Markvoian. This path will be referred to as a *forth-back* path, as opposed to the path created by concatenating branches 1 and 3 in Fig. 3.1, which will be called *one-way*. While a one-way path can be analysed using a standard random process, analysis of a forth-back path (or other non-trivial paths) requires a different mathematical framework to work with, which takes into account nontrivial correlations induced by the spin returning to its original location. This framework is provided by a random sheet, which will be discussed in the next chapter. For a specific path, we say that we have derived a random process from an underlying random sheet. The discussed concepts do not exclusively pertain to a forth-back path, but also to other nontrivial trajectories such as looped shuttling [44], or cases where multiple spins traverse the same path at different times [19].

3.4 Dynamical decoupling

One way to suppress dephasing/decoherence is the use of dynamical decoupling (DD) sequences, in which well-timed pulses can be used to suppress the effect of slowly varying noise. This technique has been shown to significantly extend the coherence time of *stationary* qubits. Two well-used sequences are the XY4 and XY8 sequences:

$$\mathrm{XY4} \equiv \tau - X - 2\tau - Y - 2\tau - X - 2\tau - Y - \tau, \tag{3.13}$$

$$\begin{aligned}\mathrm{XY8} \equiv\ & (\tau - X - 2\tau - Y - 2\tau - X - 2\tau - Y - \tau) \\ & - (\tau - Y - 2\tau - X - 2\tau - Y - 2\tau - X - \tau),\end{aligned} \tag{3.14}$$

where τ indicates the free evolution under a given Hamiltonian for a time τ, X/Y denotes a pulse which applies a π rotation around the x/y-axis, respectively.

These sequences work by effectively averaging out the low-frequency components of the noise, which are the dominant source of decoherence. The alternating X and Y pulses provide protection against noise along all three axes by periodically inverting the qubit state, or in the toggling frame, inverting the axes along which the noise is acting. This allows the refocusing of errors accumulated during the free evolutions. Furthermore, the XY8 sequence is symmetric, reducing the impact of pulse imperfections, making it particularly useful in experimental settings where gate fidelity is limited.

However, in the case of forth-back shuttling, correlations may be strongest during the evolutions that occur in the same spatial region, such as the start and the end, when the qubit returns to its original point. As a result, DD sequences that are highly effective for *stationary* qubits may become suboptimal for *shuttled* qubits. DD sequences work by allowing refocusing to occur between free evolutions during periods where noise is highly correlated. In the case of *stationary* qubits, this is most effective during the periods that are correlated in time, so refocusing should occur during periods before and after a pulse. However, for *shuttled* qubits, DD may be most effective by ensuring that refocusing occurs during periods correlated in space. We address this issue in Chapter 6, where we propose, analyse, and simulate new DD sequences, designed for shuttling.

Crucially, a path through stationary random sheet may lead to a non-stationary random process. This renders certain tools unusable for the analysis of DD sequences, such as filter function formalism based on the power spectral density [25].

In this chapter, we have introduced the problem we are studying, that of shuttled qubits under the influence of correlated random magnetic fields. We have emphasised the importance of a method for simulating magnetic fields whose direction varies significantly to allow the study of shuttling in Ge-like systems. Finally, we have discussed how DD sequences effective for *stationary* qubits may be suboptimal for *shuttled* qubits.

Chapter 4

Qubit decoherence due to random magnetic fields

In this chapter, we discuss how random effects can be modelled as static noise, random processes, or based on random sheets, and we present analytical solutions for the resulting decoherence. Understanding these scenarios provides insight into the mechanisms of decoherence and offers ways to verify the numerical solutions discussed in the following chapters.

4.1 Decoherence due to static noise

As a first look to see how random effects lead to decoherence, we consider the case where the magnetic field is a random variable acting along the z-axis. Assuming a Zeeman Hamiltonian according to Eq. (2.1) with magnetic field B and setting $\mu_B g_0 = 1$, the evolution operator describing the evolution of a state becomes

$$U_B(t) = \exp\left(-itBS_z\right) = \cos\left(\frac{Bt}{2}\right) - i\sin\left(\frac{Bt}{2}\right)\sigma_z, \tag{4.1}$$

indicating that the Hamiltonian induces a rotation of the state on the Bloch sphere around the z-axis, by an angle Bt. To introduce the effect of noise on a spin, consider the case where B is not a constant, but a value β randomly sampled from a Gaussian distribution:

$$f(x) = \frac{1}{\sqrt{2\pi\sigma^2}}\exp\left(-\frac{(x-\mu)^2}{2\sigma^2}\right) \sim \mathcal{N}(\mu, \sigma^2) \tag{4.2}$$

We let $\mu = 0$ as any nonzero mean could be absorbed into a deterministic field and therefore does not contribute to dephasing in this case. The variance is given by σ^2. The dephasing of the x component of the spin can be quantified by the value

$$\mathbb{E}[\langle S_x(t)\rangle] = \mathbb{E}\left[\mathrm{Tr}\left(\rho(0)U^\dagger{}_\beta(t)S_xU_\beta(t)\right)\right] \equiv \frac{1}{2}W_x(t), \tag{4.3}$$

which is the average projection of the spin onto the x-axis, where the averaging occurs over all possible realisations of β. Assuming an initial state $\rho(0) = |+\rangle\langle+| = \frac{1}{2}\begin{pmatrix}1 & 1\\ 1 & 1\end{pmatrix}$ fully along the x-axis, the state will process around the z-axis due to the

magnetic field. The angle by which it rotates will depend on the value of β for that realisation, leading to the average projection along the x-axis being

$$W_x(t) = \mathbb{E}[\cos(\beta t)] = \int_{-\infty}^{\infty} \cos(\beta t) f(\beta) d\beta = \exp\left(-\frac{t^2\sigma^2}{2}\right). \tag{4.4}$$

and $W_y = W_z = 0$. As time increases, the average projection along the x-axis tends to 0. Due to the magnetic field, the state rotates to some point on the equator. As t tends to infinity, the probability distribution of being in each position along the equator becomes uniform, leading to an average projection of zero. This means that all information on the phase of the qubit has been lost due to dephasing by a static field β. The timescale for this dephasing is $T_2^* = \frac{\sqrt{2}}{\sigma}$. The higher the variance of the noise, the faster the dephasing. This example showcases how random aspects of an environment can lead to undesirable behaviour for a qubit as information is lost. Furthermore, we have gained insight into the shape of the dephasing, which in this case is Gaussian.

Now, suppose that the noise is not only along the z-axis, but along all three axes, as will be the case for Ge. This means that the Hamiltonian that governs the evolution is given by

$$H = \tilde{\mathbf{B}} \cdot \mathbf{S}, \tag{4.5}$$

where $\tilde{\mathbf{B}} = (\tilde{B}_x, \tilde{B}_y, \tilde{B}_z)$ is a vector of random variables, with each random variable sampled from a zero-mean Gaussian distribution. The average projection of the x-component of the spin is given by (derivation in Appendix A.1)

$$W_x(t) = \frac{1}{3} + \frac{2}{3}(1 - \sigma^2 t^2) \exp\left(-\frac{\sigma^2 t^2}{2}\right). \tag{4.6}$$

For short times, the coherence decay is quicker than in the case where noise is only along the z-axis. Secondly, for long times the average projection tends to $1/3$. Finally, in this situation, the spin evolves to a point anywhere on the surface of the Bloch sphere, as opposed to just along the equator in the case where noise is only along z. This result is equivalent to the situation when considering the average decoherence due to the interaction of a spin with a large bath of spins [45]. This result will be used as verification of the method used to numerically calculate decoherence due to a 3D field in Chapter 5.

4.2 Dephasing due to an Ornstein-Uhlenbeck process

Now we turn to the description of the magnetic field as a random process. To achieve this, it is important to define the key concepts of random processes first. We draw from Chapter III of *Van Kampen*'s book on stochastic processes [46]. Given a random variable X, a stochastic process $Y(t)$ is given as

$$Y_X(t) = f(X, t). \tag{4.7}$$

Sampling the random variable X to give a value x leads to a *realisation* of the random process described as

$$Y_x(t) = f(x,t). \tag{4.8}$$

Subsequently, the average of the stochastic process is given by the weighted average of all realisations of Y as

$$\langle Y(t)\rangle = \int Y_x(t) P_X(x) dx. \tag{4.9}$$

Subsequently, the *autocovariance function* of a stochastic process is given by

$$K(t_1,t_2) = \langle Y(t_1)Y(t_2)\rangle - \langle Y(t_1)\rangle\langle Y(t_2)\rangle, \tag{4.10}$$

which when dealing with zero-mean processes reduces to the autocorrelation function

$$K(t_1,t_2) = \langle Y(t_1)Y(t_2)\rangle. \tag{4.11}$$

This quantity will be used to describe how correlated the two values of the magnetic field B at t_1 and t_2 are.

In this thesis, we consider only zero-mean stochastic processes, as any nonzero mean can be included in the deterministic component of the magnetic field. As a result, we use the terms covariance and correlation function interchangably. A stochastic process is called *stationary* when its moments are not affected by a shift in time (the lag τ), that is,

$$\langle Y(t_1+\tau)Y(t_2+\tau)\cdots Y(t_n+\tau)\rangle = \langle Y(t_1)Y(t_2)\cdots Y(t_n)\rangle, \tag{4.12}$$

An important consequence of stationarity is that statistical properties (such as the mean and variance) of $Y(t)$ do not change over time. This means that at any point in time, the probability distribution of the magnetic field at that point is identical.

Stationarity is a suitable assumption for the random effects on the spin as we consider these effects to be due to a very large bath of interacting spins, which will not change significantly as a result of the interaction, so the distribution describing the random effects will not change over time.

In the case of a stationary process, the autocovariance function can be described solely by the lag τ given by

$$K(\tau) = \langle Y(0)Y(\tau)\rangle. \tag{4.13}$$

In cases where the autocovariance function decays with increasing lag, the correlation time τ_c is then a constant such that $K(\tau)$ is zero or negligible for $\tau > \tau_c$. The correlation time of a magnetic field is important in describing how long-lived the correlations are. A magnetic field with a very long correlation time can be considered quasi-static, while a magnetic field with very short correlation times is akin to white noise.

When dealing with a stochastic quantity with several components $Y_i(t); i = 1,2,...,n$, the autocovariance function is replaced by a *covariance matrix* described by

$$K_{ij}(t_1,t_2) = \langle Y_i(t)Y_j(t)\rangle \tag{4.14}$$

or in the case of stationary processes,

$$K_{ij}(\tau) = \langle Y_i(0) Y_j(\tau) \rangle. \tag{4.15}$$

These quantities will become important when we consider the correlation between two different components of a random process, such as the x, y and z components of the magnetic field $\mathbf{B}$. We will consider these to be uncorrelated, such that $K_{ij}(\tau) = \delta_{ij} K_i(\tau)$ for $i, j = x, y, z$. This will only become relevant in the next chapters, as for the remainder of this chapter, we only deal with a random magnetic field along z.

The next step before defining the two other key properties, Gaussianity and Markovianity, is to describe probability densities for a stochastic process. The probability density for $Y_X(t)$ to take a certain value y at time t is given by

$$P(y, t) = \int \delta(y - Y_x(t)) P_X(x) dx. \tag{4.16}$$

The joint probability that Y has a value y_1 at t_1, and also y_2 at t_2, and so on up to n, is

$$P_n(y_1, t_1; y_2, t_2; ...; y_n, t_n) = \int \delta(y_1 - Y_x(t_1)) \cdots \delta(y_n - Y_x(t_n)) P_X(x) dx. \tag{4.17}$$

Then the conditional probability $P_{1|1}(y_2, t_2 | y_1, t_1)$ is the probability density for Y to take the value of y_2 at t_2, given that it has the value y_1 at t_1. A stochastic process is called a *Gaussian process* if all its P_n are Gaussian distributions, given by the probability distribution in Eq. (4.2). This means that any finite collection of random variables indexed at times in the random process has a multivariate normal distribution. Gaussianity is a suitable property to associate with the random effects which cause the spin to decohere due to the number of contributing interactions, which average out to a Gaussian variable by the central limit theorem. The most important aspect of a Gaussian process is that it is completely determined by its mean (in our case zero) and covariance function.

An important property that can be associated with a stochastic process is being a *Markov process*. Markovianity is the property that the probability that a state transitions to a subsequent state is dependent only on its current state (and explicitly not on its previous states). Mathematically, this means that for any $t_1 < t_2 < \cdots < t_n$

$$P_{1|n-1}(y_n, t_n | y_1, t_1; ...; y_{n-1}, t_{n-1}) = P_{1|1}(y_n, t_n | y_{n-1}, t_{n-1}). \tag{4.18}$$

The conditional probability density at t_n, given the value y_{n-1} at t_{n-1}, is determined only by the state y_{n-1} at t_{n-1}, with $P_{1|1}$ being the transition probability. This is a suitable assumption for the random effects acting on the spin because the bath is assumed to be very large and rapidly fluctuating, such that its influence on the system at any time depends only on the current state of the system. The correlations in the bath decay on timescales much shorter than the system dynamics, meaning the statistical properties of the driving noise due to the bath of spins can be well approximated by a Markov process.

We now have the tools we need to define the random process describing the magnetic field for a *stationary* qubit. The stochastic process that has all three

properties of being stationary, Gaussian, and Markovian is called the *Ornstein-Uhlenbeck* (OU) process [47]. An OU process is characterised by its covariance function as

$$K(\tau) = \sigma^2 e^{-\kappa\tau} \tag{4.19}$$

where σ^2 is the variance. For an OU process, the correlation between two points *exponentially decays* as the time between those two points increases. The speed at which this decay occurs is determined by $\kappa = 1/\tau_c$, where τ_c is the correlation time.

During this chapter and in Section 3.3, we motivated why an OU process is a suitable candidate for modelling the random magnetic field affecting a *stationary* qubit. Now we can discuss the dephasing behaviour of a spin under the influence of a magnetic field modelled as an OU process, where the magnetic field is allowed to change over time. The Hamiltonian becomes

$$H(t) = (B_0 + \tilde{B}(t))S_z, \tag{4.20}$$

where $\tilde{B}(t)$ is an OU process given by Eqs. (4.19)). B_0 is the deterministic part of the magnetic field, which results in a deterministic phase. For each realisation of $\tilde{B}(t)$, B_0 will contribute the same deterministic phase, and as such its effect can be neglected when looking at dephasing. This is only possible because the deterministic $B_0 S_z$ component and the random component $\tilde{B}(t)S_z$ commute. In the case where they do not, the deterministic magnetic field will affect the dephasing dynamics. To derive the average dephasing due to $\tilde{B}(t)$, we still use Eq. (4.3), but rather than β referring to a single randomly sampled value, it represents a single realisation of an OU process. The evolution operator for a single realisation is

$$U_\beta(t) = \exp\left(-i\int_0^t \tilde{B}_\beta(s)ds\right), \tag{4.21}$$

where the subscript β is indicative of a single realisation. For an OU process, it can be shown that

$$W_x(t) = \exp\left(-\frac{\sigma^2}{\kappa^2}[\kappa t - 1 + e^{-\kappa t}]\right). \tag{4.22}$$

The decay can be separated into two regimes: Short times where $t \ll \tau_c = 1/\kappa$, and long times where $t \gg \tau_c$, with the following decay curves:

$$\text{Short times: } t \ll \tau_c,\ W_x(t) = \exp\left(\frac{-\sigma^2 t^2}{2}\right) \tag{4.23}$$

$$\text{Long times: } t \gg \tau_c,\ W_x(t) = \exp\left(\frac{-\sigma^2 t}{\kappa}\right) \tag{4.24}$$

Notice that for short times, we have the same Gaussian decay as in the static case analysed previously. This can be interpreted as the process not having had time to change yet, so it can be treated as a (quasi-)static field. For long times, the decay is exponential. This allows us to identify two regimes. In the case where the variance is high and the correlation time long (strong slow noise), decoherence occurs completely according Gaussian decay curve, during the period where $t \ll t_c$, with decoherence time $T_2^* = \frac{\sqrt{2}}{\sigma}$. In the case where the variance is small and the

correlation time small (weak fast noise), decoherence occurs mostly according to the exponential decay curve for $t \gg t_c$, with a decoherence time $T_2^* = \frac{\kappa}{\sigma^2}$. This is the motional narrowing regime, and in the limit of very fast and very weak noise, the coherence time tends to infinity.

By considering this scenario, we have gained insight into how we can calculate dephasing for time-dependent magnetic fields modelled as random processes, and identified two important regimes for dephasing: the quasi-static regime where noise is strong and slow, and the motional narrowing regime where noise is weak and fast.

4.3 Dephasing during shuttling in an Ornstein-Uhlenbeck sheet

Now we turn to considering the magnetic field for a shuttled qubit. This field will vary and be correlated not only in time but also in space. This requires the description of a random sheet, the complete mathematical description of which can be found in Mokeev et al. [19]. Here, we focus on the properties we need to describe the random magnetic field during shuttling. Many properties and definitions naturally extend from random processes to random sheets. Importantly, the covariance function for an OU-sheet can be defined as

$$K_{OU}(\theta, \theta') = \frac{\sigma^2}{4\kappa_x \kappa_t} \exp(-\kappa_x |x - x'| - \kappa_t |t - t'|) \tag{4.25}$$

$$\equiv \sigma_B^2 \exp(-\kappa_x |x - x'| - \kappa_t |t - t'|), \tag{4.26}$$

where $\theta = (x, t)$ and $\theta' = (x', t')$ are two points on the sheet. The parameters $\lambda_c = 1/\kappa_x$ and $\tau_c = 1/\kappa_c$ denote the correlation length and correlation time respectively, and $\sigma_B = \sigma/\sqrt{4\kappa_x \kappa_t}$. In the case of a one-way path taken with constant velocity v, this covariance function reduces to that of a random process:

$$K(t, t') = \sigma_B^2 \exp(-\kappa |t - t'|), \tag{4.27}$$

where $\kappa = \kappa_t + v\kappa_x$ characterises the correlation time of a standard OU process. For nontrivial paths such as forth-back shuttling, this reduction is not possible. Importantly, while the underlying random sheet may be stationary, the random process along a path through a random sheet is often non-stationary. However, the random process does inherit the Gaussianity from the underlying random sheet, allowing Eq. (4.26) to be used to describe the random process.

An example realisation of a magnetic field based on an OU sheet is shown in Fig. 4.1(a), with Fig. 4.1(b) showing the magnetic field derived from a forth-back path through the sheet, along with the mirror image of only the forth-path where we observe correlation between the two. The resurfacing correlations in space are exemplified in Fig. 4.1(c). This shows the importance of using a random process derived from a random sheet to describe the magnetic field during shuttling, rather than a standard random process.

We will now observe the dephasing behaviour when we describe the random magnetic field in Eq. (4.20) as a random sheet. This will give insight into the shuttling regimes where the random sheet model is most important, and the analytical

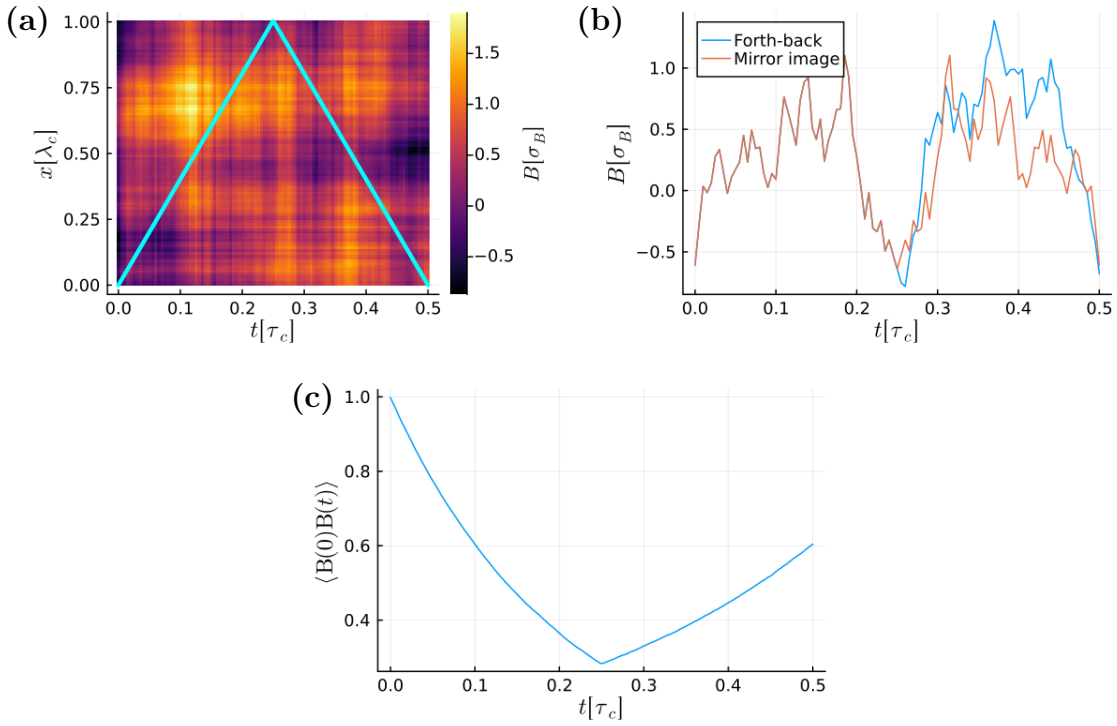

Figure 4.1: **(a)**: A single realisation of an OU sheet. The cyan line represents the forth-back path. **(b)**: The random process along the path derived from the forth-path, as well as the reflection of the path along branch 1. There is a noticeable correlation between the original path and the reflected path. **(c)**: The average correlation over many realisations showing a clear resurfacing of correlation as branch 2 is traversed.

solutions will be used as a comparison for the numerical simulations in the next chapters.

The dephasing characteristic can be found by integrating over the covariance function. Consider first a *one-way* path from $x = 0$ to $x = 2L$ traversed during a time $2T$ at constant velocity. At the end of the shuttling path $W_x(t_0 = 2T) = \exp(-\chi(t_0))$ is given by

$$\chi_{\text{ow}}(t_0) = (\sigma_B/\kappa_t)^2 \Lambda_0(\beta, \gamma) \tag{4.28}$$

$$\Lambda_0 = \frac{2(\beta + \gamma) + e^{-2(\beta+\gamma)} - 1}{(1 + \gamma/\beta)^2} \tag{4.29}$$

where the dimensionless quantities $\beta = \kappa_t T$ and $\gamma = \kappa_x L$ are introduced. On the other hand, in the case of *forth-back* shuttling, the dephasing is given by

$$\chi_{\text{fb}}(t_0) = (\sigma_B/\kappa_t)^2 \Lambda, \quad \Lambda = \Lambda_1 + \Lambda_2 \tag{4.30}$$

$$\Lambda_1 = \frac{2(\beta + \gamma + e^{-\beta-\gamma} - 1)}{(1 + \gamma/\beta)^2} \tag{4.31}$$

$$\Lambda_2 = \frac{(e^{-2\beta} - 1)(\gamma/\beta) - 2e^{-\beta-\gamma} + e^{-2\beta} + 1}{1 - \gamma^2/\beta^2} \tag{4.32}$$

Fig. 4.2 shows a two-dimensional plot of how the dephasing during one-way shuttling compares to dephasing during forth-back shuttling for different correlation times and lengths. Figs. 4.2(a), 4.2(b) show that for $\tau_c \to 0$ and $\lambda_c \to 0$, the dephasing is minimised as the system tends to the motional narrowing regime, while for large τ_c and large λ_c dephasing is maximised as the random sheet is quasi-static. In the regime where λ_c is small and τ_c is large, the absolute difference in dephasing between one-way shuttling and forth-back shuttling is larger, as shown in Fig. 4.2(c). This is expected as due to the small λ_c, the correlations in space are quickly lost while in time the random process along the shuttling path is almost constant as τ_c is large. However, as the spin returns to the original point in the forth-back path, the correlations in space resurface, contributing to additional dephasing. Fig. 4.2(d) shows how the difference is dependent on σ_B and λ_c. As σ_B increases, the value of λ_c for which the difference is largest decreases quadratically. The parameters for which the difference between one-way and forth-back shuttling is highest determine when the random sheet approach is most important when considering a nontrivial shuttling path.

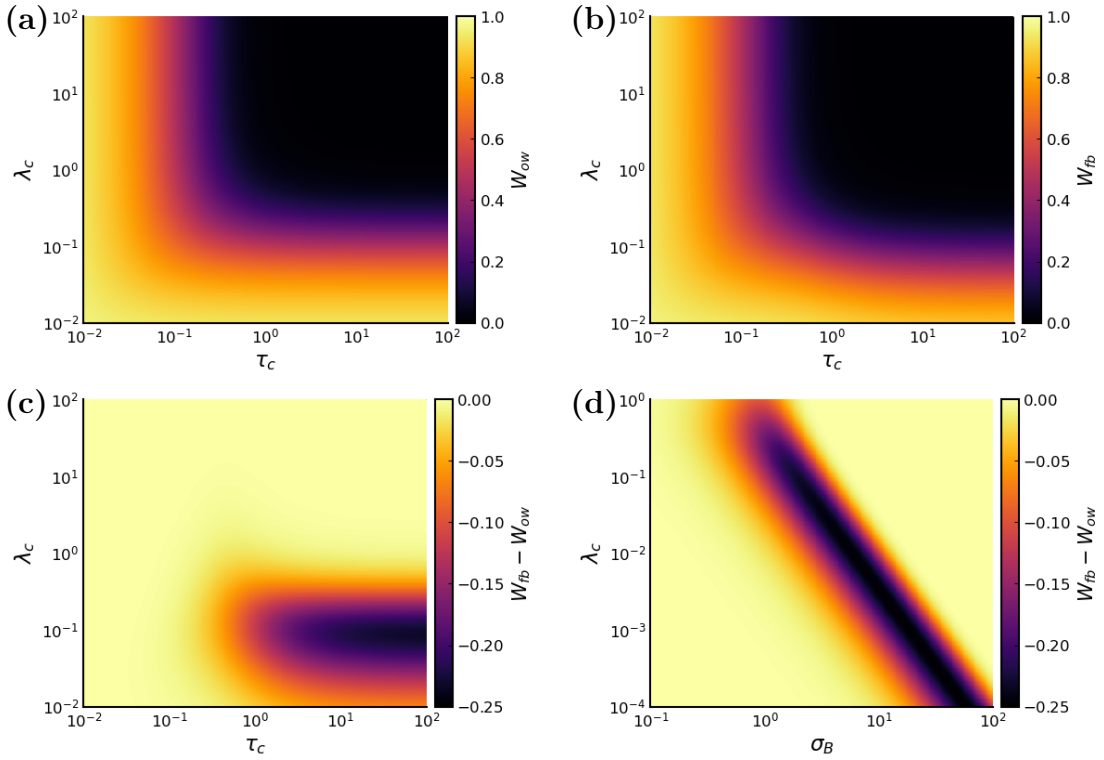

Figure 4.2: Calculations of the dephasing $W_x = \exp(-\chi(t_0 = 2T))$ (the subscript x has been excluded in the axis labels), using **(a)**: Eqs. (4.28)-(4.29) for one-way shuttling, **(b)**: Eqs.(4.30)-(4.32) for forth-back shuttling, for different correlation times τ_c and correlation lengths λ_c. For **(a), (b), (c)**: $T = L = 1$, $\sigma_B = 2$. The singularity at $\tau_c = \lambda_c$ ($\gamma = \beta$ in Eq. (4.32)) is removable [19]. **(c)**: The difference $W_{fb} - W_{ow}$, showing a highest difference for small $\lambda_c \approx 0.1$ and large τ_c. **(d)**: Dependence of the difference $W_{fb} - W_{ow}$ on λ_c and σ_B, for $\tau_c = 100$. The value of λ_c for which the absolute difference is highest decreases as σ_B increases.

These results give an indication of the behaviour that is expected when we simulate the Hamiltonian in Eq. (3.4) in the next chapter, as well as the regimes where

we expect the forth-back shuttling to most differ from one-way shuttling.

In this chapter, we have discussed important concepts for understanding dephasing and decoherence by considering spins under the influence of random processes in different scenarios. There are three problems which we will address in the next chapters. First, in Chapter 5, we will address how to numerically calculate the decoherence due to a random magnetic field along all three axes. Secondly, in Chapter 6, we will analyse existing dynamical decoupling sequences and introduce new sequences designed for shuttling. We will assess their efficacy at suppressing decoherence in a Si-like system where the direction of the magnetic field is strongly along z, but there is a random component along all three axes, where we make use of the method developed in Chapter 5. Finally, in Chapter 7 we will apply this method to a Ge-like system where the direction of the magnetic field varies significantly, and assess the efficacy of the same DD sequences.

Chapter 5

Simulating spin dynamics in a 3D random magnetic field

In this chapter, we introduce and benchmark a method to numerically calculate the average effect of a Hamiltonian of the form

$$H(x,t) = \left(\mathbf{B}_0(x) + \tilde{\mathbf{B}}_{\text{eff}}(x,t)\right) \cdot \mathbf{S}, \tag{5.1}$$

where we have a deterministic field $\mathbf{B}_0$ which may vary along the shuttling path, and a random field $\tilde{\mathbf{B}}_{\text{eff}}(x,t)$. This model is applicable to Ge channels, where the direction of the magnetic field will vary significantly. This variation will consist of a time-independent part ($\mathbf{B}_0$), which is specific to the device being modelled and varies along the channel, as well as a time-dependent part $\tilde{\mathbf{B}}_{\text{eff}}$, which will change over the course of a single shuttle. We model the random magnetic field $\tilde{\mathbf{B}}_{\text{eff}}(x,t) = \left(\tilde{B}_x(x,t), \tilde{B}_y(x,t), \tilde{B}_z(x,t)\right)$ as a 3-component random process where each random process is derived from an independent random sheet:

$$\langle \tilde{B}_a(\theta_1)\tilde{B}_b(\theta_2)\rangle = \delta_{ab}K_a(\theta_1,\theta_2); \quad a,b = x,y,z, \tag{5.2}$$

where $\theta = (x,t)$, and in this thesis we focus on the covariance function $K_i(\theta_1,\theta_2)$ of an OU sheet as in Eq. (4.26). Each component will have equal correlation times τ_c and lengths λ_c, but may differing variances σ_a^2, such that

$$K_a(\theta_1,\theta_2) = \sigma_a^2 \exp(-\kappa_x|x_1 - x_2| - \kappa_t|t_1 - t_2|). \tag{5.3}$$

where, to clarify, the variable x in κ_x refers to spatial position (not an axis label), similar to t in κ_t referring to time.

We will introduce several tools which are required to calculate the average effect and prove the rigorous bounds for the error. We subsequently use the developed method and compare the result to analytical solutions in specific scenarios to confirm that the error is bounded and scales well. Next, we use the developed model to analyse specific shuttling scenarios and compare one-way shuttling to forth-back shuttling. This method was developed earlier [48], but its usefulness, accuracy, and performance, have never been studied in practice.

5.1 Numerical methods

Let us first introduce the definite goal and the problems faced en route. First, we need to be able to generate realisations of the random magnetic field along a shuttling path. We need to be able to do this efficiently, given specific properties of the random sheet underlying the magnetic field. For this, we use the *Cholesky Decomposition*. Once we have values of the magnetic field along the path, we need to be able to calculate the total evolution operator, which involves calculating the piecewise evolution at each point. To perform this step, we utilise the *Suzuki-Trotter decomposition*. Finally, once we have realisations of the evolution operator along the shuttling path, we combine them using *Monte Carlo sampling* to calculate the average effect, in this decoherence.

5.1.1 Suzuki-Trotter Decomposition

Given a realisation of a random magnetic field, we need to be able to calculate the average effect of the Hamiltonian for a single realisation by calculating the total evolution operator. To this purpose, we are first interested in the evolution at each step along a discretised path (x_j, t_j) where the total magnetic field is $\mathbf{B}_j$ as

$$U_j = \exp\left[-i\Delta t(B_{j,x}S_x + B_{j,y}S_y + B_{j,z}S_z)\right], \tag{5.4}$$

where $\Delta t = T/N$ with T being the total duration of the evolution, and N being the degree to which we discretise the path and the random sheet. Using the first-order Suzuki-Trotter approximation, this evolution can be approximated as

$$U_j \approx \exp(-iB_{j,x}\Delta t S_x)\exp(-iB_{j,y}\Delta t S_y)\exp(-iB_{j,z}\Delta t S_z) + \mathcal{O}(\Delta t^2), \tag{5.5}$$

This allows the treatment of the evolution as a piecewise rotation around each axis, where the rotation angle is described by the quantity $B_{j,i}\Delta t$. This is important for proving rigorous bounds when the effect of total evolution is calculated. The total evolution operator is then given by the product of these piecewise evolutions.

5.1.2 Monte Carlo sampling

Suppose that we have generated M realisations, and for each realisation we can calculate a quantity w_i (for example, average projection along x) based on the total evolution operator for that realisation. By performing these steps for a large number of realisations, the average value will converge to the true expected value by the law of large numbers:

$$W_{MC} = \frac{1}{M}\sum_{i=1}^{M} w_i \to W \tag{5.6}$$

The accuracy of this estimate depends on the number of samples M and the variance of w_i. Since $w_i \in [-1, 1]$, the variance is bounded above by 1.The Monte Carlo error is $\mathcal{O}(1/\sqrt{M})$.

We have a way to calculate the total evolution operator for a single realisation, and have discussed how we use the Monte Carlo method to calculate the average

value of a quantity by considering many realisation. We still need a method to efficiently generate realisation of the magnetic field along the shuttling path, given the covariance matrix along that path. To do this, we use the Cholesky decomposition.

We can discretise the shuttling path into a set of points $\{\theta_1, \theta_2, ...\theta_n\}$. For these points, the covariance matrix $\mathbf{C}_a$ for each $a = x, y, z$ can be calculated according to Eq. (5.3). As the random process along each axis is independent, the covariance matrices can be considered independently. The elements of the covariance matrix $\mathbf{C}_a$ are

$$C_{a,i,j} = K_a(\theta_i, \theta_j). \tag{5.7}$$

The Cholesky decomposition is important to allow the efficient sampling of a random process with a given covariance. This avoids having to generate an entire random sheet; instead, it only requires the covariance function along the shuttling path. The Cholesky decomposition involves the decomposition of any Hermitian positive definite matrix $\mathbf{M}$ into the form $\mathbf{M} = \mathbf{L}\mathbf{L}^*$, where $\mathbf{L}$ is a lower triangular matrix with real and positive diagonal entries. For positive semi-definite matrices, the diagonal entries of $\mathbf{L}$ may be zero and the decomposition is not unique. Any covariance matrix is positive semi-definite. For the covariance matrix given by Eq. (5.7), $\mathbf{L}$ will be real, which means $\mathbf{L}^* = \mathbf{L}^T$. If $\mathbf{z} = (z_1, z_2, ..., z_n)$ is a vector of n uncorrelated random variables generated from a standard normal distribution $(z_1, z_2, ..., z_n)$, then the vector $\mathbf{x} = \mathbf{L}\mathbf{z}$ is a zero-mean random process with the desired covariance matrix (4.26). This follows from $\langle \mathbf{x}\mathbf{x}^T \rangle = \langle \mathbf{L}\mathbf{z}\mathbf{z}^T\mathbf{L}^T \rangle = \langle \mathbf{L}\mathbf{L}^T \rangle = \mathbf{C}$. Hence, this method can be used to generate realisations of the random process to be used during Monte Carlo sampling.

5.1.3 Calculating the average effect of a 3D random magnetic field

With the tools discussed above, we can construct the total method. For a single realisation of m of the Hamiltonian H in Eq. (5.1), the total evolution operator along the shuttling path can be separated into pieces as

$$U_m = \mathcal{T} \exp\left(-i \int_{t_{N-1}}^{t_N} H_m(s) ds\right) ... \mathcal{T} \exp\left(-i \int_{t_0}^{t_1} H_m(s) ds\right), \tag{5.8}$$

where N is the discretisation number. $\mathcal{T}$ is the time-ordering operator required to preserve time ordering as the operators do not commute in general. For a single piece at point n, the Suzuki-Trotter approximation leads to

$$\mathcal{T} \exp\left(-i \int_{t_n}^{t_{n+1}} \sum_{j=x,y,z} B_{m,j}(s) S_j \, ds\right) \approx \prod_{j=x,y,z} \mathcal{T} \exp\left(-i \int_{t_n}^{t_{n+1}} B_{m,j}(s) S_j \, ds\right). \tag{5.9}$$

In each separate factor x, y, z, the Hamiltonian commutes with itself during the evolution i.e $\forall t, t'$, $[B_{m,j}(t)S_j, B_{m,j}(t')S_j] = 0$, which means that the time ordering can be omitted. Subsequently, we estimate each integral as

$$\int_{t_n}^{t_{n+1}} B_{m,j}(s) ds \approx (t_{n+1} - t_n) B_{m,j}(t_n) \equiv \phi_{m,n}^{(j)}. \tag{5.10}$$

Eventually, for a realisation m, the total evolution operator is

$$U_m = \left[\prod_{n=1}^{N} \exp\left(-i\phi_{m,n}^{(x)}\sigma_x\right) \exp\left(-i\phi_{m,n}^{(y)}\sigma_y\right) \exp\left(-i\phi_{m,n}^{(z)}\sigma_z\right)\right] + \mathcal{O}(N^{-1}), \tag{5.11}$$

which we can use to calculate a quantity such as the average projection of the x-component of the spin as

$$\frac{1}{2}W_x = \mathbb{E}\left[\langle S_x(t)\rangle\right] = \mathbb{E}\left[\mathrm{Tr}(S_x U^\dagger S_x U)\right] \approx \frac{1}{M}\sum_{m=1}^{M} \mathrm{Tr}(S_x U_m^\dagger S_x U_m), \tag{5.12}$$

where the Monte Carlo error is $\mathcal{O}(M^{-\frac{1}{2}})$, and the discretisation error is $\mathcal{O}(N^{-\frac{1}{2}})$.

An important note is that the main source of error in N is due to the discretisation of the random process, and not due to the use of the Suzuki-Trotter approximation. As a result, higher order Suzuki-Trotter methods will not lead to better error scaling. A formal derivation for this method is provided by Mokeev et al. [48].

We can use the same method to calculate W_y, W_z, and therefore the decoherence factor as

$$W = \sqrt{W_x^2 + W_y^2 + W_z^2} \tag{5.13}$$

or alternatively the average fidelity as

$$F = \frac{1}{3} + \frac{1}{6}\mathbb{E}\left[|\mathrm{Tr}(U_m)|^2\right]. \tag{5.14}$$

The average fidelity quantifies how close the quantum operation caused by the shuttling is to the ideal operation, which in our case is the identity operation. Physically, a high average fidelity means that before and after the shuttling operation, the qubit is in the same state.

5.2 Accuracy of numerical simulations

For the proposed model and methods, we need to demonstrate that the obtained results are accurate and that the error scales as expected when the discretisation number N or the Monte Carlo number M is increased. There is no general analytical solution for the 3D model that we can use to assess accuracy, so instead, we assess numerical accuracy via two methods. Firstly, we use a slightly simplified version of the 3D model, which still requires the described method to simulate, but allows us to use the analytical solution given by Eqs. (4.30)-(4.32) for the 1D model. To make use of the analytical solution, we set up the Hamiltonian in Eq. (5.1) such that $B_x = B_y = B_z$ and $B_0 = 0$. This means that the direction of the magnetic field is constant, while its magnitude is derived from an OU sheet. This is a rotated form of the Hamiltonian in Eq. (4.20). By performing a similar rotation in the axis along which we measure the dephasing, we arrive at a situation where the

analytical solution given in Eqs. (4.30)-(4.32) applies in the case of forth-back shuttling. Explicitly, we use the following model and measure

$$H = \tilde{B}(S_x + S_y + S_z) \tag{5.15}$$

$$W_x = 2\mathbb{E}\left[\langle S'_x \rangle\right] = 2\mathbb{E}\left[\mathrm{Tr}(S'_x U_\beta^\dagger S'_x U_\beta)\right] \tag{5.16}$$

$$S'_x = \frac{1}{\sqrt{2}}(S_x - S_y) \tag{5.17}$$

with $\tilde{B}$ a random process derived from forth-back path on an OU sheet with variance σ_B. Using this method leads to the error scaling in N shown in Fig. 5.1(a), and error scaling in M shown in Fig. 5.1(c). Alternatively we can assess the error scaling of the model given by Eq. (5.1) and the subsequent methods by generating a "high resolution" target value using large values of N and M, which we can use to test the error scaling for smaller values of N and M as N or M increases. The target value is generated at values of $N = 1000$, $M = 10^6$. The resulting error scaling in increasing N is shown in Fig. 5.1(b), and the error scaling in increasing M is shown in Fig. 5.1(d). For both methods, the error scaling in N is better than the expected $\epsilon = A/\sqrt{N}$. Both methods show the expected $\mathcal{O}(1/\sqrt{M})$ scaling in error due to Monte Carlo sampling.

Finally, Fig. 5.2 shows the error for different N (in the case of analytical comparison akin to Fig 5.1(a), for parameters closer to the values which will be used in the next chapter, most importantly a short shuttling time T resulting in significantly lower Δt. This gives a more useful indicator of the accuracy of the results when we analyse various scenarios and compare different decoupling sequences. Importantly, at $N = 300$ we have an error on the order of 10^{-5}.

5.3 Shuttling simulations in limiting cases

Having presented and verified the accuracy of the method we use to calculate the effect of a 3-component random magnetic field on a shuttled spin, we can turn to using it to simulate various scenarios.

5.3.1 Static field

The first scenario we consider is the limit where $\tau_c \to \infty$, $\lambda_c \to \infty$, and when there is no deterministic magnetic field ($\mathbf{B}_0 = 0$), resulting in a quasi-static magnetic field resembling the Hamiltonian in Eq. (4.5). The results for this case are shown in Fig. 5.3, showing agreement with the analytical solution. In the case where $B_0 \neq 0$, the characteristic curve is similar but does not tend to 1/3 in the limit $t \to \infty$. Using smaller values of τ_c and λ_c leads to further decoherence away from a value of $\frac{1}{3}$, due to the effect of variation of the field along the shuttling path. These results confirm that the model and methods used lead to expected decoherence characteristics when in the quasi-static regime.

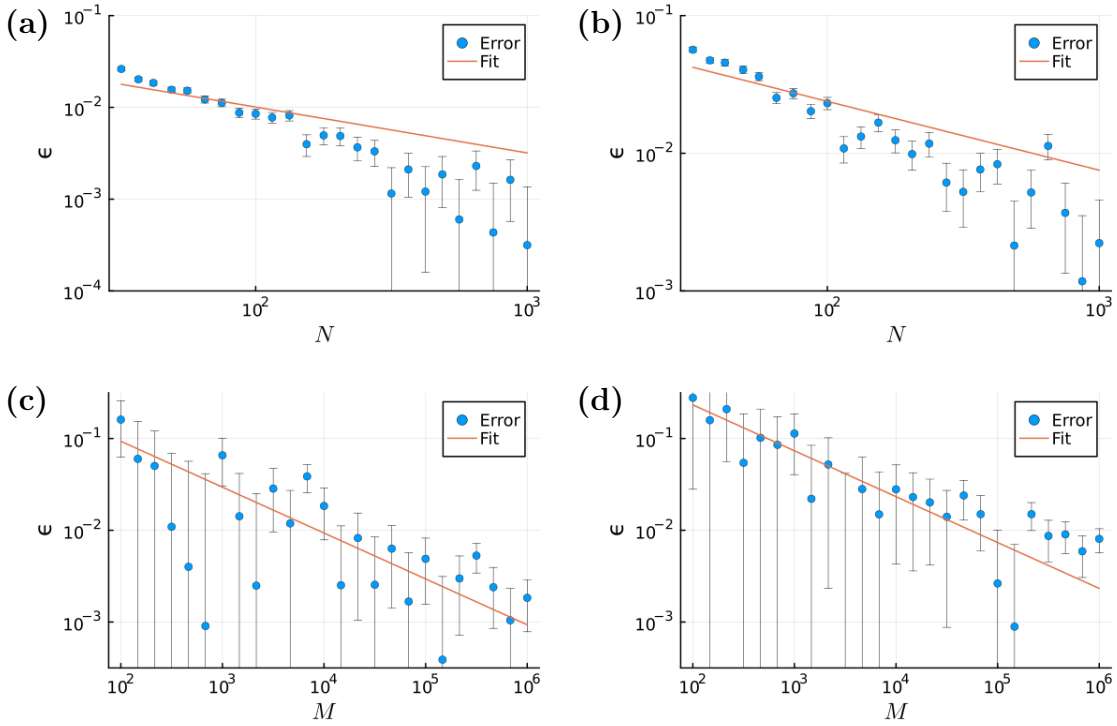

Figure 5.1: Numerical accuracy of the calculation of the decoherence for the forth-back spin shuttling. Calculations were performed for $\tau_c = \lambda_c = 1$, $T = 1$, $L = 2$. **(a),(c)**: $\sigma_B = 1/\sqrt{3}$. **(b), (d)** $\sigma_x = \sigma_y = \sigma_z = 1$. **(a)** and **(c)**: Simplified model given by Eqs. (5.15)-(5.17), where the error is calculated relative to the analytical solution using Eq. (4.30). **(b)** and **(d)**: Error relative to a target value calculated at $N = 10^3$, $M = 10^6$. **(a)**,**(b)**: Numerical error calculated as a function of the discretisation number N. The number of samples is $M = 10^6$. The results are fitted to the curve $\epsilon = A/\sqrt{N}$. **(c)**, **(d)**: Numerical error calculated as a function of the number of Monte Carlo samples M. The discretisation number is $N = 300$. The results are fitted to the curve $\epsilon = A\sqrt{M}$, showing agreement with the expected scaling in the error due to Monte Carlo sampling. The fitting parameters are **(a)**: $A = 0.10$, **(b)**: $A = 0.24$, **(c)**: $A = 0.93$, **(d)**: $A = 2.32$,

5.3.2 One-way vs. forth-back shuttling

We will now focus on comparing one-way to forth-back shuttling in the limiting cases where the correlation time is long or short, and similarly for the correlation length. These results will indicate how the spin precesses due to a random magnetic field, and the differences between one-way and forth-back shuttling. The Hamiltonian we simulate is given by Eq. (5.1), with $\mathbf{B}_0 = B_0\hat{z}$. The variance of the random magnetic field will be on the order of the deterministic magnetic field, such that the direction of the magnetic field will vary significantly during shuttling. We look at how the projection along x changes during shuttling. The four limiting regimes we simulate are where τ_c, λ_c are both short, both long, or one is short and one is long, relative to the shuttling length and time. In the case that both τ_c and λ_c are short, we are in the motional narrowing regime. If both are long, then we are in the quasi-static regime.

Results are shown in Figs. 5.4, 5.5, and 5.6. In each plot, we compare the

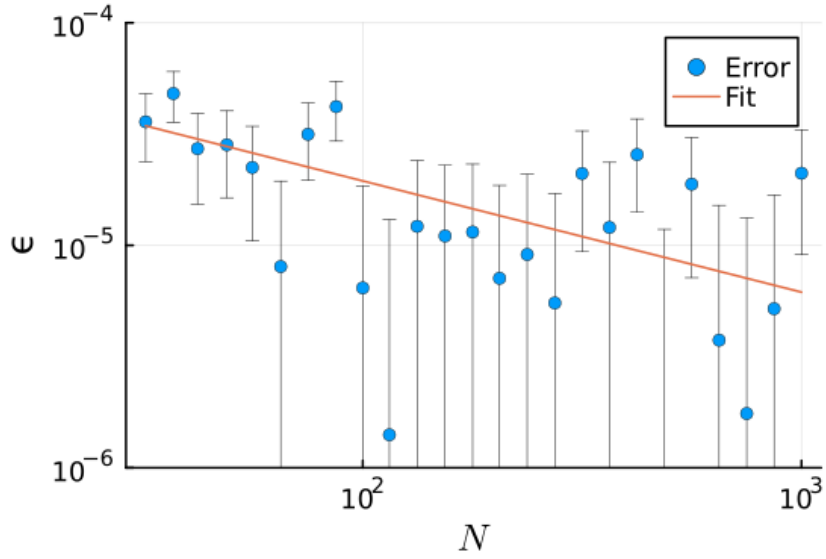

Figure 5.2: Same simulation as in Fig. 5.1(a) for more realistic simulation parameters: $\tau_c = \lambda_c = 1$, $T = 1/30$, $L = 4$, $\sigma_B = 1$, $B_0 = 100$, $M = 10^4$. This figure indicates the expected error for the simulations performed in the next chapters. The results are fitted to the curve $\epsilon = A/\sqrt{N}$. The fitting parameter is $A = 2 \times 10^{-4}$.

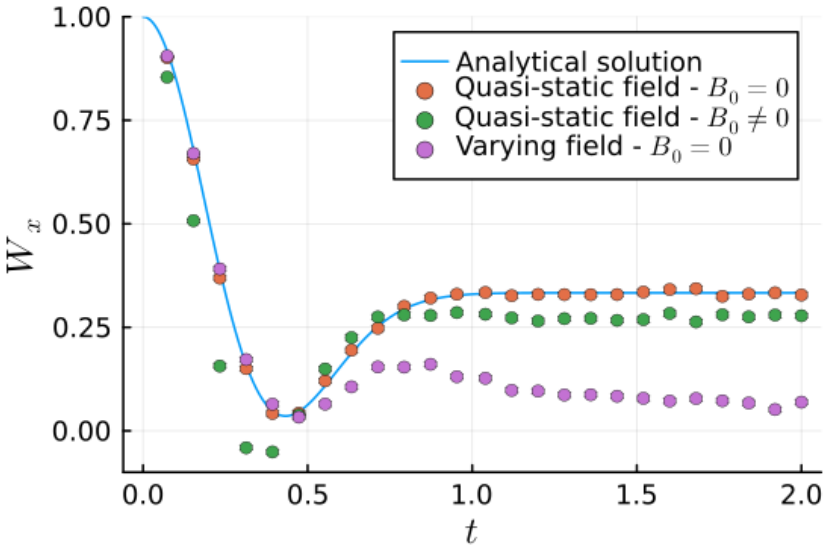

Figure 5.3: Comparison of numerical results for decoherence of the x-component of the spin due to a random field to the analytical solution given by Eq. (4.6). Simulation parameters are $\sigma_x = \sigma_y = \sigma_z = 4$, $N = 300$, $M = 10^4$. (blue): $B_0 = 0$, $\tau_c = 10000$, $\lambda_c = 10000$. (orange): $B_0 = 4$, $\tau_c = 10000$, $\lambda_c = 10000$. (green): $B_0 = 0$, $\tau_c = 3$, $\lambda_c = 3$. Error bars are included but small enough to not be visible.

evolution of the projection along the x-axis between a one-way path and a forth-back path for the same parameters. The difference between the three sets of figures lies in their values for σ_z and B_0. Fig. 5.4 shows the results in the case where $\sigma_x = \sigma_y = \sigma_z = B_0$. In Fig. 5.4(a), the case where $\tau_c \ll T$, $\lambda_c \ll L$, the motional

narrowing regime. We observe a Larmor precession due to the quantising magnetic field B_0, which is constant along the shuttling path. The effect of decoherence can be observed in that the peak does not resurface to a value of 1. Similar behaviour is observed in Fig. 5.4(b), where $\tau_c \ll T,\ \lambda_c \gg L$. The slightly increased decoherence is a result of the correlation in space not significantly decaying, so compared to Fig. 5.4(b) the noise is effectively "less fast". In Fig. 5.4(c) where $\tau_c \gg T,\ \lambda_c \ll L$, a difference between the decoherence for one-way and forth-back shuttling is observed. For this regime, the noise in time is almost static, while in space, the correlations are quickly lost. For the one-way path, the result is similar to the result in Fig. 5.4(b), but for the forth-back path, the correlations in space are regained as the spin returns to its original point, leading to an increased decoherence. This numerical result reflects the discussion on the analytical case surrounding Fig. 4.2 and emphasises the importance of the random sheet treatment for decoherence along non-trivial paths, for these parameters we are in the regime where the difference between forth-back and one-way shuttling is largest. Finally in Fig. 5.4(d) where $\tau_c \gg T,\ \lambda_c \gg L$, the system can be considered quasi-static as correlations in both space and time are preserved along the whole shuttling path, which results in decoherence very similar to the analytical solution for a random static field.

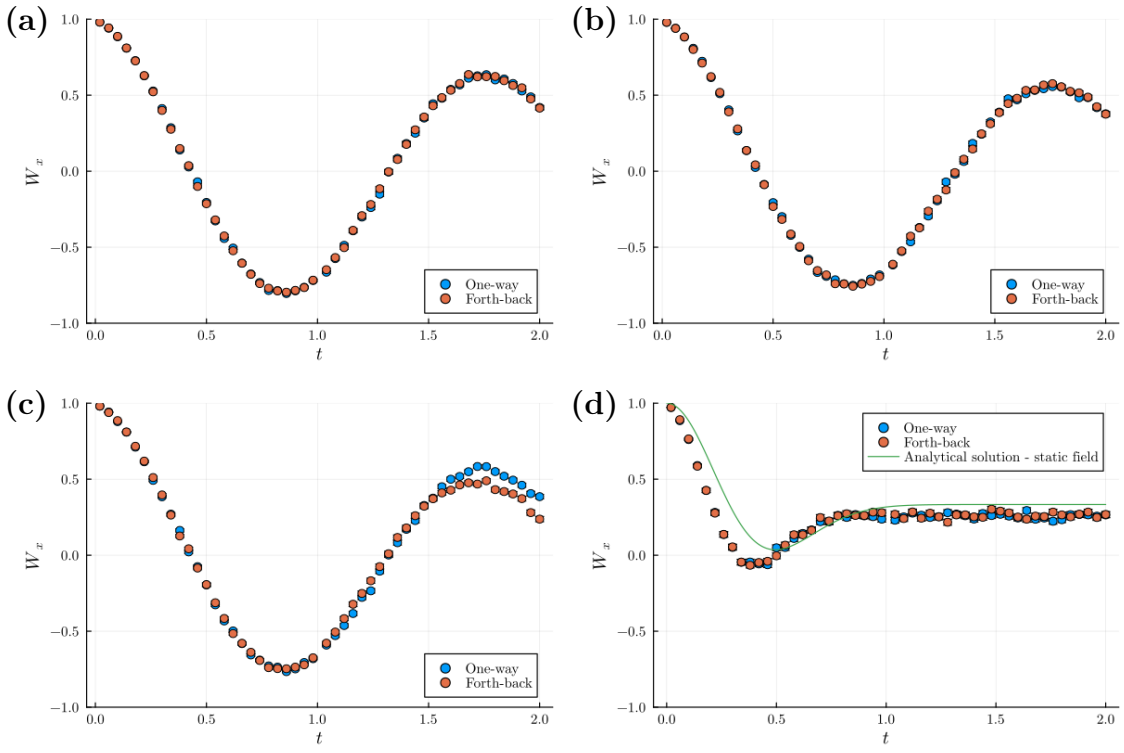

Figure 5.4: Plots showing how the average projection along the x-axis $W_x = 2\mathbb{E}[\langle S_x(t)\rangle]$ changes along the shuttling path for $\sigma_x = \sigma_y = \sigma_z = B_0 = 3.5$ and $T = L = 1$. **(a)**: $\tau_c = \lambda_c = 1/100$. **(b)**: $\tau_c = 1/100$, $\lambda_c = 100$. **(c)**: $\tau_c = 100$, $\lambda_c = 1/100$, **(d)**: $\tau_c = \lambda_c = 100$. Error bars are included but too small to be visible.

We are now interested in the effect of changing σ_z and B_0 on the decoherence behaviour, which influences how much the direction of the magnetic field can vary. Fig. 5.5 shows the results in the case where $\sigma_x = \sigma_y = \frac{1}{2}\sigma_z = \frac{1}{2}B_0$. These parameters result in a quantisation axis that is slightly more strongly localised along the z-axis.

In all figures, the oscillation period is smaller due to the larger B_0. Furthermore, the increased value of σ_z leads to increased decoherence in the form of a lower resurfacing peak. In Fig. 5.5(c), the difference between one-way and forth-back shuttling is again observed as the spin returns to its original point.

Fig. 5.6 shows the results when $\sigma_x = \sigma_y = 2\sigma_z = B_0$, resulting in a smaller variance along the z-axis. In general, this results in reduced decoherence and higher resurfacing peaks. In Fig. 5.4(c), the difference between one-way and forth-back shuttling has become negligible. This signifies that for these values of τ_c, λ_c and $\sigma_{x,y,z}$, we have departed from the regime where the difference between one-way and forth-back shuttling is largest, see Fig. 4.2(d).

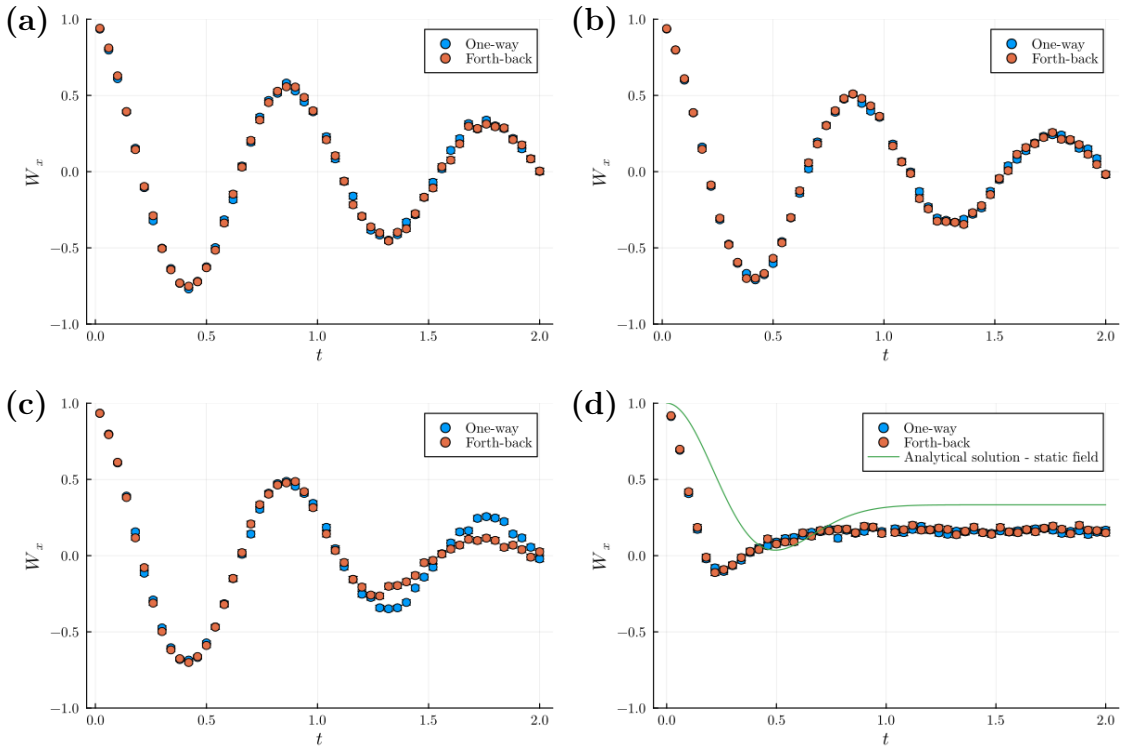

Figure 5.5: Plots showing how the average projection along the x-axis $W_x = 2\mathbb{E}[\langle S_x(t)\rangle]$ changes along the shuttling path for $\sigma_x = \sigma_y = \frac{1}{2}\sigma_z = \frac{1}{2}B_0 = 3.5$ and $T = L = 1$. **(a)**: $\tau_c = \lambda_c = 1/100$. **(b)**: $\tau_c = 1/100$, $\lambda_c = 100$. **(c)**: $\tau_c = 100$, $\lambda_c = 1/100$, **(d)**: $\tau_c = \lambda_c = 100$. Error bars are included but too small to be visible.

5.4 Comparing decoherence for different shuttling models

In this section, we compare the decoherence due to noise along all three axes to the analytical solutions for dephasing given in Eqs. (4.28)-(4.32) for shuttling where the random magnetic field is only along the z-axis. This means that rather than looking at only projection along the x-axis, we look at the decoherence factor according to Eq. (5.13)

Furthermore, we look at an alternate model for the random sheet where the correlations in the random sheet decay according to a Gaussian in space:

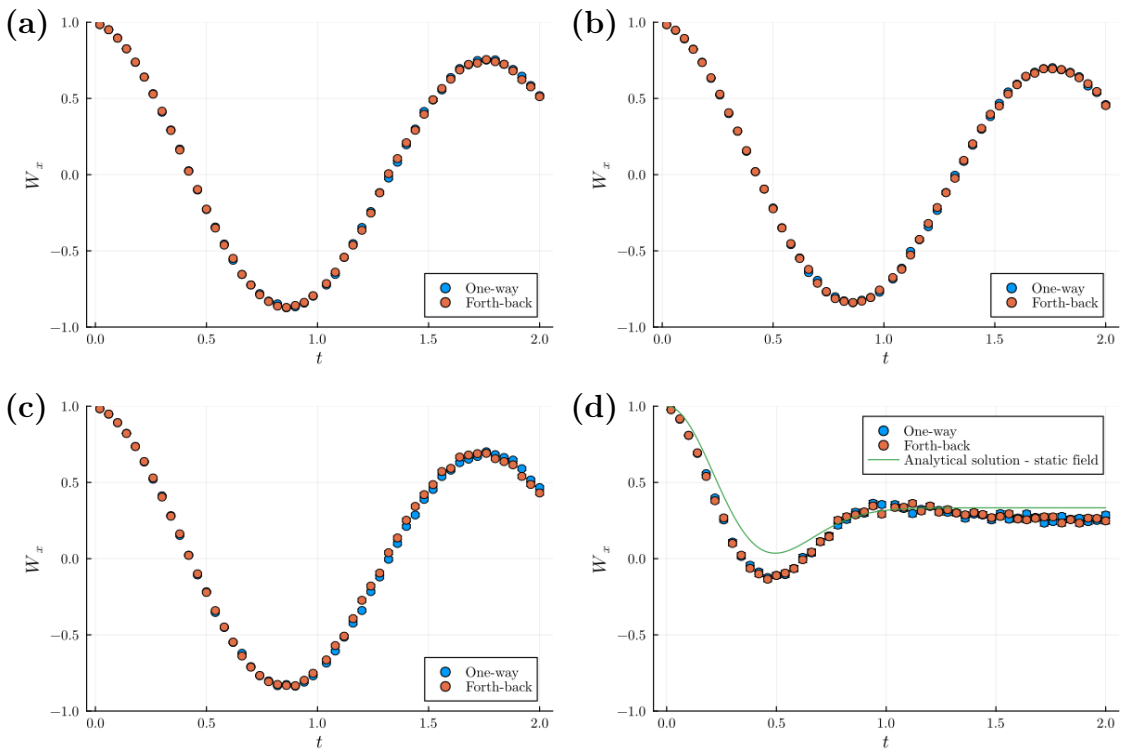

Figure 5.6: Plots showing how the average projection along the x-axis $W_x = 2\mathbb{E}[\langle S_x(t)\rangle]$ changes along the shuttling path for $\sigma_x = \sigma_y = 2\sigma_z = B_0 = 3.5$ and $T = L = 1$. **(a)**: $\tau_c = \lambda_c = 1/100$. **(b)**: $\tau_c = 1/100$, $\lambda_c = 100$. **(c)**: $\tau_c = 100$, $\lambda_c = 1/100$, **(d)**: $\tau_c = \lambda_c = 100$. Error bars are included but too small to be visible.

$$K_a(\theta_1, \theta_2) = \sigma_a^2 \exp\left(-\frac{1}{2}\kappa_x^2(x_1 - x_2)^2 - \kappa_t|t_1 - t_2|\right). \tag{5.18}$$

This model is motivated by considering the shape of the confined wave packet, which will be Gaussian. Generally, this model means that for positions where $|x_1 - x_2| < \lambda_x$, the correlation is stronger, while for $|x_1 - x_2| > \lambda_x$ the correlation is weaker.

Rather than looking at how decoherence evolves during shuttling, we look at the average decoherence at the end of a shuttling path for different shuttling times T, assuming a constant shuttling velocity v such that the shuttling length $L = vT$. The results in Fig. 5.7 show that there is less decoherence when the noise is only along the quantisation axis than when noise along the other axes is included. Furthermore, we observe that in general, there is more decoherence during forth-back shuttling, due to the resurfacing correlations as the spin returns to its original point. Finally, we observe that the Gaussian covariance function leads to increased decoherence compared to the exponentially decaying covariance function. This is likely because the Gaussian covariance function shows stronger correlation for distances below the correlation length, and correlated noise leads to increased decoherence.

To summarise the content of this chapter, we have presented a method which is provably convergent to calculate the average effect of a random magnetic field whose direction varies significantly. We demonstrated that this method gives accurate results with favourable scaling in the discretisation parameter N and the Monte

Carlo number M. We subsequently show that the method results in expected behaviour for shuttled spins, discussing various scenarios with different parameters. We confirm that the regime where forth-back shuttling most influences decoherence is the same as derived with the analytical solutions for the 1D random magnetic field model. We also look at the case where the random sheet's correlation in space decays according to a Gaussian function, which leads to increased decoherence in general when compared to an OU sheet. Additional steps towards verifying the accuracy of the method could be taken by taking a random magnetic field whose direction varies, and comparing the results to predictions made by Bloch-Redfield theory.

Having verified and applied the method, we can now turn to using it to simulate decoherence in Si, Ge, as well as analysing the effectiveness of dynamical decoupling sequences.

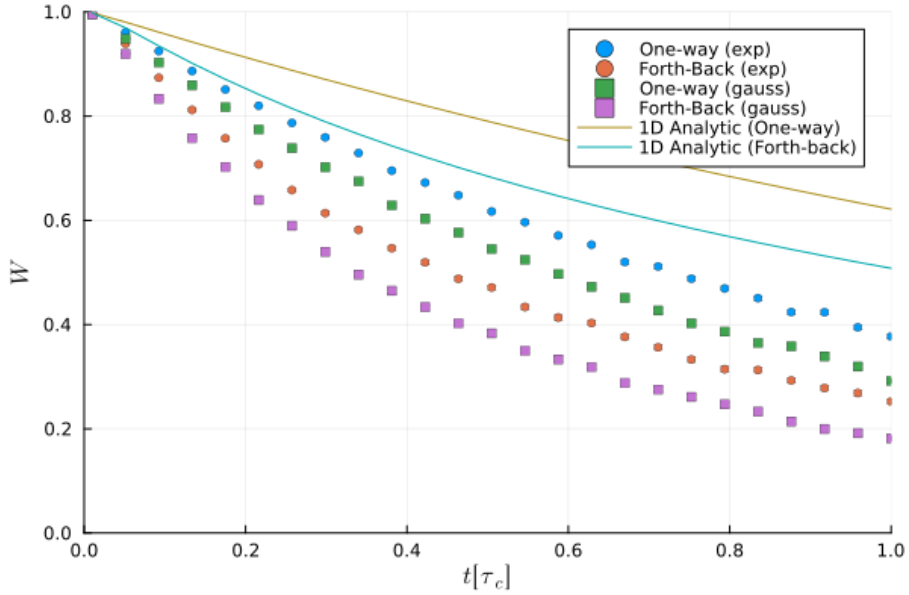

Figure 5.7: Comparison between different models of the decoherence for different shuttling times t. Solid lines representing analytical solutions are for a system where noise is only along the z-axis, given by Eqs. (4.28)-(4.32). The lines labelled "exp" refer to simulations where the random sheet's correlations in space decay exponentially in time, as for an OU sheet. The lines labelled "gauss" refer to simulations where the random sheet's correlations in space decay according to a Gaussian function. The parameters used are $\tau_c = \lambda_c = 1$, $\sigma_x = \sigma_y = \sigma_z = 3.5$, $B_0 = 0$, $v = 50$, $N = 300$, $M = 10^4$. Error bars are included but small enough to not be visible.

Chapter 6

Dynamical decoupling during shuttling

This chapter will focus on analysing and simulating dynamical decoupling (DD) sequences during shuttling. We introduce new DD sequences with a central pulse, which are predicted to be more effective at suppressing decoherence during forth-back shuttling. After a theoretical analysis of the sequences, we apply them to the shuttling of spins in a random magnetic field whose direction is strongly aligned along the z-axis, but includes random effects along all three axes. We obtain a comprehensive overview of dynamical decoupling during shuttling by considering many simulations for different velocities, shuttling lengths, waiting times, and pulses.

6.1 Average Hamiltonian theory

In this section, we analytically treat DD sequences. To perform this analysis, we rely on average Hamiltonian theory (AHT) [49, 50] to estimate the average effect of a random magnetic field during a sequence. We begin with a simple Hahn echo sequence, followed by the well-used XY4 and XY8 sequences. We then introduce the XY4-X, XY4-Z, XY8-X and XY8-Z sequences, which incorporate a central pulse halfway through a shuttling sequence. This pulse is expected to suppress decoherence during forth-back shuttling, where the random magnetic field forth and back paths is correlated.

6.1.1 Hahn echo

We first consider a simple sequence to introduce the concepts behind how DD sequences suppress decoherence and how AHT can be used to analyse DD sequences. The *Hahn Echo* [51] consists of the following sequence: Allow a spin to evolve for a certain time τ, then apply an X-pulse, then allow the spin to evolve for another time τ, and then apply another X-pulse. This sequence will be denoted by the notation $\mathrm{PX} \equiv \tau - X - \tau - X$, where X denotes a pulse that applies a π rotation about the x-axis, and τ denotes a free evolution for a duration τ. In the scenario where the free evolution is due to static noise along the z-axis (Eq. (4.1)), with the magnetic field B being some random variable β which is constant during the sequence, the evolution operator becomes

$$U = e^{-i\pi S_x} e^{-i\tau\beta S_z/2} e^{-i\pi S_x} e^{-i\tau\beta S_z/2} = I. \tag{6.1}$$

The effect of the static field has been completely removed due to the X-pulse, resulting in an echo when the evolution times on either side of the pulse are equal. For longer times, the spin will start to decoherence again, which can be further mitigated using repeated pulse sequences. This demonstrates how a simple DD can suppress the effect of quasi-static noise.

In the case where a random magnetic field along the z-axis is instead modelled as an OU process, this pulse sequence will also lead to refocussing. The dephasing at $t = 2\tau$, when a pulse is applied at $t = \tau$, becomes [52]

$$W_x(t = 2\tau) = \exp\left(-\frac{b^2}{\kappa^2}[2\kappa\tau - 3 + 4e^{-\kappa\tau} - e^{-2\kappa\tau}]\right), \tag{6.2}$$

$$\text{Short times: } t \ll \tau_c, \quad W_x(t) = \exp\left(\frac{-\kappa b^2 t^3}{12}\right), \tag{6.3}$$

$$\text{Long times: } t \gg \tau_c, \quad W_x(t) = \exp\left(\frac{-b^2 t}{\kappa}\right). \tag{6.4}$$

For short times, the correlations persist, allowing there to be some cancelling and therefore refocusing. The decay shape is now e^{-t^3} instead of the e^{-t^2} observed when no pulse is applied (see Eq. (4.23)), and the decoherence timescale is longer. This shows that for correlated noise, a decoupling pulse can reduce the effect of the noise on decoherence.

For long decoherence times, the pulses have no effect and there is no refocusing, and the result is the same as Eq. (4.24). This can be considered a consequence of the random magnetic field having a very short correlation time relative to the decoherence time, and as such, the evolution before and after the pulse is nearly uncorrelated. This is the motional narrowing regime discussed previously for Eq. (4.24)

A useful technique to analyse a DD sequence is to use the toggling frame and AHT. Consider a simple Hamiltonian $H = B_x S_x + B_y S_y + B_z S_z = H_x + H_y + H_z$, with each B_i constant in time. The total evolution in a PX sequence is given by the product of evolutions

$$U = XU_\tau XU_\tau = XX(X'U_\tau X)U_\tau, \tag{6.5}$$

where U_τ denotes a free evolution of the Hamiltonian for a duration τ, while $X = \exp(-i\pi S_x)$ is the X pulse. Using the fact that for any two matrices A, B, we have $A\exp(B)A^{-1} = \exp(ABA^{-1})$ (for derivation see Appendix A.2), we can reframe the second half of the evolution as

$$X'U_\tau X = X'\exp(-iH\tau)X = \exp(-i\tau(X'HX)) = \exp(-\tau H_2), \tag{6.6}$$

where we now have an evolution for the same duration τ but now under the action of the Hamiltonian H_2, which is the original Hamiltonian transformed to a new coordinate frame. Using products of Pauli matrices, we can derive that H_2 is given by

$$H_2 = H_x - H_y - H_z. \tag{6.7}$$

The total evolution is given by

$$\begin{aligned} U &= P_X^2 \exp\left(-i\tau(H_x - H_y - H_z)\right) \exp(-i\tau(H_x + H_y + H_z)) \\ &= \exp(-i\tau H_2) \exp(-i\tau H_1). \end{aligned} \tag{6.8}$$

Average Hamiltonian theory can be used to analyse a sequence of evolutions during a pulse sequence, where the evolution is written as

$$U = \exp\bigl(-i\bar{H}T\bigr), \tag{6.9}$$

with T the total duration of the sequence, and $\bar{H}$ the effective or average Hamiltonian, which can be written as a series expansion called the Magnus expansion:

$$\bar{H} = \bar{H}^{(1)} + \bar{H}^{(2)} + \bar{H}^{(3)} + ... \tag{6.10}$$

The first three orders of the expansions are

$$\bar{H}^{(1)} = \frac{1}{T}\int_0^T H(t)dt, \tag{6.11}$$

$$\bar{H}^{(2)} = \frac{1}{2iT}\int_0^T \int_0^t [H(t), H(t')]dt'dt, \tag{6.12}$$

$$\bar{H}^{(3)} = \frac{-1}{6T}\int_0^T \int_0^t \int_0^{t'} [H(t), [H(t'), H(t'')] + [[H(t), H(t')], H(t'')]dt''dt'dt. \tag{6.13}$$

Calculating the first-order average Hamiltonian for the PX sequence (making use of the toggling frame), we obtain

$$\bar{H}^{(1)} = H_x, \tag{6.14}$$

$$\bar{H}^{(2)} = \frac{1}{2}H_y - \frac{1}{2}H_z, \tag{6.15}$$

$$\bar{H}^{(3)} = -\frac{2}{3}H_x, \tag{6.16}$$

and we observe that, to the first order, the PX sequence has eliminated the evolution due to H_y and H_z. This example gives a basic idea of how the toggling frame and AHT can be used to analyse pulse sequences. In general, more sophisticated decoupling sequences will eliminate evolution along more than three axes for higher orders.

While both the Magnus expansion and AHT provide powerful frameworks for analysing the time evolution under time-dependent Hamiltonians, it is important to recognise that the Magnus expansion is a formal series. It is not, in general, asymptotic or guaranteed to converge. However, it is a powerful heuristic tool that has been used extensively to great success.

6.1.2 Decoupling sequences for shuttling

We first consider the well-used XY4 and XY8 sequences [53, 54]:

$$\text{XY4} \equiv \tau - X - 2\tau - Y - 2\tau - X - 2\tau - Y - \tau, \tag{6.17}$$

$$\begin{aligned}\text{XY8} \equiv\ & (\tau - X - 2\tau - Y - 2\tau - X - 2\tau - Y - \tau) \\ & - (\tau - Y - 2\tau - X - 2\tau - Y - 2\tau - X - \tau),\end{aligned} \tag{6.18}$$

where, although the pulse sequences appear to have different lengths, the evolution times are adjusted such that the sequence takes place over the whole duration during which the spin is being shuttled.

These two sequences are effective in reducing the influence of noise along all three axes. Throughout this section, we assume that over the course of the shuttling duration, the evolution is governed by a static Hamiltonian $H = H_x + H_y + H_z$. We find the toggling frame for the XY4 sequence given in Tab. 6.1, and the XY8 sequence in Tab. 6.2. For both sequences, the first-order average Hamiltonian is zero.

The toggling frame and AHT provide an intuitive understanding of how DD sequences work. When a random magnetic field along a given axis remains strongly correlated before and after a pulse that inverts the effective magnetic field along that axis, the pulse can induce refocusing. In general, increasing the number of pulses reduces the time between them, so the field has less time to become uncorrelated. This results in a stronger correlation between evolution segments on either side of a pulse, enhancing the effectiveness of the sequence. However, in the case of forth-back shuttling and other shuttling types, correlations do not simply decay during the sequence. Recall Fig. 4.1(c), where we observed that in the case of forth-back shuttling in a random sheet, correlations will resurface as the spin returns to the original point. We have to take into account that when a spin is travelling backwards, it is passing through the same space as forwards. This invites us to consider that it may be more effective to ensure that when passing through the same space forwards and backwards, the effective Hamiltonian is as anticorrelated as possible. In the case of a simple PX sequence, this is already the case. However, in the symmetric XY8 protocol, the effective Hamiltonian is repeatedly the same at same points in space, as can be seen in Table 6.2 (mirroring the blue region onto the red region). Also, in the XY4 protocol, the toggling frame during the initial and final evolution is the same.

Motivated by the goal to suppress the effect of the random magnetic field being correlated during the forth and the back half of a forth-back shuttling path, we have devised new dynamical decoupling sequences designed for shuttling:

$$\text{XY4-X} \equiv \tau - X - 2\tau - Y - \tau - X - \tau - X - 2\tau - Y - \tau - X, \tag{6.19}$$

$$\text{XY4-Z} \equiv \tau - X - 2\tau - Y - \tau - Z - \tau - X - 2\tau - Y - \tau - Z, \tag{6.20}$$

$$\begin{aligned}\text{XY8-X} \equiv\ & (\tau - X - 2\tau - Y - 2\tau - X - 2\tau - Y - \tau) - X \\ & - (\tau - Y - 2\tau - X - 2\tau - Y - 2\tau - X - \tau) - X,\end{aligned} \tag{6.21}$$

$$\begin{aligned}\text{XY8-Z} \equiv\ & (\tau - X - 2\tau - Y - 2\tau - X - 2\tau - Y - \tau) - Z \\ & - (\tau - Y - 2\tau - X - 2\tau - Y - 2\tau - X - \tau) - Z.\end{aligned} \tag{6.22}$$

For the XY4-X and XY4-Z protocol, we have shown the toggling frame in Tab. 6.1, where we observe that the toggling frames during the forward and backwards

Table 6.1: Toggling frame during the XY4 (Eq. (6.17)), XY4-X (Eq. (6.19)), and XY4-Z (Eq. (6.20)) pulse sequence. During shuttling, we distinguish between the toggling frame in the forward half (Blue) and the backwards half (Red). Summing up the terms in a column gives the first-order effective Hamiltonian (excluding normalisation by a factor 8τ).

		XY4			XY4-X			XY4-Z		
	Duration (τ)	H_x	H_y	H_z	H_x	H_y	H_z	H_x	H_y	H_z
	1	+	+	+	+	+	+	+	+	+
	2	+	-	-	+	-	-	+	-	-
	1	-	-	+	-	-	+	-	-	+
	1	-	-	+	-	+	-	+	+	+
	2	-	+	-	-	-	+	+	-	-
	1	+	+	+	+	-	-	-	-	+
Total	8	0	0	0	0	$-4\tau H_y$	0	$4\tau H_x$	$-4\tau H_y$	0

parts of the shuttling are different. For the XY4-X sequence, we do have a leftover H_y term in first-order AHT, implying that even in the first order a this sequence will not fully mitigate decoherence due to a static field (as opposed to XY4). For XY4-Z, the leftover term contains both H_x and H_y terms, indicating even worse performance. For the XY8-X and XY8-Z sequences, we have included the toggling frame in Tab. 6.2, where we again observe different toggling frames during the forwards and backwards shuttling. Like the XY8 sequence, the XY8-X and XY8-Z sequences have no leftover first-order terms.

The effectiveness of the introduced pulse sequences can be analysed by calculating the effective Hamiltonian at different orders. These results are shown in Tab. 6.3. We observe that for the X, XY4-X and XY4-Z sequences, there are leftover terms at first order. For XY4 and XY8-X, the first non-zero terms are at second order, while for XY8, the first non-zero terms are at third order. For the XY8-Z protocol, there are only terms at higher orders than three. For symmetric protocols such as XY8, all even terms of the effective Hamiltonian are zero [50]. These results are reflected when considering each sequence for a random static magnetic field, shown in Fig. 6.1. For increasing time t, we calculate the average shuttling fidelity F (given by Eq. (5.14)) for a quasi-static random magnetic field for different decoupling sequences. We observe that the X, XY4-X, and XY4-Z sequences lead to the lowest fidelities, followed by the XY4 and XY8-X sequences and finally the XY8 sequence and then XY8-Z. This hierarchy is reflected in the AHT calculations in Tab. 6.3.

We have seen that applying X and Y pulses leads to an inversion of the Hamiltonian along the other axes. When we model the random magnetic field, we will consider the magnetic field along each axis to be independent and correlated only along the same axis. This may lead to pulses along the same set of axes to overperform. As such, we will also consider sequences where, rather than applying pulses along the x and y axis, we apply the pulse X$'$ along the line $[1, 1, 0]$ and the pulse Y$'$ along $[1, -1, 0]$. Importantly, X$'$ and Y$'$ are still orthogonal, and still perform a π rotation. However, now the X' pulse leads to the transformation of the Hamiltonian as $H_{x,y} \to H_{y,x},\ H_z \to -H_z$, and Y' leads to $H_{x,y} \to -H_{y,x},\ H_z \to -H_z$. This set

Table 6.2: Toggling frame during the XY8 (Eq. 6.18), XY8-X (Eq. 6.21) and XY8-Z (Eq. 6.22) sequence. During shuttling, we distinguish between the toggling frame in the forward half (Blue) and the backwards half (Red). Summing up the terms in a column gives the first-order effective Hamiltonian (excluding normalisation by a factor 16τ).

		XY8			XY8-X			XY8-Z		
	Duration (τ)	H_x	H_y	H_z	H_x	H_y	H_z	H_x	H_y	H_z
	1	+	+	+	+	+	+	+	+	+
	2	+	-	-	+	-	-	+	-	-
	2	-	-	+	-	-	+	-	-	+
	2	-	+	-	-	+	-	-	+	-
	1	+	+	+	+	+	+	+	+	+
	1	+	+	+	+	-	-	-	-	+
	2	-	+	-	-	-	+	+	-	-
	2	-	-	+	-	+	-	+	+	+
	2	+	-	-	+	+	+	-	+	-
	1	+	+	+	+	-	-	-	-	+
Total	16	0	0	0	0	0	0	0	0	0

Table 6.3: First-, second-, and third-order average Hamiltonians for different decoupling sequences, each defined by the toggling frames in Tabs. 6.1, 6.2, and Eqs. (6.11)-(6.13)

Pulse sequence	$H^{(1)}$	$H^{(2)}$	$H^{(3)}$
None	$H_x + H_y + H_z$	0	0
X	H_x	$\frac{1}{2}H_y - \frac{1}{2}H_z$	$-\frac{2}{3}H_x$
XY4	0	$-\frac{1}{2}H_z$	$\frac{1}{4}H_x + \frac{1}{4}H_y$
XY4-X	$-\frac{1}{2}H_y$	$\frac{1}{8}H_y - \frac{1}{4}H_z$	$-\frac{1}{4}H_x + \frac{23}{48}H_y + \frac{1}{8}H_z$
XY4-Z	$\frac{1}{2}H_x - \frac{1}{2}H_y$	$-\frac{1}{8}H_x + \frac{1}{8}H_y - \frac{1}{2}H_z$	$-\frac{17}{48}H_x + \frac{17}{48}H_y - \frac{1}{6}H_z$
XY8	0	0	$\frac{1}{4}H_x + \frac{1}{4}H_y$
XY8-X	0	$-\frac{1}{2}H_z$	$\frac{1}{4}H_x$
XY8-Z	0	0	0

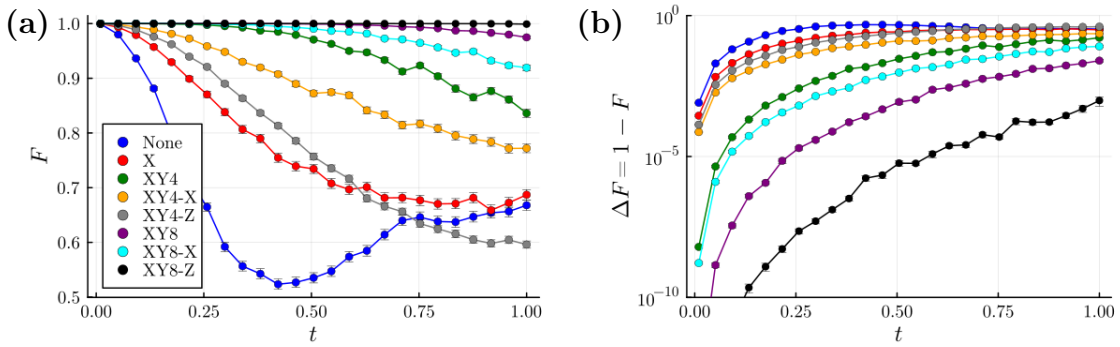

Figure 6.1: Dependence of average fidelity F of a stationary qubit on evolution time t under a static random magnetic field $H = \tilde{\mathbf{B}} \cdot \mathbf{S}$, for different decoupling sequences. The static random magnetic field is a three-component Gaussian distribution with each component having mean $\mu = 0$ and variance $\sigma_B^2 = 4$. Simulation parameters are $N = 320$, $M = 10^3$. Both figures show the same results, with **(a)**: Fidelity F as a function of time, and **(b)**: Infidelity $\Delta F = 1 - F$ as a function of time with a log scale.

of pulses will be referred to as "XY45", as they are rotated 45° w.r.t. the original X, Y pulses.

Although we have not considered the ability of DD sequences to suppress decoherence due to varying magnetic fields, these results give insight into the nature of various pulse sequences. We will analyse the effectiveness of these sequences at suppressing decoherence due to a random magnetic field during shuttling in this Chapter and Chapter 7.

Throughout this section, we have assumed that the applied pulses are perfect and instantaneous. In reality, this is not the case. The instantaneousness of the pulses can be problematic when modelling shuttling. Firstly, we do not include the fact that the qubit may need to be stationary for a duration in order to apply a pulse. Secondly, the actual shape of the pulse depends on how it is implemented. It does not implement a direct spin flip, but a continuous rotation over the duration of the pulse. One way to analyse imperfect pulses is by modelling each pulse as a rotation by an angle $\pi + \epsilon$ rather than the ideal π rotation. These considerations can be taken into account if we want to investigate how these faults influence the effectiveness of different pulse sequences. For the work in this thesis, the pulses are considered perfect and instantaneous.

6.2 Simulation parameters

For the remainder of this chapter, we will consider a model where the Hamiltonian is given by

$$H(x,t) = B_0 S_z + \tilde{\mathbf{B}}_{\text{eff}}(x,t) \cdot \mathbf{S}, \tag{6.23}$$

where B_0 is a deterministic magnetic field significantly larger than the variance of $\tilde{\mathbf{B}}_{\text{eff}}$. The random magnetic field $\tilde{\mathbf{B}}_{\text{eff}}$ has the same properties as in Chapter 5: It is a 3-component random process where each random process is derived from an

Table 6.4: Parameters used for Figs. 6.2-6.8, including shuttling length and times, correlation scales, and deterministic & random magnetic field strengths. Adapted from [19].

Parameter	Experimental value	Simulation value	Description
T_2^*	$20\mu s$	$1\tau_c$	Decoherence time
σ_B	-	$\sqrt{\frac{2}{3}}(\tau_c)^{-1}$	Variance of random field
T_{fast}	$2\mu s$	$0.1\tau_c$	"Fast" shuttling time
T_{slow}	$20\mu s$	$1\tau_c$	"Slow" shuttling time
L	$10\mu m$	$100\lambda_c$	Shuttling length
τ_c	$20\mu s$	1	Correlation time
λ_c	$0.1\mu m$	1	Correlation length
B_0	-	$30\sigma_B$	Quantising magnetic field
t_w	$2\mu s$	$0.1\tau_c$	Waiting time

independent OU sheet with same correlation time τ_c and correlation length λ_c, and here we consider that they have the same variance σ_B^2.

We will only consider forth-back shuttling, through a bus of length L where the total shuttling time is $2T + 2t_w$. T is the time it takes to move from $x = 0$ to $x = L$ at constant velocity $v = L/T$. We also consider a waiting time $2t_w$, which we use to analyse what the effect of waiting during forth-back shuttling has on the decoherence. The motivation for this is the goal to model shuttling with a two-qubit ZZ gate, according to the sequence (excluding any DD)

$$U = U_b \exp(-i\alpha Z_1 Z_2) U_a \tag{6.24}$$

where U_a is the evolution during the forward shuttling, and U_b is the evolution during the backward shuttling. Intermittently, we apply the two qubit gate between the shuttled qubit (qubit 1), and another arbitrary qubit (qubit 2). The duration required to apply this operation is the waiting time $2t_w$, during which the shuttled qubit is stationary.

The parameters we use for these simulations are listed in Tab. 6.4. Before performing simulations, let us analyse these parameters to give an overview of the system we are simulating. Firstly, the variance σ_B^2 is derived from T_2^* such that $\sigma = \frac{\sqrt{2}}{T_2^*}$ and $\sigma^2 = \sigma_x^2 + \sigma_y^2 + \sigma_z^2 = 3\sigma_B^2$. The quantising magnetic field B_0 is 30 times larger than the standard deviation of the random field, meaning that the direction of the magnetic field will only vary by about 2% in all directions. We distinguish between two shuttling times termed "fast" and "slow" shuttling. The fast shuttling time T_{fast} is much less than the correlation time τ_c, meaning the correlations in time will only decay slightly. In slow shuttling, the correlations will decay significantly over the course of the shuttling time (by 90% over a duration $2T_{\text{slow}} = 2\tau_c$). The shuttling length L is significantly longer than the correlation length λ_c, so during shuttling the correlations in space decay very quickly.

A useful way to analyse the effect of the parameters defining the random sheet on the forth-back path is to image the covariance matrix along the path [25]. In Fig. 6.2, the highest correlations are observed in a cross shape, as well as a central square. The cross shape results from points along the shuttling path only being strongly correlated with two points: The point itself, and the same point during the

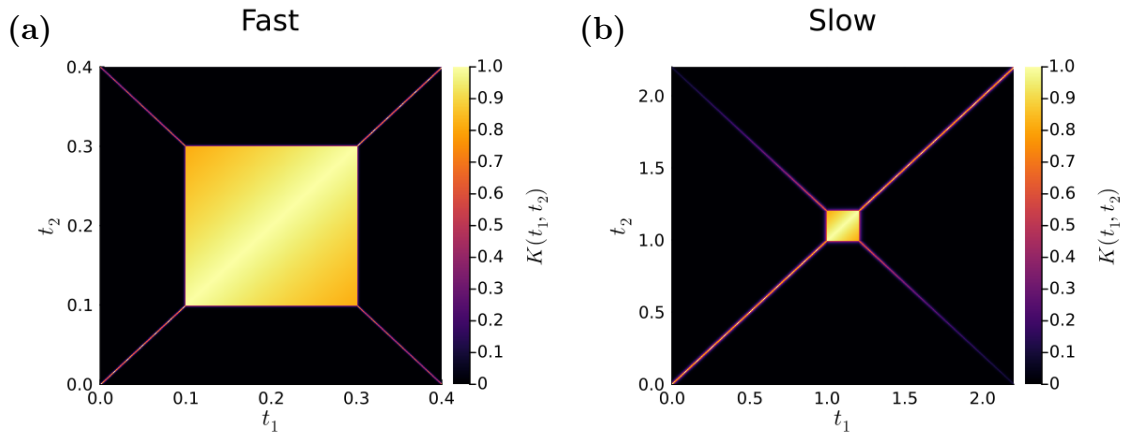

Figure 6.2: Covariance function (Eq. (5.3)) for the random magnetic field along a forth-back path, derived from an OU sheet. Parameters used are $L = 100\lambda_c$, $\sigma_B = 1$, $t_w = 0.1\tau_c$; **(a)**: $T = 0.1\tau_c$, **(b)**: $T = 1\tau_c$.

other half of the shuttling path, where the same space is traversed. The correlation with any other points quickly decays due to the correlation length λ_c being very small relative to the shuttling length L. In the case of slow shuttling in Fig. 6.2(b), we observe that the correlations between the same positions on forth-half and the back-half of the path are lower as a longer period of time has passed, on the order of the correlation time τ_c.

The central square represents the waiting period. We consider a waiting time $t_w = 0.1\tau_c$, which means that during the total waiting time $2t_w$, the correlation decays by approximately 20%, meaning the random magnetic fields along the forwards and backwards paths of the shuttling are still strongly correlated. Furthermore, this means that during the waiting period the random magnetic field is quasi-static, as opposed to the motional narrowing regime during shuttling. When applying DD sequences to shuttling with waiting time, we apply the sequences over the *whole* shuttling, with total time $2T + 2t_w$. An alternate method would be to apply a sequence during shuttling forwards, then a specific sequence during the waiting time, and then a sequence backwards. We briefly discuss this in Appendix A.4.

The most important observation is that during shuttling, we are in the motional narrowing regime, while during waiting, we are in the quasi-static regime, and that there is always a degree of correlation between the forth and the back paths.

6.3 Simulations of DD sequences during forth-back shuttling

We apply the DD sequences during shuttling in a system defined by the introduced parameters. We measure the effectiveness of a DD sequence by comparing either the decoherence factor W, given by Eq. (5.13), or the average fidelity F, given by Eq. (5.14). For fidelity we account for the deterministic rotation in the case that no pulses are applied. In each figure, we plot the measured W or F at the *end* of a forth-back shuttling sequence for varying shuttling parameters including the shuttling velocity v, shuttling length L, or waiting time t_w. We do not plot how

decoherence or infidelity accumulates *during* a shuttling path, as was the case in Chapter 5.

It is important to emphasise that when studying the decoherence factor W, the results are specific to the chosen initial state along the x-axis. We therefore define **x-decoherence** as the measured decoherence factor W at the end of a shuttling path, for a spin initialised along the x-axis. This is to avoid confusion with general decoherence applicable to arbitrary initial state. This important as certain DD sequences show a high effectiveness for the chosen initial state. We will distinguish between statements that apply to decoherence in general, and statements that only apply to x-decoherence. The average fidelity F requires no such distinction as it already takes into account all possible initial states.

The simulation results are displayed in Figs. 6.3-6.8. In Fig. 6.3(a), we show the loss of coherence for a spin initialised along the x-axis for increasing dimensionless shuttling velocity, where for all sequences the x-decoherence decreases as shuttling velocity increases. This is expected, as the faster the shuttling, the lower the time during which decoherence can occur. For low shuttling velocities, we observe a lower x-decoherence for the set of sequences with a central X pulse: X (which refers to the PX sequence), XY4-X, and XY8-X, when compared to sequences without a central X pulse: None, XY4, XY4-Z, XY8, and XY8-Z. This indicates that a central pulse does suppress x-decoherence for forth-back shuttling as we predicted. The reason that the XY8-Z sequence does not show the same level of suppression is likely because the spin is initialised along the x-axis. Towards the higher velocities, XY8-X leads to the lowest loss of coherence for a spin initialised along the x-axis. The well-used XY4 and XY8 sequences are not at all effective at reducing the loss of coherence. This is likely due to the very short coherence length λ_c, which prevents the pulses from leading to any refocusing, as the random magnetic fields during different evolutions become uncorrelated too quickly.

Fig. 6.3(b) shows the results when waiting time is included. For high velocities, all sequences now suppress x-decoherence to an extent. This is because (depending on the velocity), we are applying pulses during the waiting period, where the random magnetic field is quasi-static. This allows the DD sequences to be effective at suppressing decoherence of a spin initialised along the during this waiting period. The XY8-X and XY8-Z sequences stand out as most effective, as they also suppress decoherence due to spatial correlations.

Fig. 6.3(c) we observe that, when applying the XY-45 pulses instead of pulses along the x- and y-axis, only the XY8-X sequence shows a noticeable reduction in effectiveness. This is likely related to the pulse axis of the central pulse no longer being parallel to the initial state along the x-axis.

Equivalent simulations using average fidelity instead of x-decoherence are shown in Fig. 6.4. In Fig. 6.4(a), we observe that XY8-X and XY8-X maintain fidelity equally well, supporting the hypothesis that the improved performance of XY8-X over XY8-Z in decoherence suppression in Fig. 6.3(a) was due to the chosen initial state. Overall, the results are very similar between fidelity and x-decoherence. In Fig. 6.4(b), where waiting time is included, we observe a crossover point after $v = 600$ where XY8-Z outperforms XY8-X. The velocity determines the shuttling time T, and therefore affects whether pulses occur during shuttling or during waiting. At $v > 600$, the second X pulse of the sequence occurs during the waiting time. The inclusion of this pulse (and its symmetric counterpart) during the waiting period,

where the field is quasi-static, suppresses decoherence more for the XY8-Z sequence than for the XY8-X sequence, hence the crossover. Fig. 6.4(c) shows no difference when applying XY-45 pulses.

We come to an important conclusion. The relation between waiting time and shuttling time is important when we consider DD sequences applied over the whole duration of a forth-back shuttling. The exact placement of pulses during a shuttle can lead to inflection points depending on the shuttling time/waiting time, which we will observe in subsequent figures.

Next, we vary the shuttling length L, maintaining a constant velocity. In Fig. 6.5 we observe the loss of coherence of a spin initialised along the x-axis for increasing shuttling lengths, for fast ($v = 1000$), and slow ($v = 100$), shuttling, where we look at both scenarios with and without waiting time. During fast shuttling, XY8-X results in the lowest x-decoherence. In Fig. 6.5(b), we observe multiple inflection points, such as the inflection at $L \approx 15$ for XY8, XY8-X, XY8-Z. This is a result of the first X pulse of the sequence occurring before the waiting period for $L > 15$. At $L = 100$, we observe that all sequences effectively suppress x-decoherence for a spin initialised along the x-axis, with the XY8-X and XY8-Z sequences showing significantly increased effectiveness.

During slow shuttling shown in Figs. 6.5(c) and (d), we again observe that only the sequences with a central X pulse are effective at suppressing x-decoherence, with all other sequences showing very limited effectiveness, independent of whether a waiting time is included or not.

The same simulations using average fidelity instead are shown in Fig 6.6. For fast shuttling, XY8-Z is now most effective at maintaining fidelity, both with and without waiting time. When no waiting time is included, the impact of DD sequences at increasing shuttling fidelity is limited. However, when waiting time is included, all sequences show increased shuttling fidelity.

For slow shuttling, we repeat the observation that sequences with a central X pulse are most effective at increasing shuttling fidelity. Interestingly, when waiting time is included, it is the sequences with a central Z pulse that do not show any increased shuttling fidelity, while the XY4 and XY8 sequences do show some effectiveness.

The final independent variable we analyse the effect of is the waiting time t_w. The results for x-decoherence are shown in Fig. 6.7. As a reference value, recall that in the previous figures we looked at a waiting time of $t_w = 0.1\tau_c$. For increasing waiting time, the spin spends more time in a quasi-static random magnetic field, resulting in increased x-decoherence, for both fast and slow shuttling. For fast shuttling, all sequences show a similar effectiveness at suppressing x-decoherence. For slow shuttling, the same is true for all but the XY4 and XY4-Z sequences, which are largely ineffective. For these sequences, before $t_w \approx 0.3$, none of the X/Y, pulses occur during the waiting, meaning the X/Y pulses only occur during the motional narrowing regime during shuttling, where they are ineffective. After $t_w \approx 0.3$, they show some effectiveness at suppressing decoherence.

When looking at average fidelity in Fig. 6.8, we observe similar characteristics in general, though the performance of XY8-Z is improved compared to XY8-X. This indicates that the XY8-X shows high effectiveness when the state is initialised along the x-axis; however, averaged over all states, the XY8-Z sequence is more effective.

In the case where we use the XY-45 pulse axes, the observable difference is not

substantial. The only significant difference is in XY8-X between Figs. 6.7(a) and (b), where we again predict that the difference comes as a result of the central pulse no longer being parallel to the initial state along the x-axis. This hypothesis is supported by the fact that in the case where we measure average fidelity in Fig 6.8, the difference between XY and XY-45 is no longer visible.

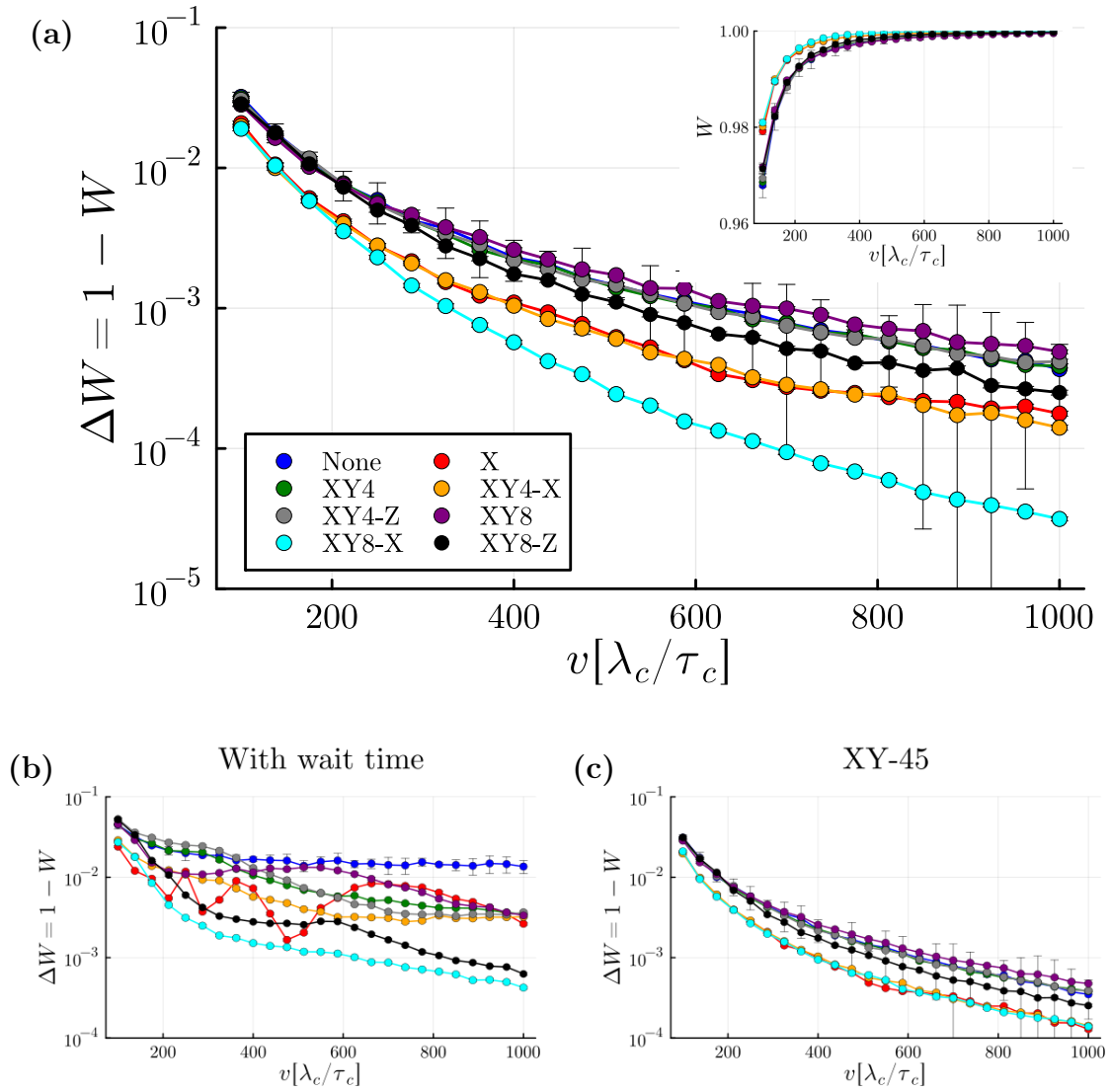

Figure 6.3: Dependence of **decoherence** W of a spin initialised along the x-axis, measured at the end of a forth-back shuttling path, on the **shuttling velocity** $v = L/T$ in different scenarios. During shuttling, the spin travels at a constant velocity v, except when it is stationary for a duration $2t_w$ at $x = L = 100\lambda_c$. The random magnetic field acting on the shuttled spin is strongly along the z-axis, and given by the Hamiltonian in Eq. (6.23). Parameters are listed in Tab. 6.4. Legend in **(a)** applies to all figures. We plot $\Delta W = 1 - W$ on a logarithmic y-axis, with the inset in **(a)** showing decoherence W. Notice that y-axis ranges differ. **(a)**: no waiting time ($t_w = 0$). **(b)**: Includes waiting time $t_w = 0.1\tau_c$. **(c)**: no waiting time ($t_w = 0$), but X and Y pulse axes in DD sequences are rotated 45°. Results generated using $N = 320$, $M = 10^3$. Error bars are present in each figure, though may be too small to be visible

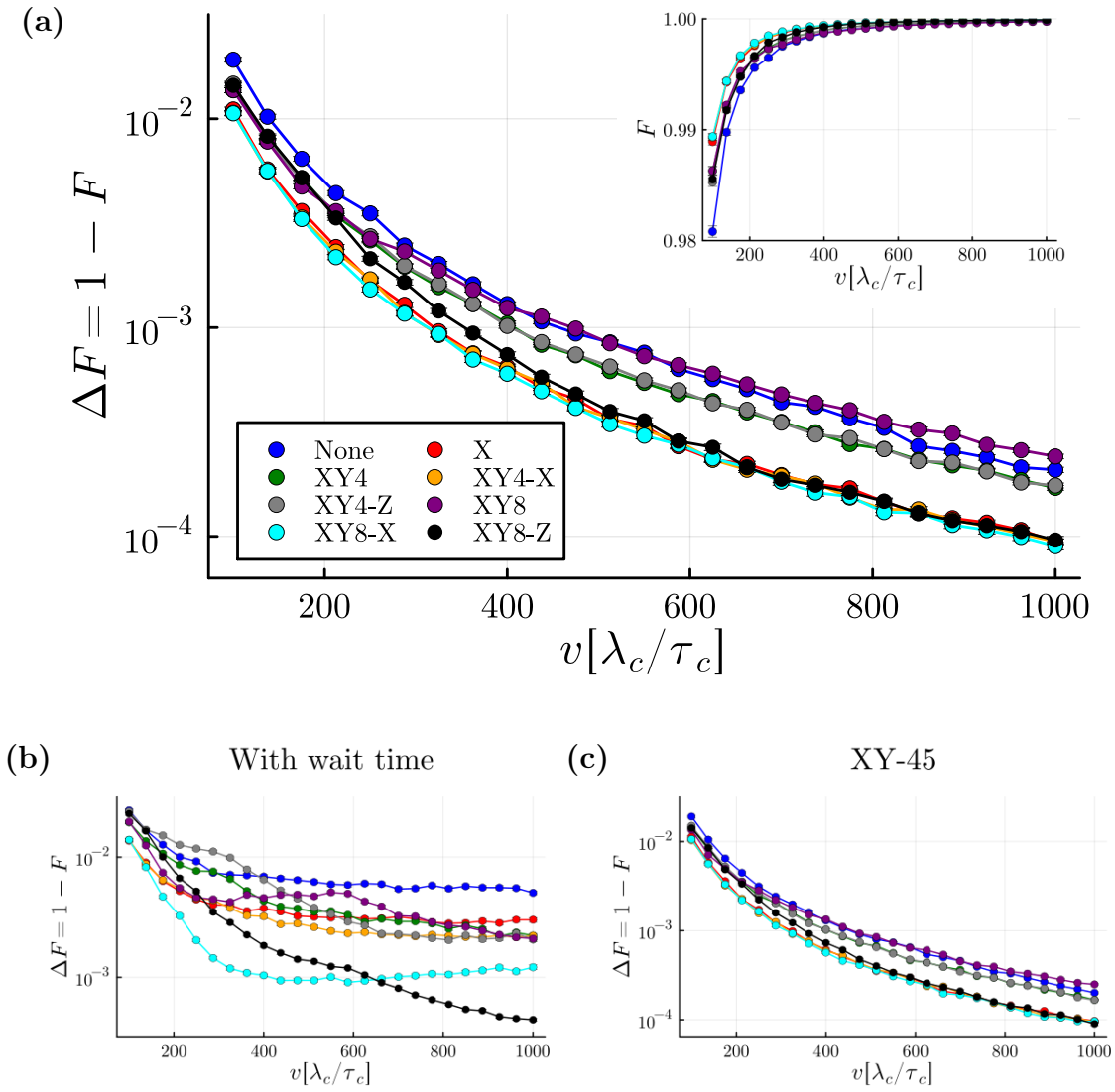

Figure 6.4: Dependence of **average fidelity** F, measured at the end of the forth-back shuttling path, on the **shuttling velocity** $v = L/T$ in different scenarios. During shuttling, the spin travels at a constant velocity v, except when it is stationary for a duration $2t_w$ at $x = L = 100\lambda_c$. The random magnetic field acting on the shuttled spin is strongly along the z-axis, and given by the Hamiltonian in Eq. (6.23). Parameters are listed in Tab. 6.4. Legend in **(a)** applies to all figures. We plot infidelity $\Delta F = 1 - F$ on a logarithmic y-axis, with the inset in **(a)** showing fidelity F. Notice that y-axis ranges differ. **(a)**: no waiting time ($t_w = 0$). **(b)**: Includes waiting time $t_w = 0.1\tau_c$. **(c)**: no waiting time ($t_w = 0$), but X and Y pulse axes in DD sequences are rotated 45°. Results generated using $N = 320$, $M = 10^3$. Error bars are present in each figure, though may be too small to be visible

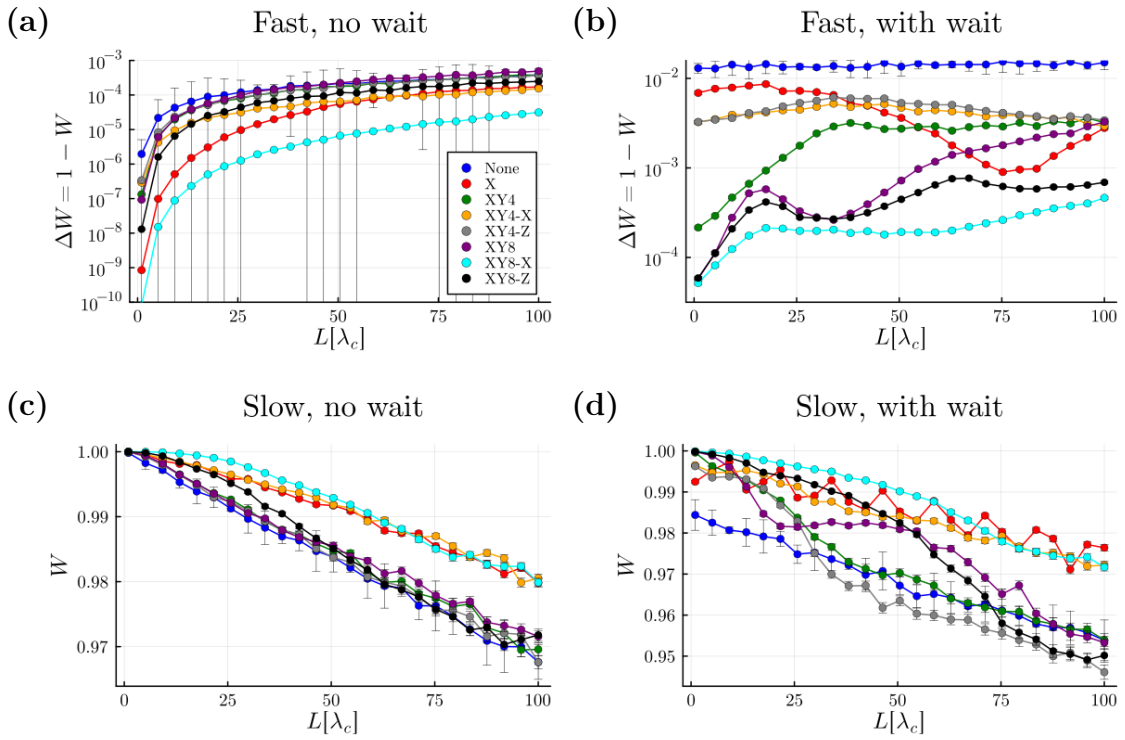

Figure 6.5: Dependence of **decoherence** W of a spin initialised along the x-axis, measured at the end of the forth-back shuttling path, on the **shuttling length** L in different scenarios. During shuttling, the spin travels at a constant velocity $v = L/T$, with T the shuttling time, except when it is stationary for a duration $2t_w$ at $x = L$. The random magnetic field acting on the shuttled spin is strongly along the z-axis, and given by the Hamiltonian in Eq. (6.23). Parameters are listed in Tab. 6.4. Legend in **(a)** applies to all figures. **(a)**, (**b**) show $\Delta W = 1 - W$ on a logarithmic y-axis, while **(c)**, (**d**) show decoherence W on a linear scale. Notice that y-axis ranges differ. **(a)**, **(b)**: Fast shuttling with shuttling velocity $v = 10^3\ \lambda_c/\tau_c$. **(c)**, **(d)**: Slow shuttling with shuttling time $v = 10^2\ \lambda_c/\tau_c$. For **(a)**, **(c)**: waiting time $t_w = 0$. For **(b)**, **(d)**: waiting time $t_w = 0.1\tau_c$. Results generated using $N = 320$, $M = 10^3$. Error bars are present in each figure, though may be too small to be visible.

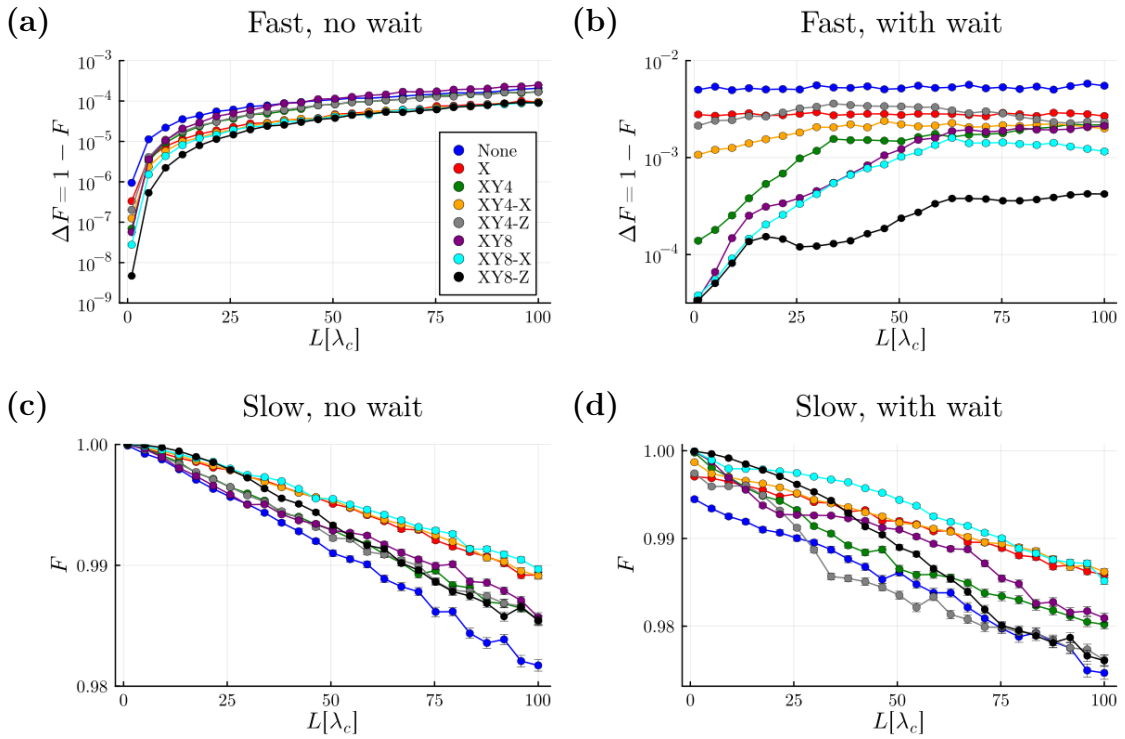

Figure 6.6: Dependence of **average fidelity** F, measured at the end of the forth-back shuttling path, on the **shuttling length** L in different scenarios. During shuttling, the spin travels at a constant speed $v = L/T$, with T the shuttling time, except when it is stationary for a duration $2t_w$ at $x = L$. The random magnetic field acting on the shuttled spin is strongly along the z-axis, and given by the Hamiltonian in Eq. (6.23). Parameters are listed in Tab. 6.4. Legend in **(a)** applies to all figures. **(a)**, (**b**) show infidelity $\Delta F = 1 - F$ on a logarithmic y-axis, while **(c)**, (**d**) show fidelity F on a linear scale. Notice that y-axis ranges differ. **(a)**, (**b**): Fast shuttling with shuttling velocity $v = 10^3\ \lambda_c/\tau_c$. **(c)**, **(d)**: Slow shuttling with shuttling time shuttling velocity $v = 10^2\ \lambda_c/\tau_c$. **(a)**, **(c)**: waiting time $t_w = 0$. **(b)**, **(d)**: waiting time $t_w = 0.1\tau_c$. Results generated using $N = 320$, $M = 10^3$. Error bars are present in each figure, though may be too small to be visible.

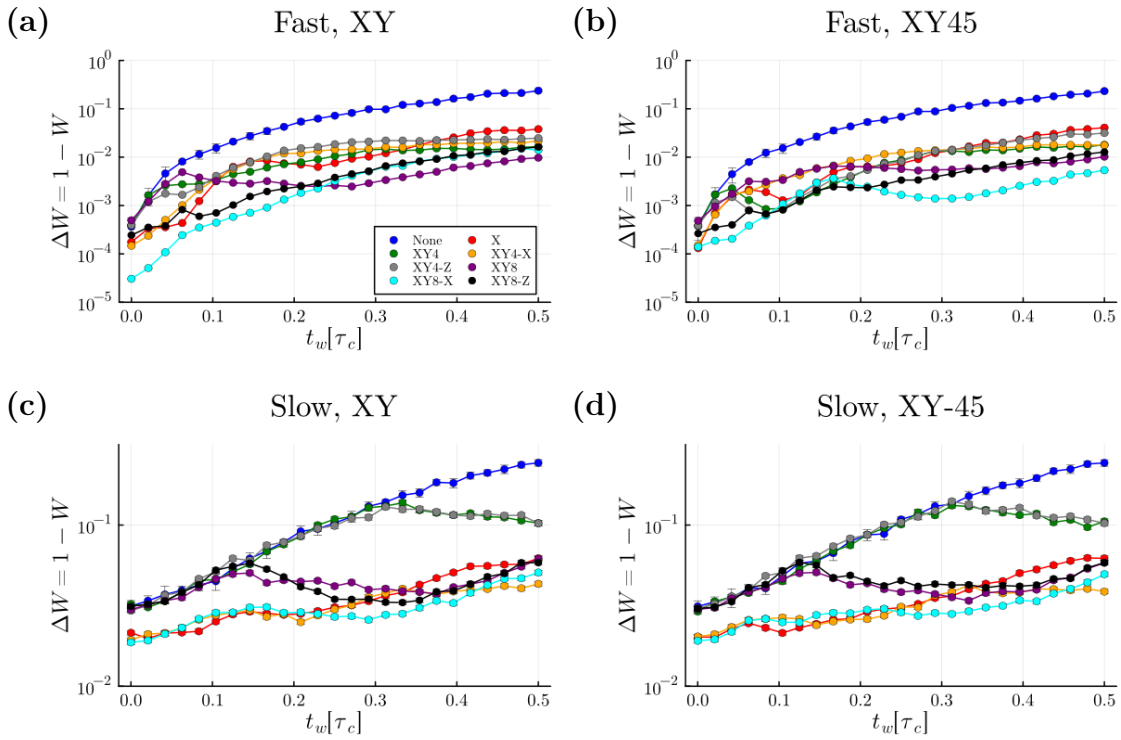

Figure 6.7: Dependence of **decoherence** W of a spin initialised along the x-axis, measured at the end of the forth-back shuttling path, on the **waiting time** t_w in different scenarios. During shuttling, the spin travels at a constant speed $v = L/T$, except when it is stationary for a duration $2t_w$ at $x = L = 100\lambda_c$. The random magnetic field acting on the shuttled spin is strongly along the z-axis, and given by the Hamiltonian in Eq. (6.23). Parameters are listed in Tab. 6.4. Legend in **(a)** applies to all figures. All figures show ΔW on a logarithmic y-axis. Notice that y-axis ranges differ. **(a)**, **(b)**: Fast shuttling with shuttling time $T = 0.1\tau_c$. **(c)**, **(d)**: Slow shuttling with shuttling time $T = 1\tau_c$. **(a)**, **(c)**: X, Y pulses in the DD sequences are along the x- and y-axis. **(b)**, **(d)**: X, Y pulses in the DD sequences are along the lines $[1, 1, 0]$ and $[1, -1, 0]$ respectively. Results generated using $N = 320$, $M = 10^3$. Error bars are present in each figure, though may be too small to be visible.

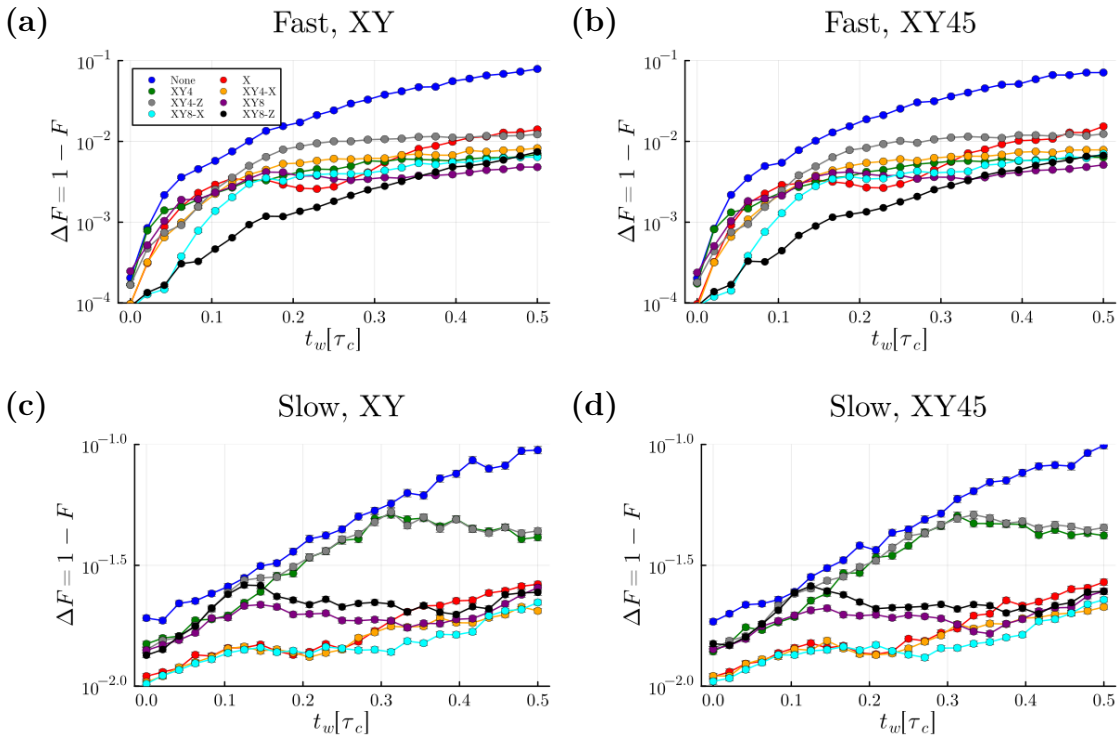

Figure 6.8: Dependence of **average fidelity** F, measured at the end of the forth-back shuttling path, on the **waiting time** t_w in different scenarios. During shuttling, the spin travels at a constant speed $v = L/T$, except when it is stationary for a duration $2t_w$ at $x = L = 100\lambda_c$. The random magnetic field acting on the shuttled spin is strongly along the z-axis, and given by the Hamiltonian in Eq. (6.23). Parameters are listed in Tab. 6.4. Legend in **(a)** applies to all figures. All figures show infidelity $\Delta F = 1 - F$ on a logarithmic y-axis. Notice that y-axis ranges differ. **(a)**, **(b)**: Fast shuttling with shuttling time $T = 0.1\tau_c$. **(c)**, **(d)**: Slow shuttling with shuttling time $T = 1\tau_c$. **(a)**, **(c)**: X, Y pulses in the DD sequences are along the x- and y-axis. **(b)**, **(d)**: X, Y pulses in the DD sequences are along the lines $[1, 1, 0]$ and $[1, -1, 0]$ respectively. Results generated using $N = 320$, $M = 10^3$. Error bars are present in each figure, though may be too small to be visible.

6.4 Summary

In this chapter, we introduce the new dynamical decoupling sequences XY4-X, XY4-Z, XY8-X, and XY8-Z, with the hypothesis that the central pulse will decouple the forward path from the backwards path. We first study these sequences analytically and compare them to the existing XY4 and XY8 sequences. We assess their effectiveness at reducing the decoherence of a spin initialised along the x-axis, and increasing shuttling fidelity averaged over all initial states.

We find that when the state is initialised along the x-axis, the XY8-X sequence is most effective at suppressing decoherence. However, the XY8-Z sequence is most effective at maintaining average fidelity, indicating that the effectiveness of the XY8-X sequence at suppressing decoherence may be specific to the initial state. For slow shuttling, the most effective DD sequences are those that utilise a central X pulse.

We observe that the relationship between waiting time and shuttling time can have a large impact on the effectiveness of a specific DD sequence when considering a DD sequence applied over the entire forth-back shuttling path. There are observable inflection points, where there is a transition from having a pulse during shuttling to having a pulse during the waiting period. These inflection points can lead to optimal waiting times or shuttling times when considering DD sequences.

Finally, we posited that having X-Y pulses rotated 45° relative to the axis along which the independent random processes may affect the effectiveness of the DD sequences. However, no significant difference was observed when looking at average shuttling fidelity.

Chapter 7

Dynamical decoupling for shuttling in Ge

In this chapter, we perform simulations of the effect of a random magnetic field whose direction varies significantly on the decoherence of a qubit during shuttling. For these simulations, we analyse the effectiveness of the DD sequences introduced in Chapter 6. We begin by considering an agnostic model, where the quantising magnetic field is on the same order as the random component of the magnetic field, allowing the direction to change significantly over the course of a shuttling path. We then move on to modelling a specific Ge device by determining a position-dependent deterministic magnetic field extrapolated from the experimentally found position-dependent Larmor frequency.

7.1 Decohering field with strong variation of all components

We begin by considering a Hamiltonian of the same form as in Chapter 6:

$$H(x,t) = B_0 S_z + \tilde{\mathbf{B}}_{\text{eff}}(x,t) \cdot \mathbf{S}, \tag{7.1}$$

where B_0 is a deterministic magnetic field on the order of the variance of $\tilde{\mathbf{B}}_{\text{eff}}$. The random magnetic field $\tilde{\mathbf{B}}_{\text{eff}}$ has the same properties as in Chapter 5: It is a 3-component random process where each random process is derived from an independent OU sheet with same correlation time τ_c and correlation length λ_c, and here we consider that they have the same variance σ_B^2. The main difference between the results in this section and those in Chapter 6 lie in the chosen experimental parameters, listed in Table 7.1. Most significantly, for this section we consider $B_0 = \sigma_B$, meaning that the direction of the magnetic field will vary by around 45%, much higher than the 2% simulated previously.

Furthermore, the shuttling length L is only $1.3\mu m = 4\lambda_c$. The correlation length results from considerations on the size of the wave packet for a hole spin in Ge [55] and the parameters used in the experimental works by the group of Dr. M. Veldhorst [56]. The correlation time τ_c results from experimentally found values of $T_2^H \approx 6\mu s$ and that [57]

$$T_2^H = \left(\frac{12\tau_c}{\sigma^2}\right)^{1/3} \tag{7.2}$$

can be used to estimate the correlation time τ_c.

Table 7.1: Parameters used for Figs. 7.1-7.7, including shuttling length and times, correlation scales, and deterministic & random magnetic field strengths [56].

Parameter	Experimental value	Simulation value	Description
T_2^*	$2.5\mu s$	$0.5\tau_c$	Decoherence time
σ_B	-	$2(\tau_c)^{-1}$	Variance of random field
T_{fast}	$0.2\mu s$	$\frac{1}{30}\tau_c$	"Fast" shuttling time
T_{slow}	$2\mu s$	$\frac{1}{3}\tau_c$	"Slow" shuttling time
L	$1.3\mu m$	$4\lambda_c$	Shuttling length
τ_c	$5.6\mu s$	1	Correlation time
λ_c	$0.3\mu m$	1	Correlation length
B_0	-	σ_B	Quantising magnetic field
t_w	$0.1\mu s$	$\frac{1}{60}\tau_c$	Waiting time

We can again visualise the parameters defining the random sheet by imaging the covariance function, shown in Fig. 7.1. Compared to the covariance function for the parameters in Chapter 6 shown in Fig. 6.2, the width of the lines making up the cross shape is larger as the correlation length λ_c is larger relative to the shuttling length. Furthermore, even for slow shuttling, the total shuttling time is only $2T + 2t_w = 0.7\tau_c$, such that in time, the correlations have only decayed by 50% between the start and endpoint.

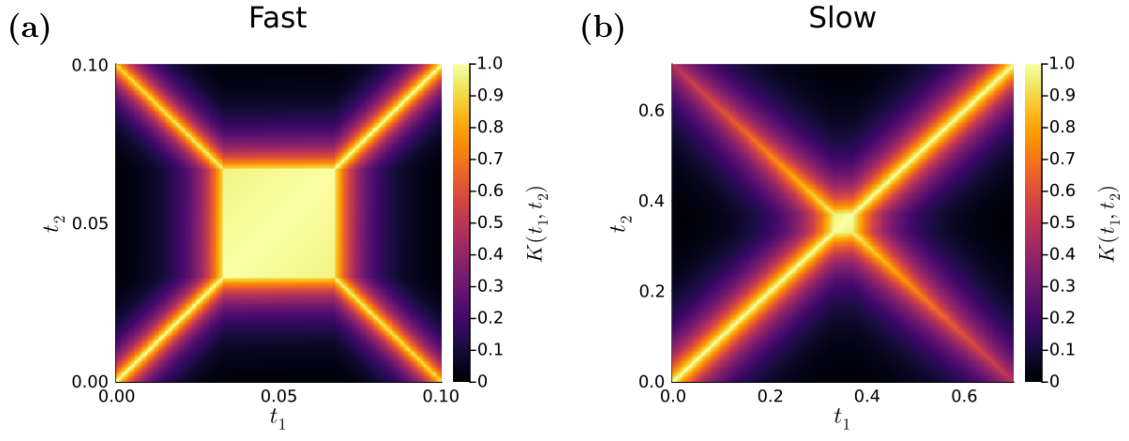

Figure 7.1: Covariance function (Eq. (5.3)) for the random magnetic field along a forth-back path, derived from an OU sheet. Parameters used are $L = 4\lambda_c$, $\sigma_B = 1$, $t_w = (1/30/2)\tau_c$; **(a)**: $T = (1/30)\tau_c$, **(b)**: $T = (1/3)\tau_c$.

7.1.1 Simulation results

We perform similar simulations as in Chapter 6, this time with the Hamiltonian in Eq. (7.1) and the parameters in Tab. 7.1. As decoherence measures, we use the decoherence factor W (Eq. (5.13)) for a spin initialised along the x-axis (which we have termed x-decoherence) and fidelity F (Eq. (5.14)), measured at the end of a forth-back shuttling path, which does not depend on the initial state. The simulation results are displayed in Figs. 7.2-7.7.

In Fig. 7.2(a), we observe that, in general, the X, XY8-X, and XY8-Z sequences are most effective at suppressing loss of coherence for a spin initialised along the x-axis. The XY8-X sequence is the most effective, and the X sequence is more effective than the XY8-Z sequence, except for slow shuttling when $v \lesssim 25(\lambda_c/\tau_c)$. The XY4, XY4-X, XY4-Z and XY8 sequences all show some effectiveness at suppressing x-decoherence. Fig. 7.2(b) shows that when a waiting time $t_w = (1/60)\tau_c$ is included, the results are very similar. In Fig. 7.2(c), we see that using XY-45 pulse axes reduces the effectiveness of the X and XY8-X sequences, which is likely due to the central pulse no longer being parallel to the initial state.

If we instead look at average fidelity in Fig. 7.3, we observe that the XY8-Z sequence shows the highest shuttling fidelity, and most notably, the X sequence shows a reduced effectiveness. This confirms that when we observe that the X sequence is effective at suppressing x-decoherence, this is due to the chosen initial state. For these results, the waiting time has no observable effect.

In Fig. 7.4 we look at x-decoherence for varying shuttling lengths. For fast shuttling with no waiting time (Fig. 7.4(a)), the hierarchy of DD efficiency is the same as in Fig. 7.2, and as expected, increasing the shuttling length (and therefore the shuttling time), leads to more decoherence. Furthermore, looking at average fidelity in Fig. 7.5, we again observe that the XY8-Z sequence outperforms the XY8-X sequence when we average over all initial states.

When including waiting time in Fig. 7.4(b) and 7.5(b), we observe certain inflection points for different sequences, which are a result of pulse occurring during the shuttling component or the stationary (waiting) component of the forth-back shuttle. However, the XY8-X sequence remains most effective at suppressing decoherence of a state initialised along the x-axis, while the XY8-Z sequence is most effective at retaining fidelity when averaged over all initial states.

We observe in Fig. 7.4(c) and (d) that for slow shuttling, the decoherence is much higher, due to the increased evolution time in a random magnetic field. This is also the case for the average fidelity in Fig. 7.5(c) and (d). This indicates that for this slow shuttling velocity, we do not observe an adiabatic process, where the spin follows the changing magnetic field to a degree such that, by the end of the shuttling, it has remained in the same state. Furthermore, for slow shuttling, there is no observable difference due to the waiting time. This is because the time spent shuttling is 20 times longer than the time spent stationary.

Finally, we look at the effect of increasing waiting time on x-decoherence in Fig. 7.6, and average fidelity in Fig. 7.7. These results reinforce previous conclusions. The XY8-X sequence is most effective for suppressing decoherence for a spin initialised along the x-axis, while the XY8-Z sequence is most effective at increasing average fidelity. The relationship between waiting time and shuttling time influences the placement of pulse during a sequence, leading to inflection points and crossover points between different DD sequences. Using 45° rotated X/Y pulses in DD se-

quences does not affect average fidelity, but does reduce the effectiveness of DD sequences with a central X pulse at suppressing x-decoherence, which is due to the spin being initialised along the x-axis. Furthermore, for slow shuttling, the waiting time only has a slight effect in increasing x-decoherence and reducing fidelity.

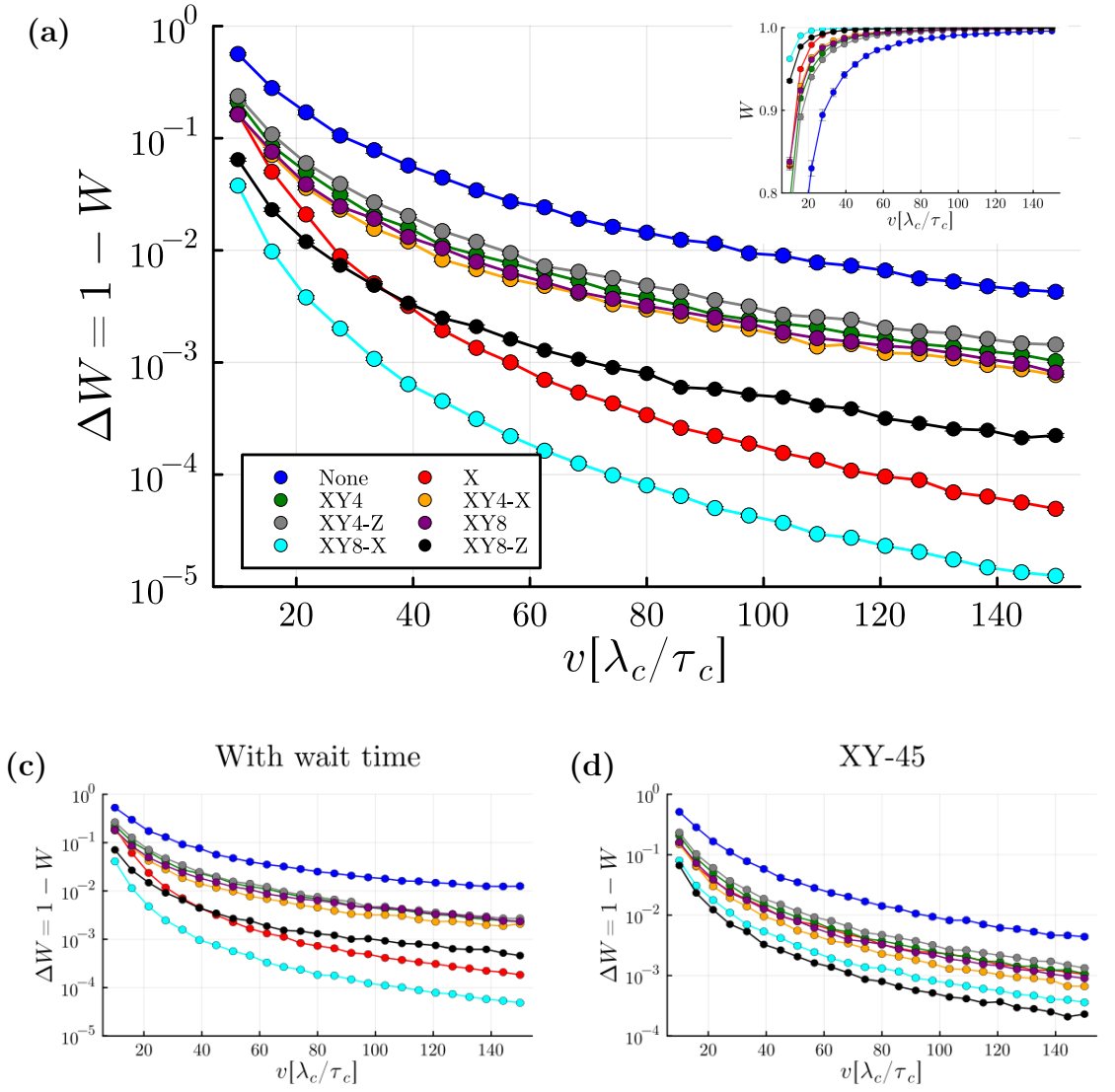

Figure 7.2: Dependence of **decoherence** W of a spin initialised along the x-axis, measured at the end of a forth-back shuttling path, on the **shuttling velocity** $v = L/T$ in different scenarios. During shuttling, the spin travels at a constant speed v, except when it is stationary for a duration $2t_w$ at $x = L = 4\lambda_c$. The random magnetic field acting on the spin is given by the Hamiltonian in Eq. (7.1), and the direction of the magnetic field can vary significantly. Parameters are listed in Tab. 7.1. Legend in **(a)** applies to all figures. We plot $\Delta W = 1 - W$ on a logarithmic y-axis, with the inset in **(a)** showing decoherence W. Notice that y-axis ranges differ. **(a)**: no waiting time ($t_w = 0$). **(b)**: Includes waiting time $t_w = (1/60)\tau_c$. **(c)**: no waiting time ($t_w = 0$), but X and Y pulse axes in DD sequences are rotated 45°. Results generated using $N = 320$, $M = 10^3$. Error bars are present in each figure, though may be too small to be visible.

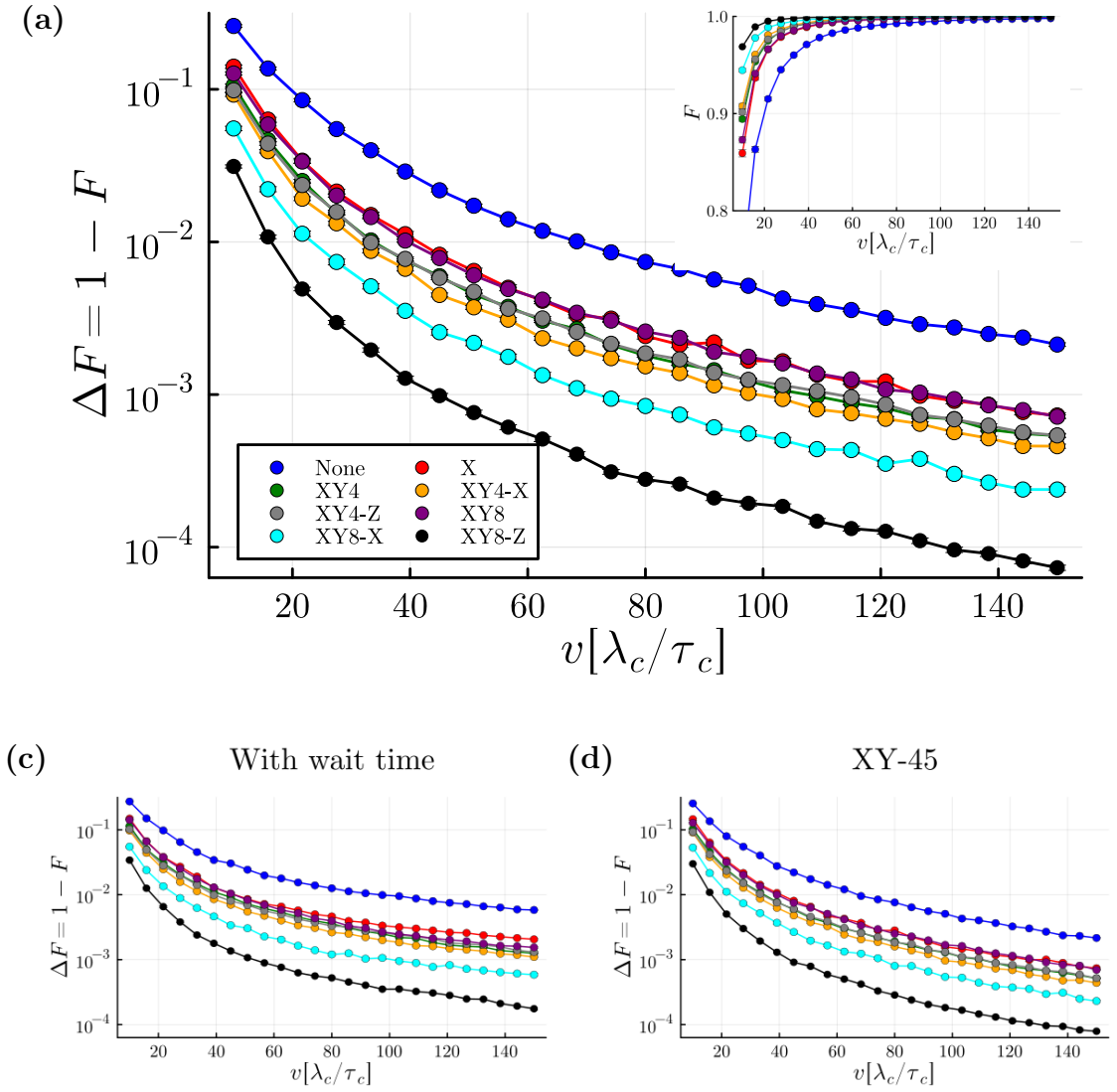

Figure 7.3: Dependence of **average fidelity** F, measured at the end of a forth-back shuttling path, on the **shuttling velocity** $v = L/T$ in different scenarios. During shuttling, the spin travels at a constant speed v, except when it is stationary for a duration $2t_w$ at $x = L = 4\lambda_c$. The random magnetic field acting on the spin is given by the Hamiltonian in Eq. (7.1), and the direction of the magnetic field can vary significantly. Parameters are listed in Tab. 7.1. Legend in **(a)** applies to all figures. We plot infidelity $\Delta F = 1 - F$ on a logarithmic y-axis, with the inset in **(a)** showing fidelity F. **(a)**: no waiting time ($t_w = 0$). **(b)**: Includes waiting time $t_w = (1/60)\tau_c$. **(c)**: no waiting time ($t_w = 0$), but X and Y pulse axes in DD sequences are rotated 45°. Results generated using $N = 320$, $M = 10^3$. Error bars are present in each figure, though may be too small to be visible.

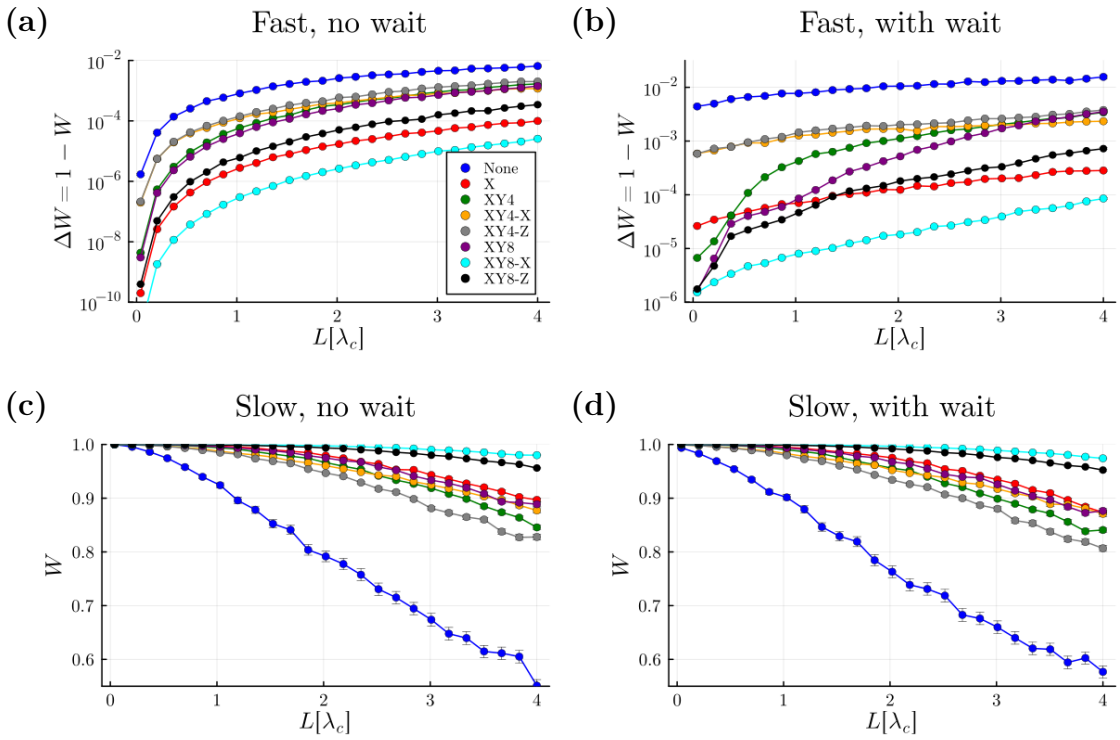

Figure 7.4: Dependence of **decoherence** W of a spin initialised along the x-axis, measured at the end of the forth-back shuttling path, on the **shuttling length** L in different scenarios. During shuttling, the spin travels at a constant speed $v = L/T$, except when it is stationary for a duration $2t_w$ at $x = L$. The random magnetic field acting on the spin is given by the Hamiltonian in Eq. (7.1), and the direction of the magnetic field can vary significantly. Parameters are listed in Tab. 7.1. Legend in **(a)** applies to all figures. **(a)**, (**b**) show $\Delta W = 1 - W$ on a logarithmic y-axis, while **(c)**, **(d)** show decoherence W on a linear scale. Notice that y-axis ranges differ. **(a)**, **(b)**: Fast shuttling with shuttling velocity $v = 120\ \lambda_c/\tau_c$. **(c)**, **(d)**: Slow shuttling with shuttling time shuttling velocity $v = 12\ \lambda_c/\tau_c$. For **(a)**, **(c)**: waiting time $t_w = 0$. For **(b)**, **(d)**: waiting time $t_w = (1/60)\tau_c$. Results generated using $N = 320$, $M = 10^3$. Error bars are present in each figure, though may be too small to be visible.

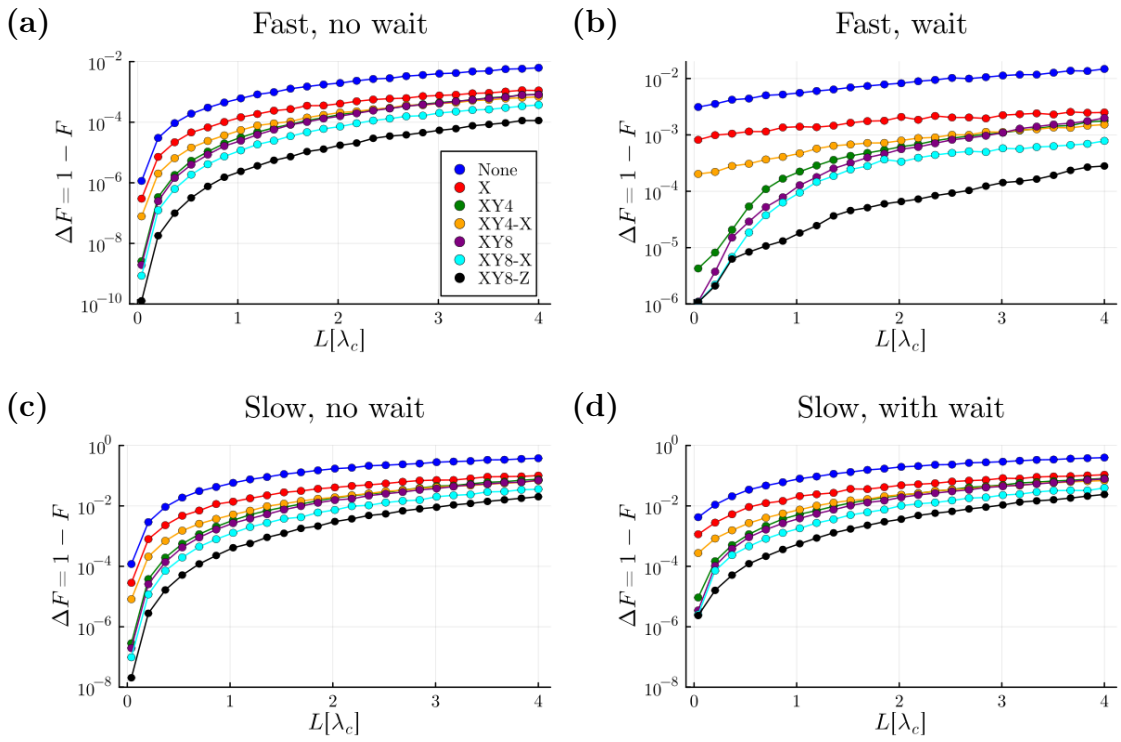

Figure 7.5: Dependence of **average fidelity** F, measured at the end of the forth-back shuttling path, on the **shuttling length** L in different scenarios. During shuttling, the spin travels at a constant speed $v = L/T$, except when it is stationary for a duration $2t_w$ at $x = L$. The random magnetic field acting on the spin is given by the Hamiltonian in Eq. (7.1), and the direction of the magnetic field can vary significantly. Parameters are listed in Tab. 7.1. Legend in **(a)** applies to all figures. All figures show infidelity $\Delta F = 1 - F$ on a logarithmic y-axis. Notice that y-axis ranges differ. **(a)**, (**b**): Fast shuttling with shuttling velocity $v = 120\ \lambda_c/\tau_c$. **(c)**, **(d)**: Slow shuttling with shuttling time shuttling velocity $v = 12\ \lambda_c/\tau_c$. **(a)**, **(c)**: waiting time $t_w = 0$. **(b)**, **(c)**: waiting time $t_w = (1/60)\tau_c$. Results generated using $N = 320$, $M = 10^3$. Error bars are present in each figure, though may be too small to be visible.

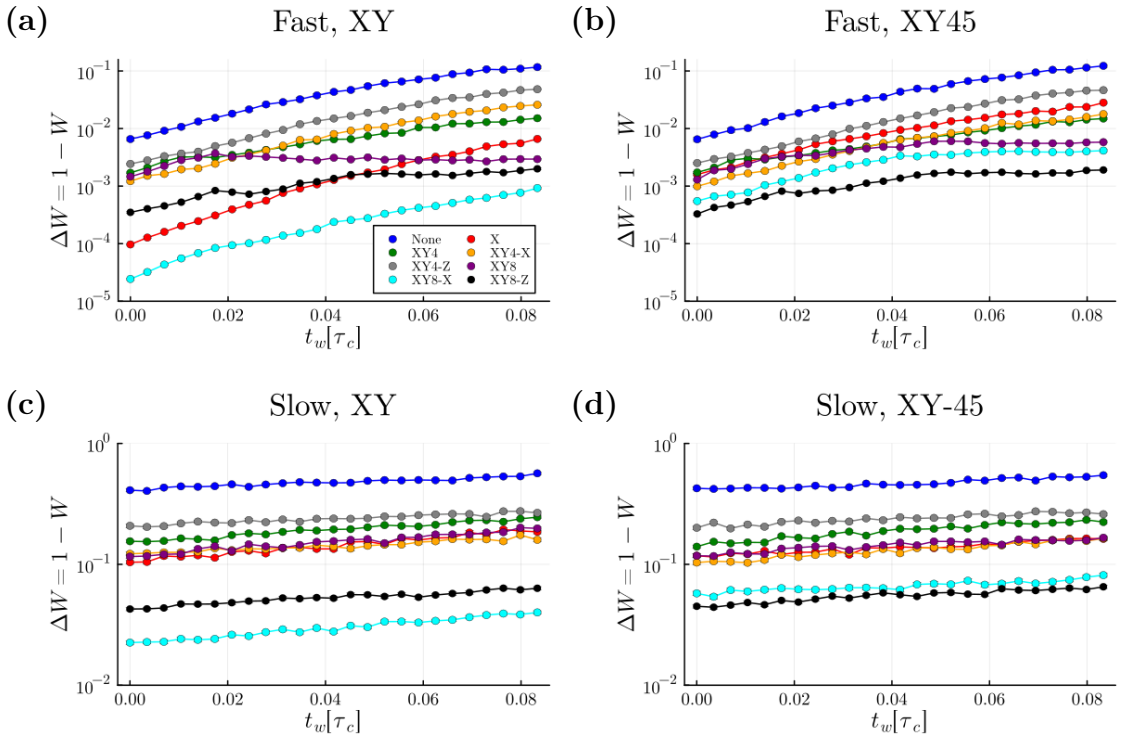

Figure 7.6: Dependence of **decoherence** W of a spin initialised along the x-axis, measured at the end of the forth-back shuttling path, on the **waiting time** t_w in different scenarios. During shuttling, the spin travels at a constant speed $v = L/T$, except when it is stationary for a duration $2t_w$ at $x = L = 4\lambda_c$. The random magnetic field acting on the spin is given by the Hamiltonian in Eq. (7.1), and the direction of the magnetic field can vary significantly. Parameters are listed in Tab. 7.1. Legend in **(a)** applies to all figures. All figures show $\Delta W = 1 - W$ on a logarithmic y-axis. Notice that y-axis ranges differ. **(a)**, **(b)**: Fast shuttling with shuttling time $T = (1/30)\tau_c$. **(c)**, **(d)**: Slow shuttling with shuttling time $T = (1/3)\tau_c$. **(a)**, **(c)**: X, Y pulses in the DD sequences are along the x- and y-axis. **(b)**, **(d)**: X, Y pulses in the DD sequences are along the lines $[1, 1, 0]$ and $[1, -1, 0]$ respectively. Results generated using $N = 320$, $M = 10^3$. Error bars are present in each figure, though may be too small to be visible.

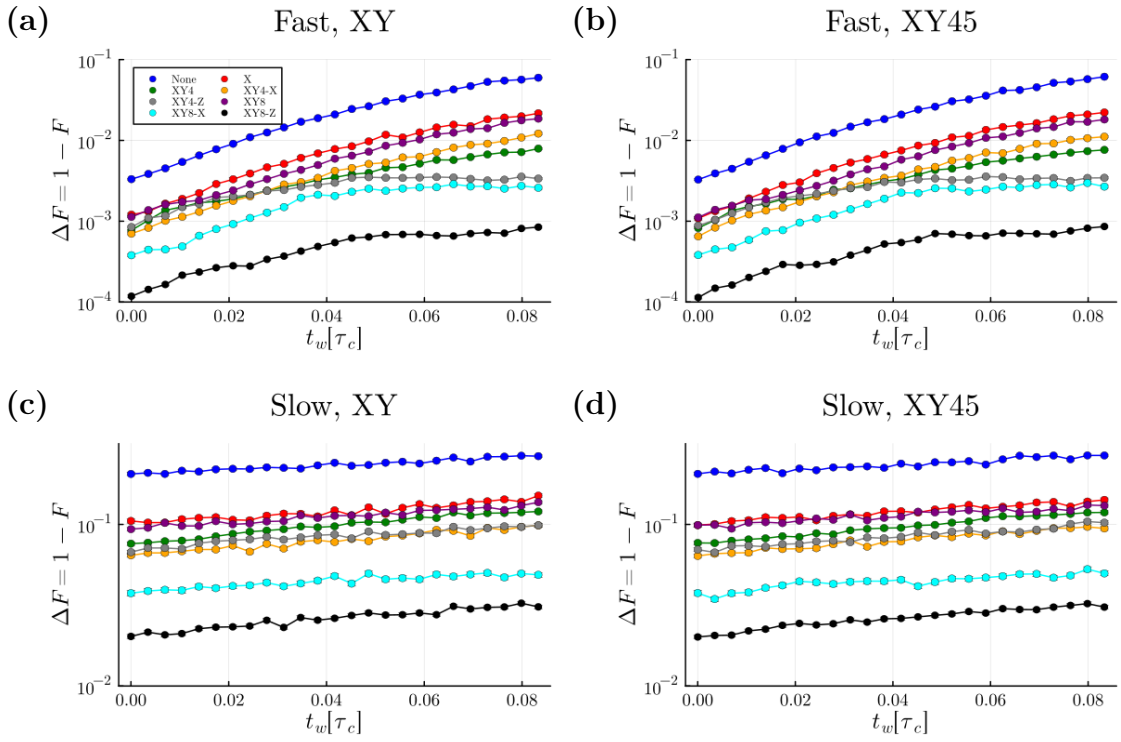

Figure 7.7: Dependence of **average fidelity** F, measured at the end of the forth-back shuttling path, on the **waiting time** t_w in different scenarios. During shuttling, the spin travels at a constant speed $v = L/T$, except when it is stationary for a duration $2t_w$ at $x = L = 4\lambda_c$. The random magnetic field acting on the spin is given by the Hamiltonian in Eq. (7.1), and the direction of the magnetic field can vary significantly. Parameters are listed in Tab. 7.1. Legend in **(a)** applies to all figures. All figures show infidelity $\Delta F = 1 - W$ on a logarithmic y-axis. Notice that y-axis ranges differ. **(a)**, (**b**): Fast shuttling with shuttling time $T = (1/30)\tau_c$. **(c)**, **(d)**: Slow shuttling with shuttling time $T = (1/3)\tau_c$. **(a)**, **(c)**: waiting time $t_w = 0$. **(b)**, **(c)**: waiting time $t_w = (1/60)\tau_c$. Results generated using $N = 320$, $M = 10^3$. Error bars are present in each figure, though may be too small to be visible.

7.2 Modelling a specific Ge device

For the final results of this thesis, we perform exploratory work on modelling a specific Ge device. We make use of the experimentally found Larmor frequency $\omega_L(x)$ of a hole spin in a shuttling channel in Ge, provided by members of the group of Dr. M. Veldhorst [56]. The Larmor frequency $\omega_L(x)$ varies significantly over the course of the shuttling channel, but is stable over long periods of time (months). Therefore, this can be considered a characteristic of the specific device and can give us information on the deterministic magnetic field experienced by the spin during shuttling. With the only available information being $\omega_L(x)$, we can determine $|\mathbf{B}(x)|$, but we cannot determine all three components $B_x(x)$, $B_y(x)$, and $B_z(x)$. We make reasonable assumptions to determine these component below.

First, let us distinguish between *quenched* disorder and *annealed* disorder. The variation in Larmor frequency arises from quenched disorder, which is fixed in time. The resulting effective magnetic field varies along the channel, and differs between channels, making it a form of disorder. However, for repeated experiments with the same channel, this field remains constant, and is therefore a deterministic magnetic field. On top of the *quenched* disorder, we still have the time-dependent *annealed* disorder resulting in a fluctuating effective magnetic field $\tilde{\mathbf{B}}_{\text{eff}}(x,t)$.

To generate the position-dependent deterministic magnetic field, we begin by using the Larmor frequency $\omega_L(x)$ to determine $|\mathbf{B}(x)|$, which can be seen in Fig. 7.8. We make the assumption that when the Larmor frequency is large, the magnetic field is predominantly along the z-axis, while when the Larmor frequency is small, the magnetic field is predominantly in the x-y plane. We use this to determine the out-of-plane magnetic field $B_z(x)$ and the in-plane magnetic field $B_p(x)$. Finally, we model $B_x(x)$ and $B_y(x)$ as OU processes, renormalised at each x such that $(B_p(x))^2 = (B_x(x))^2 + (B_y(x))^2$. We generate two profiles, shown in Fig. 7.8. Both profiles have the same $B_z(x)$ and $|\mathbf{B}(x)|$, but their $B_x(x)$ and $B_y(x)$ differ. By simulating shuttling in both profiles, we can determine if conclusions are particular to a specific realisation of $B_x(x)$ and $B_y(x)$.

To be explicit, for these results we model the Hamiltonian

$$H(x,t) = \mathbf{B}_0(x) \cdot \mathbf{S} + \tilde{\mathbf{B}}_{\text{eff}}(x,t) \cdot \mathbf{S}, \tag{7.3}$$

where $\mathbf{B}_0(x)$ is given by the profile in either Fig. 7.8(a) or Fig. 7.8(b). The random magnetic field $\tilde{\mathbf{B}}_{\text{eff}}(x,t)$ is modelled the same way as in the previous sections: A random magnetic field along a forth-back path, derived from an OU sheet. The experimental parameters used are listed in Tab. 7.1. Throughout, we define the coordinate axes in the lab frame such that magnetic fields B_x, B_y, and B_z, in the profiles Fig. 7.8 are along the x-, y-, and z-axis respectively. This frame also determines along which axes we apply decoupling pulses, and the initial state along the x-axis. This means the initial x-state is not necessarily the x-state belonging to the quantisation axis determined by the deterministic magnetic field at the start of the shuttling channel at position $x = 0$.

We again consider decoherence W for a spin initialised along the x-axis (x-decoherence), and average fidelity F. For the average fidelity, we do not account for the deterministic evolution due to $\mathbf{B}_0(x)$.

The simulation results for x-decoherence are shown in Figs. 7.9-7.14. In Fig. 7.9 we compare profiles 1 and 2 for increasing shuttling velocities. We observe

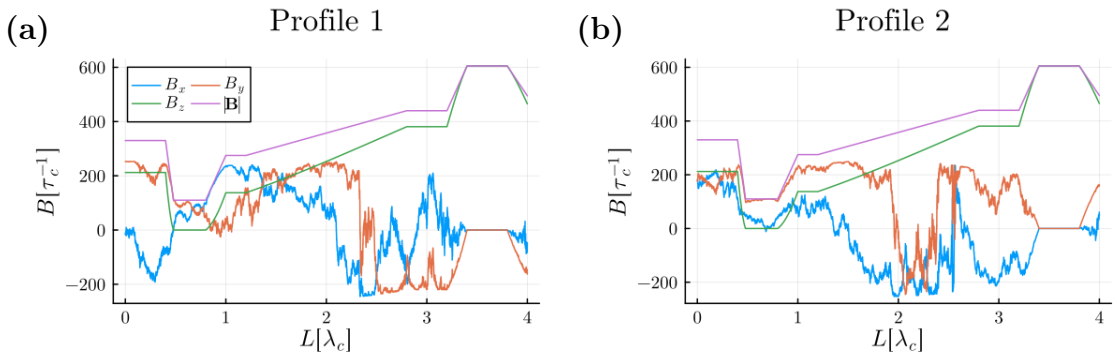

Figure 7.8: Position-dependent deterministic magnetic fields for a specific Ge device, based on the experimentally measured Larmor frequencies. $B_z(x)$ is constructed such that when the Larmor frequency is large (i.e.$|\mathbf{B(x)}|$ is large), $B_z(x)$ is large such that the deterministic magnetic field is strongly along the z-axis. $B_x(x)$ and $B_y(x)$ are scaled OU process such that for all x, $|\mathbf{B}(x)|^2 = B_x(x)^2 + B_y(x)^2 + B_z(x)^2$. **(a)** and **(b)** contain two different realisations of $B_x(x)$, $B_y(x)$, but the same $B_z(x)$. We refer to **(a)** as "Profile 1" and **(b)** as "Profile 2".

that the simulations without decoupling show quite erratic behaviour, which can be significantly different for the two profiles. The effectiveness of decoupling sequences can also vary significantly depending on the velocity and the profile. In general, the XY8-X and XY8-Z sequence show good performance. When waiting time is included, all decoupling sequences showing a noticeable effectiveness at suppressing loss of decoherence for both both profiles. If instead we look at the slow shuttling regime in Fig. 7.10, we observe that generally, the x-decoherence is much higher than during fast shuttling. Here too, the effectiveness of DD sequences is very scenario dependent, though the XY8-X sequence often is effective.

In Fig. 7.11 we look at the dependence of x-decoherence on the shuttling length L, for fast shuttling speed $v = 120\ \lambda_c/\tau_c$. For these simulations, L also determines the point in the deterministic magnetic field profile where the shuttled spin stops and begins its backwards trajectory. This may have a large impact on the result characteristics, depending on the deterministic magnetic field during the waiting period, and may even be useable to find optimised waiting points. We repeat the underlying deterministic magnetic fields as insets in Fig. 7.11(c) and (d). We observe that especially when waiting time is included, all sequences are effective in suppressing decoherence. When waiting time is not included, they are also somewhat effective, though this can vary based on the shuttling length. We do again observe that the XY8-X and XY8-Z sequences show the highest overall effectiveness. Looking at slow shuttling in Fig. 7.12 shows highly varying characteristics, although we do observe that the decoupling sequences are often effective.

In Fig. 7.13 we vary the waiting time t_w, for fast shuttling such that $v = 120\ \lambda_c/\tau_c$. We observe that the waiting time can have a significant impact on the x-decoherence when no DD sequences are used. In general it is the XY8, XY8-X and XY8-Z protocols that are most effective. The same observations are made for slow shuttling ($v = 12\ \lambda_c/\tau_c$) in Fig. 7.14.

Overall, we have observed that making general conclusions for these scenarios is difficult. This is due to some results being dependent on the profile analysed,

as well as a significant variation depending on the independent variables. We do observe that the XY8-X and XY8-Z are often most effective, and that often using any DD sequence suppresses decoherence significantly, as opposed to not using any DD sequence.

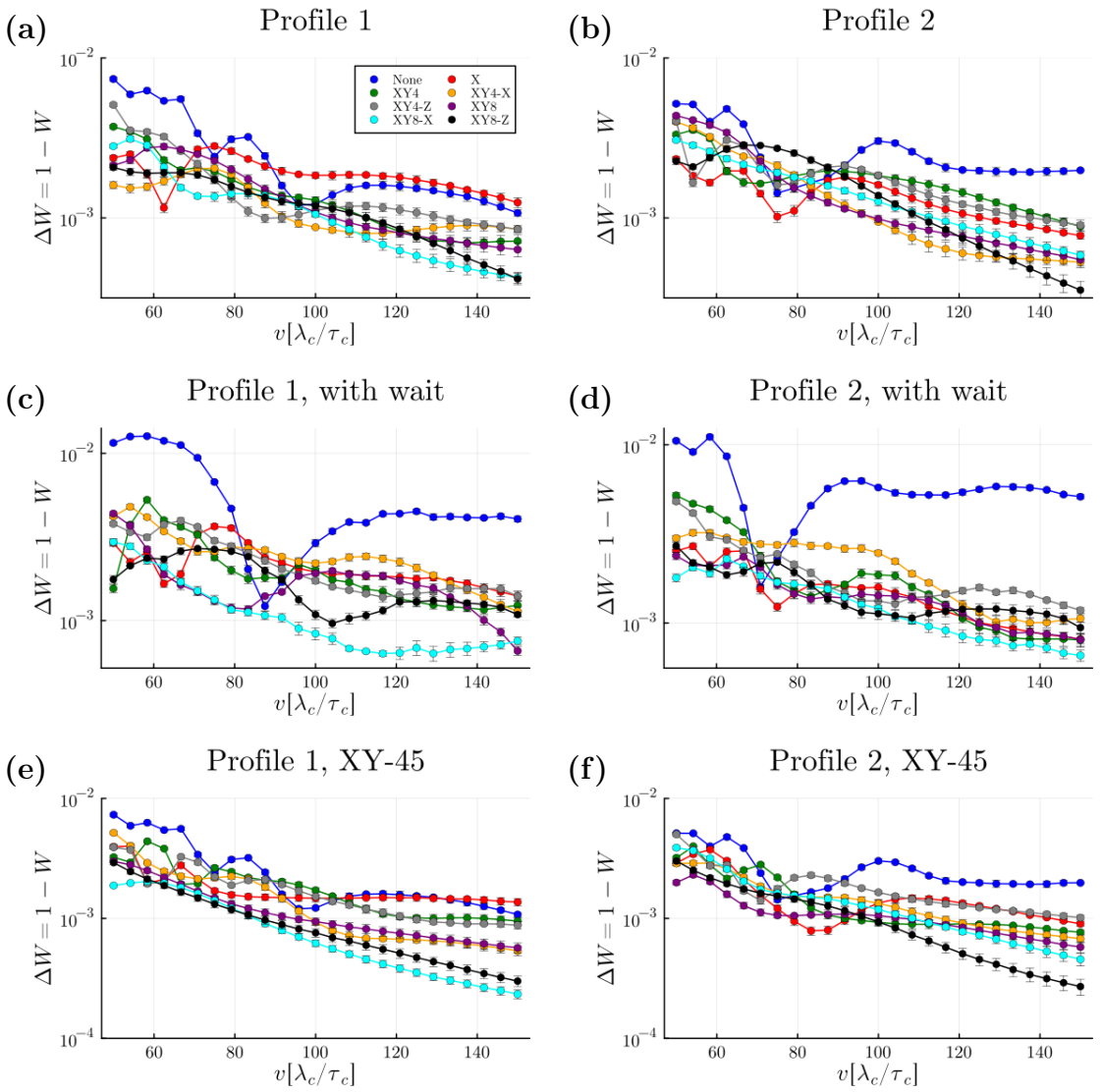

Figure 7.9: Dependence of decoherence W of a spin initialised along the x-axis, measured at the end of a forth-back shuttling path, on the **shuttling velocity** $v = L/T$ in different scenarios. These figures focus on **fast shuttling velocities**. During shuttling, the spin travels at a constant speed v, except when it is stationary for a duration $2t_w$ at $x = L = 4\lambda_c$. The random magnetic field acting on the spin is given by the Hamiltonian in Eq. (7.3), with $\mathbf{B}_0(x)$ a profile-specific position-dependent deterministic magnetic field on the profile. Profile 1 and profile 2 are presented in Fig. 7.8. **(a)**, **(c)**, **(e)** use Profile 1. **(b)**, **(d)**, **(f)** use Profile 2. Parameters are listed in Tab. 7.1. Legend in **(a)** applies to all figures. In each figure we plot $\Delta W = 1 - W$ on a logarithmic y-axis. Notice that y-axis ranges differ. **(a)**, **(b)**: no waiting time ($t_w = 0$). **(c)**, **(d)**: Includes waiting time $t_w = (1/60)\tau_c$. **(e)**, **(f)**: no waiting time ($t_w = 0$), but X and Y pulse axes in DD sequences are rotated 45°. Results generated using $N = 320$, $M = 10^5$. Error bars are present in each figure, though may be too small to be visible.

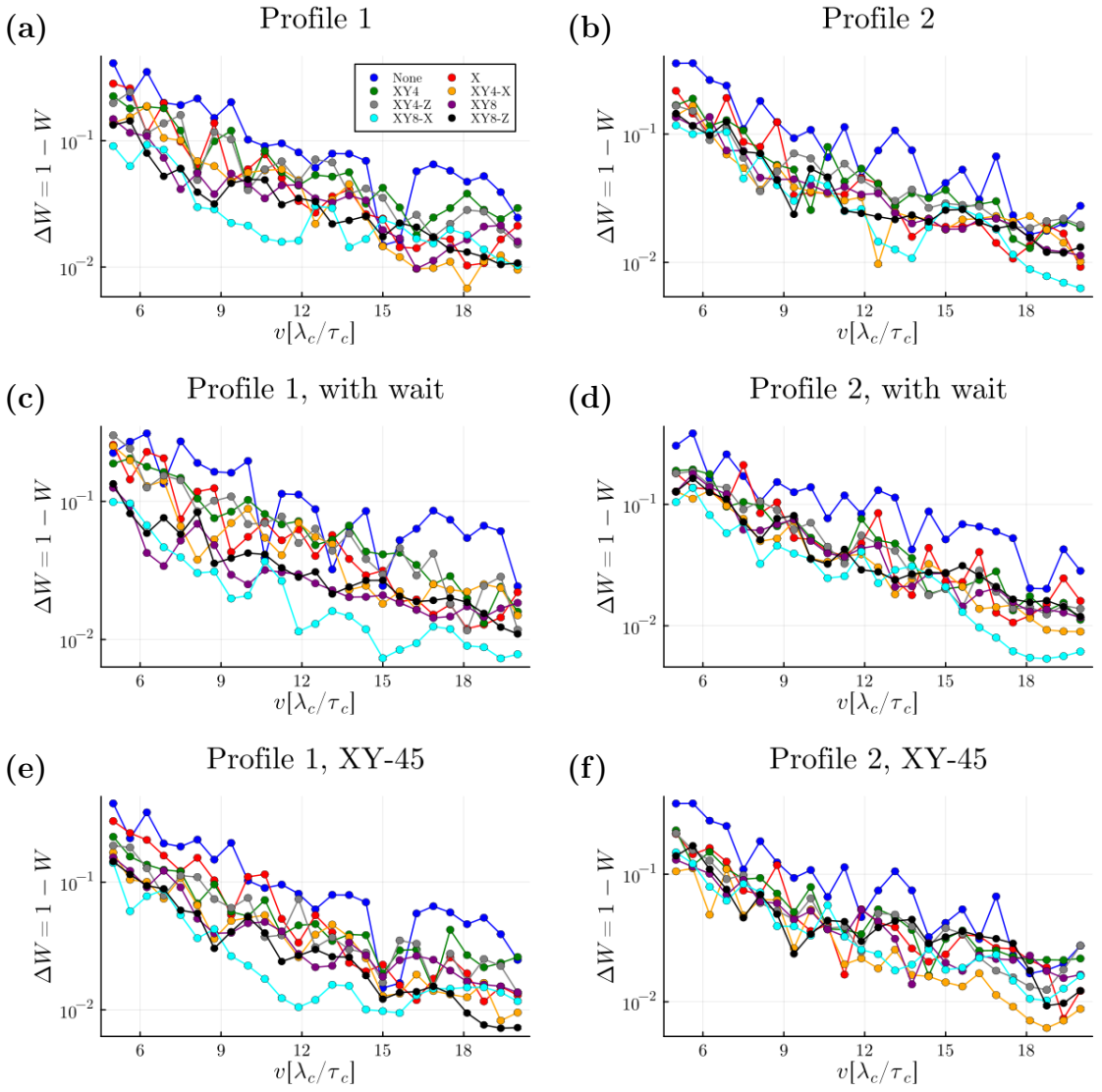

Figure 7.10: Dependence of decoherence W of a spin initialised along the x-axis, measured at the end of a forth-back shuttling path, on the **shuttling velocity** $v = L/T$ in different scenarios. These figures focus on **slow shuttling velocities**. During shuttling, the spin travels at a constant speed v, except when it is stationary for a duration $2t_w$ at $x = L = 4\lambda_c$. The random magnetic field acting on the spin is given by the Hamiltonian in Eq. (7.3), with $\mathbf{B}_0(x)$ a profile-specific position-dependent deterministic magnetic field on the profile. Profile 1 and profile 2 are presented in Fig. 7.8. **(a)**, **(c)**, **(e)** use Profile 1. **(b)**, **(d)**, **(f)** use Profile 2. Parameters are listed in Tab. 7.1. Legend in **(a)** applies to all figures. In each figure we plot $\Delta W = 1 - W$ on a logarithmic y-axis. **(a)**, **(b)**: no waiting time ($t_w = 0$). **(c)**, **(d)**: Includes waiting time $t_w = (1/60)\tau_c$. **(e)**, **(f)**: no waiting time ($t_w = 0$), but X and Y pulse axes in DD sequences are rotated 45°. Results generated using $N = 320$, $M = 10^5$. Error bars are present in each figure, though may be too small to be visible.

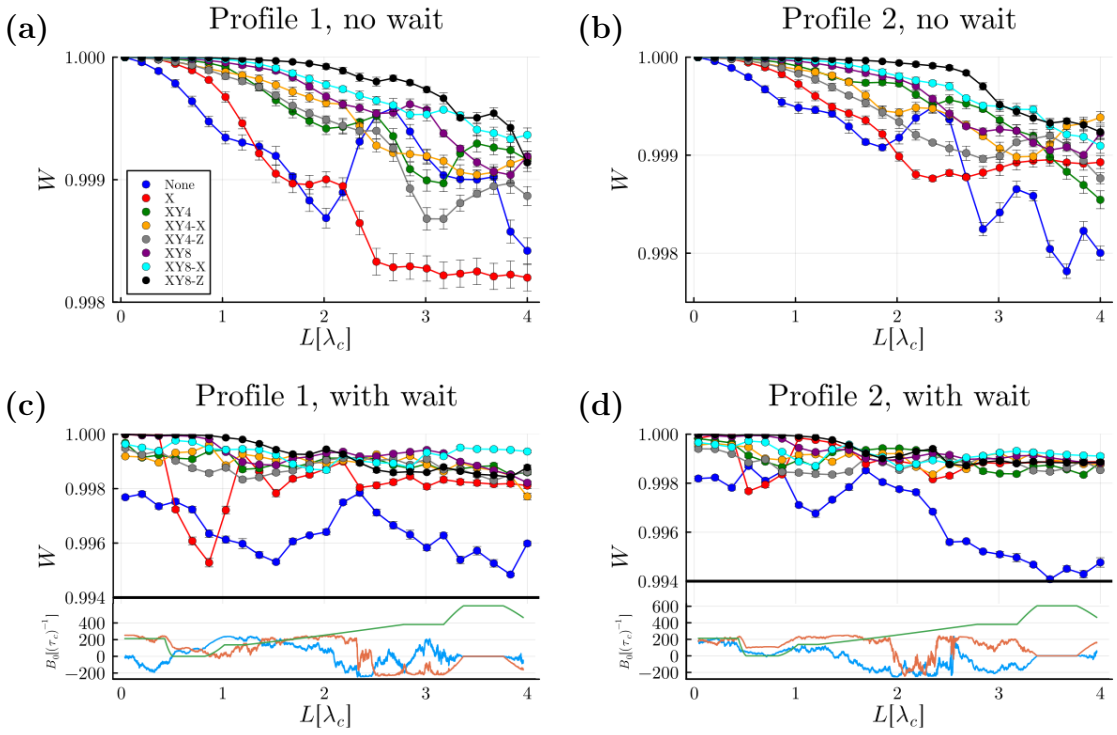

Figure 7.11: Dependence of decoherence W of a spin initialised along the x-axis, measured at the end of a forth-back shuttling path, on the **shuttling length** L in different scenarios. During shuttling, the spin travels at a constant speed $v = L/T$, except when it is stationary for a duration $2t_w$ at $x = L$. These figures involve **fast shuttling** with $v = 120\lambda_c/\tau_c$. The random magnetic field acting on the spin is given by the Hamiltonian in Eq. (7.3), with $\mathbf{B}_0(x)$ a profile-specific position-dependent deterministic magnetic field on the profile. **(a)**, **(c)** use Profile 1, with **(c)** containing an inset of the profile. **(b)**, **(d)**, use Profile 2, with **(d)** containing an inset of the profile. Parameters are listed in Tab. 7.1. Legend in **(a)** applies to all figures. Notice that y-axis ranges differ. **(a)**, **(b)**: no waiting time ($t_w = 0$). **(c)**, **(d)**: Includes waiting time $t_w = (1/60)\tau_c$. Results generated using $N = 320$, $M = 10^5$. Error bars are present in each figure, though may be too small to be visible.

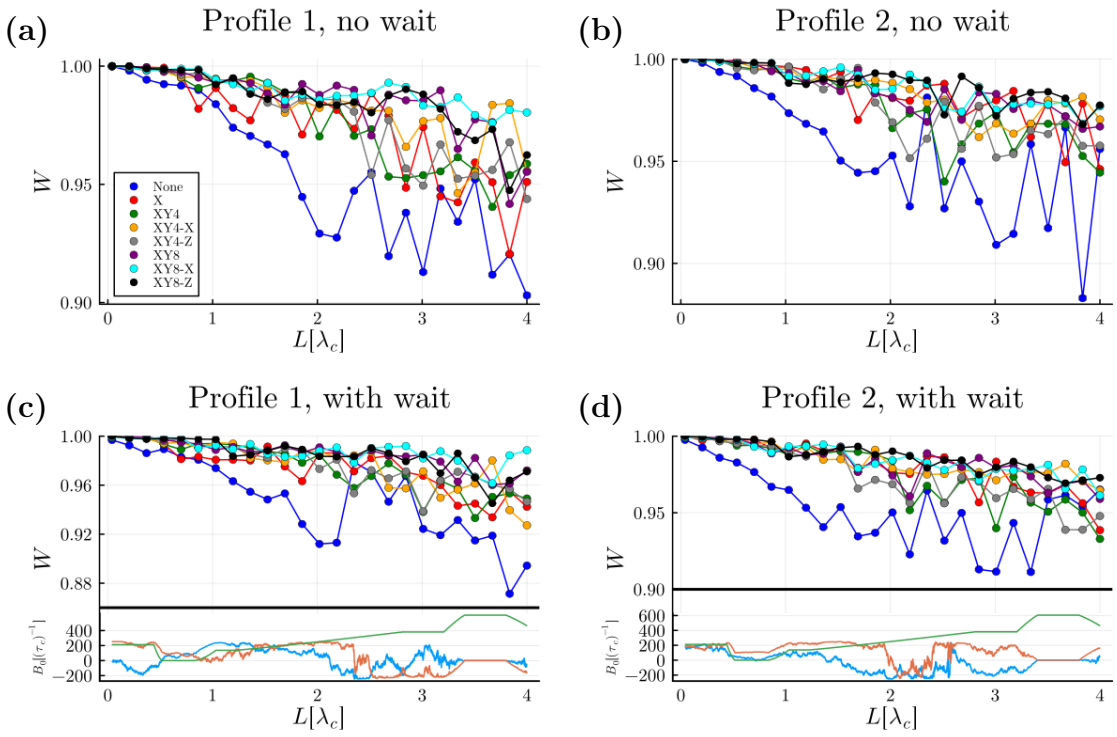

Figure 7.12: Dependence of decoherence W of a spin initialised along the x-axis, measured at the end of a forth-back shuttling path, on the **shuttling length** L in different scenarios. During shuttling, the spin travels at a constant speed $v = L/T$, except when it is stationary for a duration $2t_w$ at $x = L$. These figures involve **slow shuttling** with $v = 12\lambda_c/\tau_c$. The random magnetic field acting on the spin is given by the Hamiltonian in Eq. (7.3), with $\mathbf{B}_0(x)$ a profile-specific position-dependent deterministic magnetic field on the profile. **(a)**, **(c)** use Profile 1, with **(c)** containing an inset of the profile. **(b)**, **(d)**, use Profile 2, with **(d)** containing an inset of the profile. Parameters are listed in Tab. 7.1. Legend in **(a)** applies to all figures. Notice that y-axis ranges differ. **(a)**, **(b)**: no waiting time ($t_w = 0$). **(c)**, **(d)**: Includes waiting time $t_w = (1/60)\tau_c$. Results generated using $N = 320$, $M = 10^5$. Error bars are present in each figure, though may be too small to be visible.

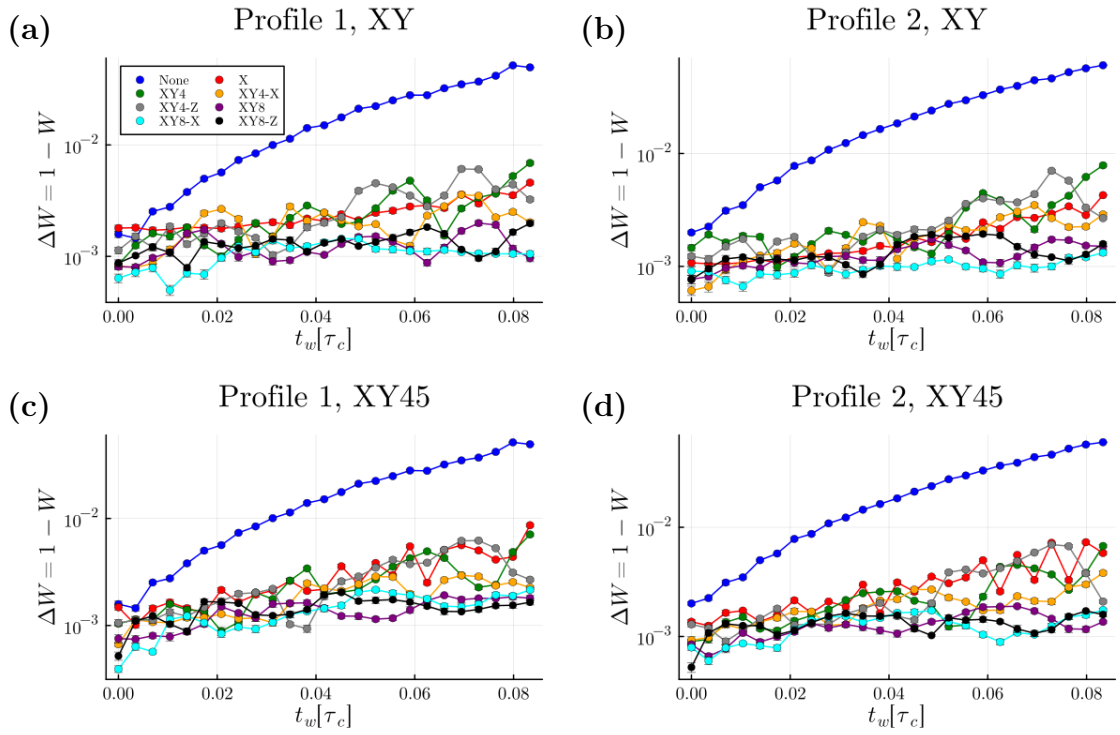

Figure 7.13: Dependence of decoherence W of a spin initialised along the x-axis, measured at the end of a forth-back shuttling path, on the **waiting time** t_w in different scenarios. During shuttling, the spin travels at a constant speed $v = L/T$, except when it is stationary for a duration $2t_w$ at $x = L = 4\lambda_c$. These figures involve **fast shuttling** with $v = 120\lambda_c/\tau_c$. The random magnetic field acting on the spin is given by the Hamiltonian in Eq. (7.3), with $\mathbf{B}_0(x)$ a profile-specific position-dependent deterministic magnetic field on the profile. Profile 1 and profile 2 are presented in Fig. 7.8. **(a)**, **(c)** use Profile 1 **(b)**, **(d)**, use Profile 2. Parameters are listed in Tab. 7.1. Legend in **(a)** applies to all figures. In each figure we plot $\Delta W = 1 - W$ on a logarithmic y-axis. **(a)**, **(b)**: X, Y pulses in the DD sequences are along the x- and y-axis. **(c)**, **(d)**: X, Y pulses in the DD sequences are along the lines $[1, 1, 0]$ and $[1, -1, 0]$ respectively. Results generated using $N = 320$, $M = 10^5$. Error bars are present in each figure, though may be too small to be visible.

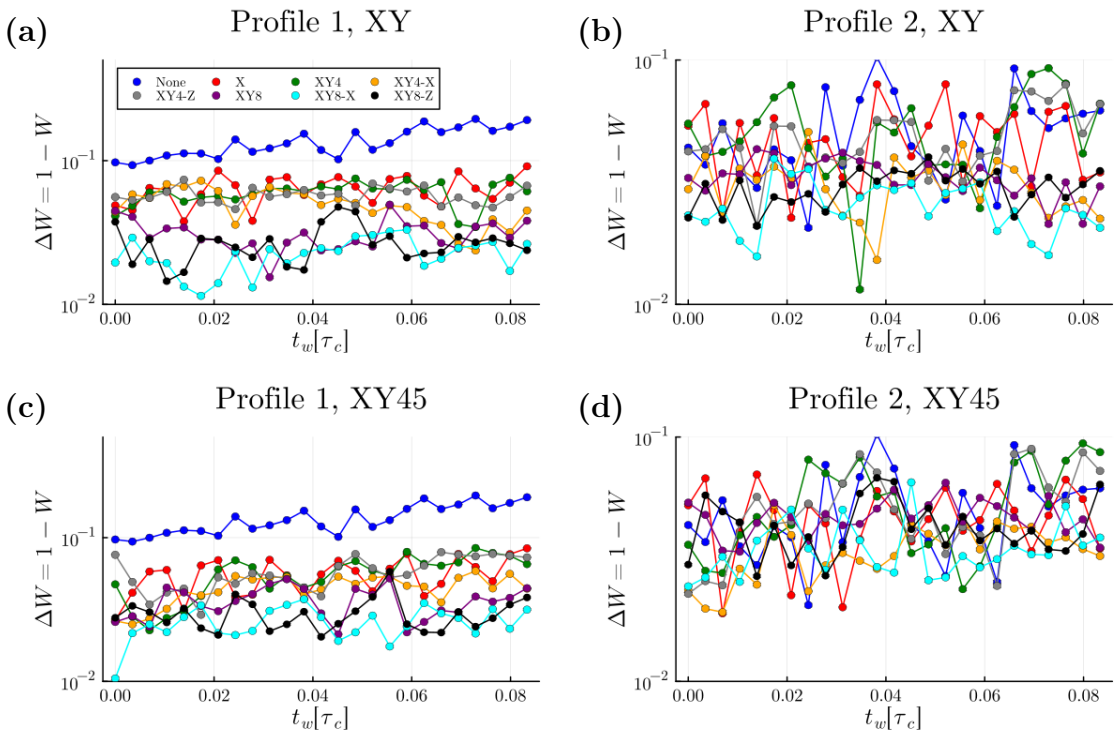

Figure 7.14: Dependence of decoherence W of a spin initialised along the x-axis, measured at the end of a forth-back shuttling path, on the **waiting time** t_w in different scenarios.During shuttling, the spin travels at a constant speed $v = L/T$, except when it is stationary for a duration $2t_w$ at $x = L = 4\lambda_c$. These figures involve **slow shuttling** with $v = 12\lambda_c/\tau_c$. The random magnetic field acting on the spin is given by the Hamiltonian in Eq. (7.3), with $\mathbf{B}_0(x)$ a profile-specific position-dependent deterministic magnetic field on the profile. Profile 1 and profile 2 are presented in Fig. 7.8. **(a)**, **(c)** use Profile 1 **(b)**, **(d)**, use Profile 2. Parameters are listed in Tab. 7.1. Legend in **(a)** applies to all figures. In each figure we plot $\Delta W = 1 - W$ on a logarithmic y-axis. Notice that y-axis ranges differ. **(a)**, **(b)**: X, Y pulses in the DD sequences are along the x- and y-axis. **(c)**, **(d)**: X, Y pulses in the DD sequences are along the lines $[1, 1, 0]$ and $[1, -1, 0]$ respectively. Results generated using $N = 320$, $M = 10^5$. Error bars are present in each figure, though may be too small to be visible.

7.2.1 Shuttling fidelity

We can instead look at shuttling fidelity, however taking into account the deterministic component of the magnetic field is a challenge as it does not commute with the random component. For simulations in Figs. 7.15 and Figs. 7.16, we do not account for the deterministic component. This leads to average fidelities that are highly varying dependent on the parameters. We observe in Fig. 7.16 that only at velocities four times as large as what we previously considered "fast" shuttling, do we achieve average fidelities nearing 1. If this does occur, it is not always clear which DD sequence is optimal.

In Fig. 7.16 we look at slow shuttling ($v = 12\ \lambda_c/\tau_c$) for different waiting times. The results frequently show oscillations depending on the waiting time. This is because at the waiting point, the spin experiences a deterministic rotation whose angle depends on the waiting time, hence the periodicity in waiting time. However, knowing when these peaks occur for different sequences may be important when optimising shuttling parameters. Additional results on average fidelity for different scenarios are included in Appendix B.1.

To make use of the average fidelity measure would require a method for accounting for the deterministic rotation. We could do this by finding the evolution operator corresponding to only the deterministic magnetic field, and performing it as an inverse rotation to the final evolution operator. However, it is important to note that as the deterministic and random component of the magnetic field do not commute, this inverse rotation would not perfectly negate the influence of the deterministic magnetic field (as it would if both the deterministic and random components of the magnetic field are along the z-axis). Nevertheless, we conjecture that this would be a suitable way of analysing the average fidelity.

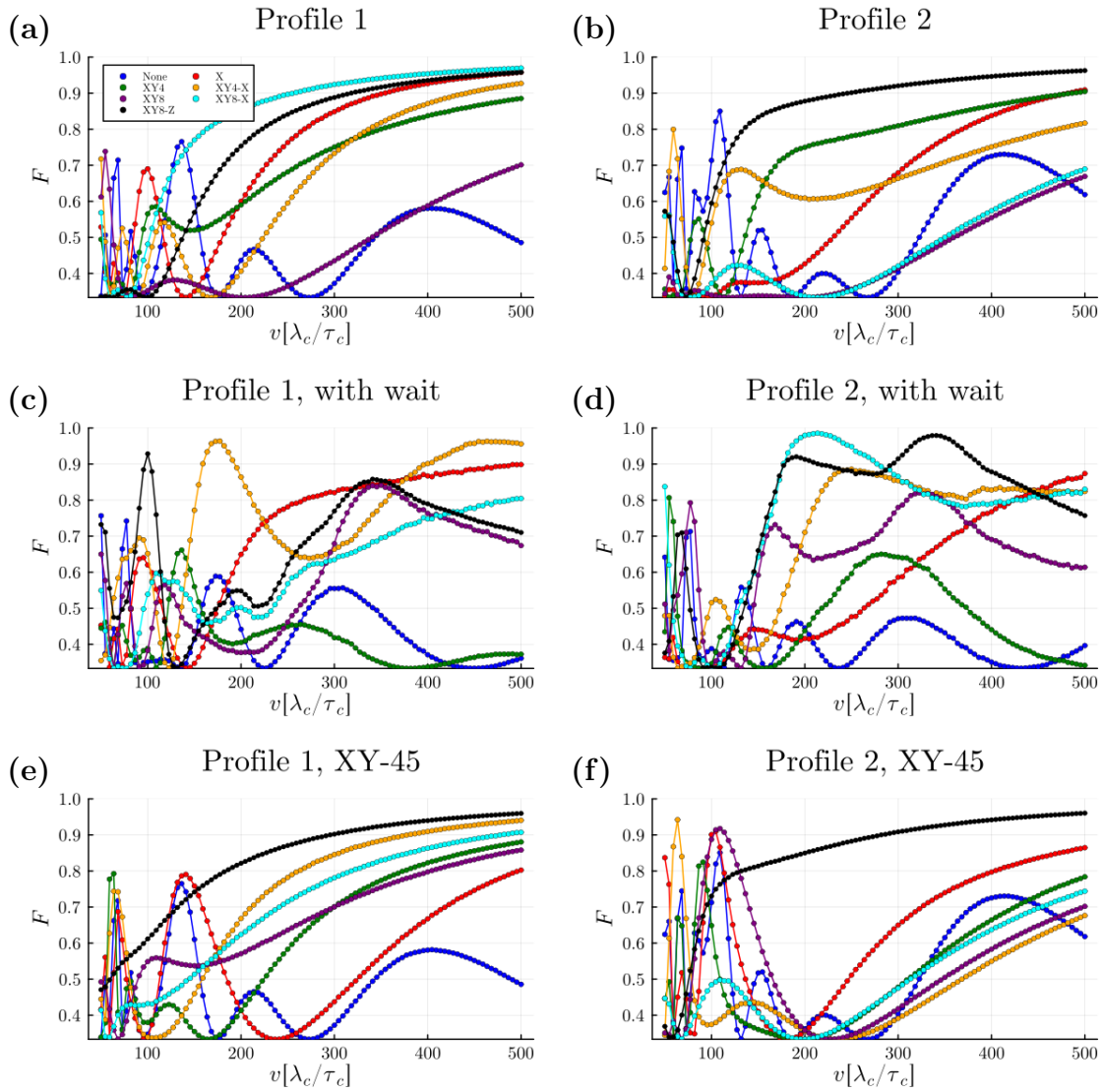

Figure 7.15: Dependence of average fidelity F, measured at the end of a forth-back shuttling path, on the **shuttling velocity** $v = L/T$ in different scenarios. These figures focus on **very fast shuttling velocities**. During shuttling, the spin travels at a constant speed v, except when it is stationary for a duration $2t_w$ at $x = L = 4\lambda_c$. The random magnetic field acting on the spin is given by the Hamiltonian in Eq. (7.3), with $\mathbf{B}_0(x)$ a profile-specific position-dependent deterministic magnetic field on the profile. Profile 1 and profile 2 are presented in Fig. 7.8. **(a)**, **(c)**, **(e)** use Profile 1. **(b)**, **(d)**, **(f)** use Profile 2. Parameters are listed in Tab. 7.1. Legend in **(a)** applies to all figures. **(a)**, **(b)**: no waiting time ($t_w = 0$). **(c)**, **(d)**: Includes waiting time $t_w = (1/60)\tau_c$. **(e)**, **(f)**: no waiting time ($t_w = 0$), but X and Y pulse axes in DD sequences are rotated 45°. Results generated using $N = 1600$, $M = 10^2$. Error bars are present in each figure, but are too small to be visible.

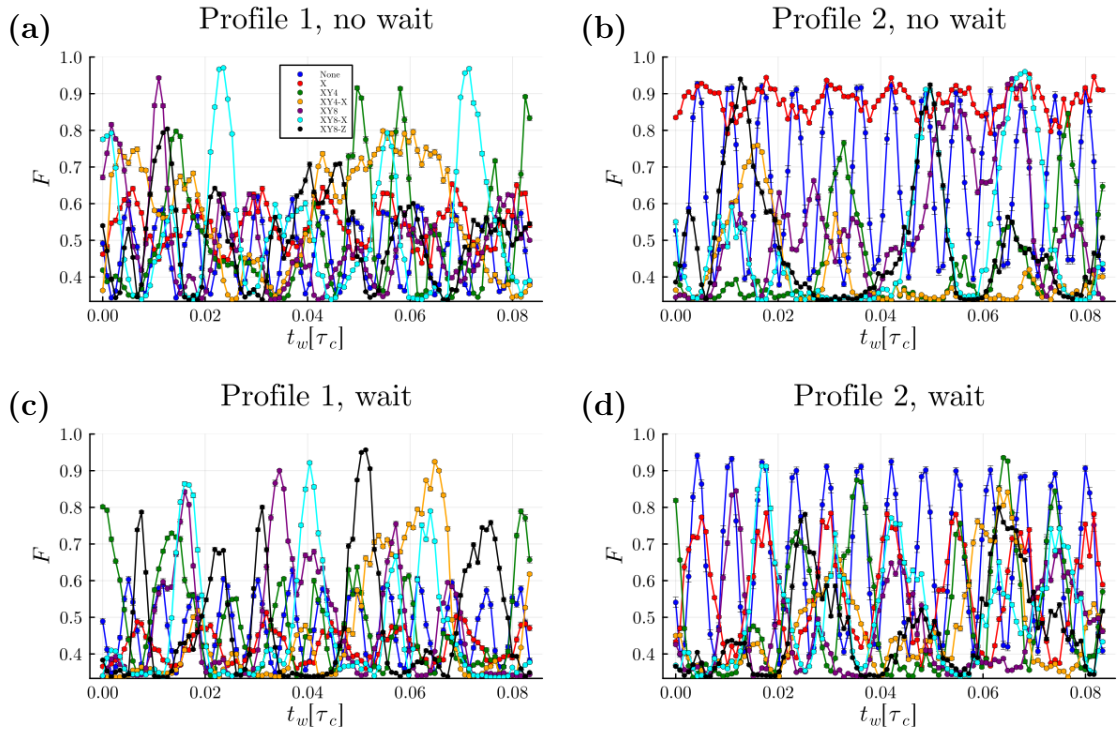

Figure 7.16: Dependence of average fidelity F, measured at the end of a forth-back shuttling path, on the **waiting time** t_w in different scenarios. During shuttling, the spin travels at a constant speed $v = L/T$, with $L = 4\lambda_c$ the shuttling length and T the shuttling time, except when it is stationary for a duration $2t_w$ at $x = L$. These figures involve **slow shuttling** with $v = 12\lambda_c/\tau_c$. The random magnetic field acting on the spin is given by the Hamiltonian in Eq. (7.3), with $\mathbf{B}_0(x)$ a profile-specific position-dependent deterministic magnetic field on the profile. Profile 1 and profile 2 are presented in Fig. 7.8. **(a)**, **(c)** use Profile 1 **(b)**, **(d)**, use Profile 2. Parameters are listed in Tab. 7.1. Legend in **(a)** applies to all figures. **(a)**, **(b)**: X, Y pulses in the DD sequences are along the x- and y-axis. **(c)**, **(d)**: X, Y pulses in the DD sequences are along the lines $[1, 1, 0]$ and $[1, -1, 0]$ respectively. Results generated using $N = 1600$, $M = 10^2$. Error bars are present in each figure, but are too small to be visible.

Chapter 8

Conclusion

In this thesis, we investigate the effect of 3D random magnetic fields on decoherence and fidelity loss during the shuttling of a spin. This is particularly relevant for Ge devices, where the direction of the magnetic field varies significantly. We implement a method to simulate random magnetic fields and calculate their average effect. We benchmark the method in different scenarios, and demonstrate that the accuracy of the method scales as well (or better) than the expected scaling in both the Monte Carlo number M, and the discretisation number N. We further verify the method by applying it to situations such as evolution in a quasi-static random magnetic field. This method enables the simulation of various systems where the magnetic field is both 3-dimensional and can be modelled as a random process.

Novel dynamical decoupling sequences designed for shuttling are introduced, namely the XY4-X, XY4-Z, XY8-X and XY8-Z sequences. These are modifications of the well-used XY4 and XY8 protocols where a central pulse is included to reduce the effect of resurfacing correlations during forth-back shuttling. These sequences are studied analytically using Average Hamiltonian Theory. The XY8-Z sequence in particular is expected to be effective at suppressing decoherence, with first-, second-, and third-order effective Hamiltonians of zero, as well as an anticorrelated effective Hamiltonian at two same points in space, during forth-back shuttling.

Using the developed method, we compare the effectiveness of the discussed DD sequences at suppressing decoherence of a spin initialised along the x-axis when it is shuttled through a random magnetic field with a strong constant quantising magnetic field. The direction of the magnetic field only varies around $2°$, and the underlying random sheet has a very short correlation length, such that during unidirectional shuttling we approach the motional narrowing regime. We find that the XY8-X sequence is most effective at suppressing decoherence for a shuttled spin initialised along the x-axis. When we investigate fidelity averaged over all possible initial states instead, we find that the XY8-Z sequence is most effective at increasing shuttling fidelity. Both sequences generally outperform the traditional XY8 sequence, leading us to conclude that the central pulse is critical when considering DD during shuttling. We find an intrinsic relationship between shuttling time and waiting time in determining the exact timing of pulse during a sequence. This can impact the effectiveness of DD sequences and thereby influence which DD sequence is considered most effective. We find that applying pulses along axes rotated $45°$ relative to the axes of the random magnetic field components does not have a noticeable effect on the average fidelity, for all DD sequences.

Subsequently, we perform the same simulations on a system where the direction of the random magnetic field can vary significantly up to 45°, and where the correlation length is instead 1/4 the shuttling length, such that even during shuttling, we are not in the motional narrowing regime. The results are qualitatively very similar and lead to the same conclusions, most importantly that the XY8-Z sequence is generally the most effective DD sequence for forth-back shuttling.

Finally, we explore the modelling of a specific Ge device but determining a spatially varying deterministic magnetic field $\mathbf{B}_0(x)$, using an experimentally found spatially varying Larmor frequency. We discover that the effectiveness of DD sequences at suppressing decoherence of a spin initialised along the x-axis can vary significantly depending on the specific shuttling parameters. We find that often DD sequences are effective at suppressing decoherence, and that the XY8-X and XY8-Z are generally among the best performing DD sequences, even in the case where the deterministic magnetic field varies significantly.

8.1 Outlook

There are a plethora of avenues for future research that naturally extend from this work, many of which can be explored using the framework we have developed.

For the more exploratory work performed in Chapter 7, it would be insightful to analyse the average fidelity when we account for the deterministic magnetic field. While we cannot perfectly accommodate for the deterministic magnetic field (as it does not commute with the random component of the magnetic field), it may still be interesting to perform a pseudo-inverse rotation to account for the deterministic magnetic field, and see if the average fidelity follows a decay curve similar to the other models we analysed. Furthermore, this makes the results agnostic of the initial state.

An intriguing investigation would involve simulating a two-qubit operation with shuttling. A ZZ-type two-qubit operation commutes with a random magnetic field along the z-axis, such that the effectiveness of the operation is not affected. However, it would be interesting to analyse the fidelity of a *shuttling + gate* operation in the case where the random magnetic field is 3D. The effectiveness of DD sequences in this case would also be very interesting.

Alternatively, one could look at alternative noise models for the underlying random sheet. A natural choice would be to look at $1/f$ noise to model the charge noise, which is predicted to be a limiting factor for decoherence in Ge. Furthermore, while we briefly covered it in this thesis, having the spatial correlations decay according to a Gaussian rather than an exponential may lead to more interesting characteristics.

While we have looked at certain developed DD sequences for a specific forth-back shuttling route, there may be more DD sequences that prove even more effective for shuttling. It is also likely that different shuttling routes will lead to different conclusions. This is also applicable to the idea of implementing qubit encodings where multiple spins constitute one logical qubit. This includes the effectiveness of different encodings during shuttling, which extends to an analysis of an optimised shuttling procedure (sequential or parallel shuttling, shuttling delay).

If one desired to model the same scenarios but include more realism, one could look at how the pulses in DD sequences are implemented. The pulses could be more realistically modelled by involving driving over a period of time according to

a specific shape, which requires the spin to be stationary for a certain waiting time during the shuttling, and may involve a pulse error. It would be interesting to observe if the DD sequences still show effectiveness when these faults are included. One could also look at the relationship between the magnetic field and the g-tensor. The g-tensor in Ge is actively being studied, and future research may inspire different ways to model the Hamiltonian affecting a qubit during shuttling, while retaining the aspects that make it possible to simulate during shuttling.

Finally, while the DD sequences we have investigated have demonstrated their effective during simulations of shuttling, it is yet to be seen if the same effectiveness is observed in an experiment.

Bibliography

[1] M. Kjaergaard, M. E. Schwartz, J. Braumüller, P. Krantz, J. I.-J. Wang, S. Gustavsson, and W. D. Oliver. Superconducting qubits: Current state of play. *Annual Review of Condensed Matter Physics*, 11(Volume 11, 2020):369–395, 2020.

[2] L. Childress and R. Hanson. Diamond NV centers for quantum computing and quantum networks. *MRS Bulletin*, 38(2):134–138, 2013.

[3] R. Debroux, C. P. Michaels, C. M. Purser, N. Wan, M. E. Trusheim, J. Arjona Martínez, R. A. Parker, A. M. Stramma, K. C. Chen, L. De Santis, et al. Quantum control of the tin-vacancy spin qubit in diamond. *Physical Review X*, 11(4):041041, 2021.

[4] C. D. Bruzewicz, J. Chiaverini, R. McConnell, and J. M. Sage. Trapped-ion quantum computing: Progress and challenges. *Applied physics reviews*, 6(2), 2019.

[5] L. Henriet, L. Beguin, A. Signoles, T. Lahaye, A. Browaeys, G.-O. Reymond, and C. Jurczak. Quantum computing with neutral atoms. *Quantum*, 4:327, 2020.

[6] M. E. Beverland, P. Murali, M. Troyer, K. M. Svore, T. Hoefler, V. Kliuchnikov, G. H. Low, M. Soeken, A. Sundaram, and A. Vaschillo. Assessing requirements to scale to practical quantum advantage. *arXiv preprint arXiv:2211.07629*, 2022.

[7] D. Castelvecchi. IBM releases first-ever 1,000-qubit quantum chip. *Nature*, 624(7991):238, December 2023.

[8] L. M. K. Vandersypen and M. A. Eriksson. Quantum computing with semiconductor spins. *Physics Today*, 72(8):38–45, 2019.

[9] A. Chatterjee, P. Stevenson, S. De Franceschi, A. Morello, N. P. de Leon, and F. Kuemmeth. Semiconductor qubits in practice. *Nature Reviews Physics*, 3(3):157–177, 2021.

[10] E. Kawakami, T. Jullien, P. Scarlino, D. R. Ward, D. E. Savage, M. G. Lagally, V. V. Dobrovitski, M. Friesen, S. N. Coppersmith, M. A. Eriksson, et al. Gate fidelity and coherence of an electron spin in an Si/SiGe quantum dot with micromagnet. *Proceedings of the National Academy of Sciences*, 113(42):11738–11743, 2016.

[11] A. R. Mills, C. R. Guinn, M. J. Gullans, A. J. Sigillito, M. M. Feldman, E. Nielsen, and J. R. Petta. Two-qubit silicon quantum processor with operation fidelity exceeding 99%. *Science Advances*, 8(14):eabn5130, 2022.

[12] C. H. Yang, R. C. C. Leon, J. C. C. Hwang, A. Saraiva, T. Tanttu, W. Huang, J. Camirand Lemyre, K. W. Chan, K. Y. Tan, F. E. Hudson, et al. Operation of a silicon quantum processor unit cell above one kelvin. *Nature*, 580(7803):350–354, 2020.

[13] F. van Riggelen-Doelman. *Distributing quantum information with holes in germanium*. PhD thesis, Delft University of Technology, 2024.

[14] L. M. K. Vandersypen, H. Bluhm, J. S. Clarke, A. S. Dzurak, R. Ishihara, A. Morello, D. J. Reilly, L. R. Schreiber, and M. Veldhorst. Interfacing spin qubits in quantum dots and donors—hot, dense, and coherent. *npj Quantum Information*, 3(1):34, 2017.

[15] I. Seidler, T. Struck, R. Xue, N. Focke, S. Trellenkamp, H. Bluhm, and L. R. Schreiber. Conveyor-mode single-electron shuttling in Si/SiGe for a scalable quantum computing architecture. *npj Quantum information*, 8(1):100, 2022.

[16] A. M. J. Zwerver, S. V. Amitonov, S. L. de Snoo, M. T. Mądzik, M. Rimbach-Russ, A. Sammak, G. Scappucci, and L. M. K. Vandersypen. Shuttling an electron spin through a silicon quantum dot array. *PRX Quantum*, 4:030303, Jul 2023.

[17] M. De Smet, Y. Matsumoto, A.-M. J. Zwerver, L. Tryputen, S. L. de Snoo, S. V. Amitonov, A. Sammak, N. Samkharadze, Ö. Gül, R. N. M. Wasserman, et al. High-fidelity single-spin shuttling in silicon. *arXiv preprint arXiv:2406.07267*, 2024.

[18] F. van Riggelen-Doelman, C.-A. Wang, S. L. de Snoo, W. I. L. Lawrie, N. W. Hendrickx, M. Rimbach-Russ, A. Sammak, G. Scappucci, C. Déprez, and M. Veldhorst. Coherent spin qubit shuttling through germanium quantum dots. *Nature Communications*, 15(1):5716, 2024.

[19] A. S. Mokeev, Y.-N. Zhang, and V. V. Dobrovitski. Modeling of decoherence and fidelity enhancement during transport of entangled qubits. *arXiv preprint arXiv:2409.04404*, 2024.

[20] P. Huang and X. Hu. Spin qubit relaxation in a moving quantum dot. *Physical Review B—Condensed Matter and Materials Physics*, 88(7):075301, 2013.

[21] F. Ginzel, A. R. Mills, J. R. Petta, and G. Burkard. Spin shuttling in a silicon double quantum dot. *Phys. Rev. B*, 102:195418, Nov 2020.

[22] V Langrock, J. A. Krzywda, N. Focke, I. Seidler, L. R. Schreiber, and Ł. Cywiński. Blueprint of a scalable spin qubit shuttle device for coherent mid-range qubit transfer in disordered Si/SiGe/SiO_2. *PRX Quantum*, 4(2):020305, 2023.

[23] S. Bosco, J. Zou, and D. Loss. High-fidelity spin qubit shuttling via large spin-orbit interactions. *PRX Quantum*, 5:020353, Jun 2024.

[24] Y.-N. Zhang and V.V. Dobrovitski. Optimized shuttling of entangled qubits in decoherence-free subspace. (To be published).

[25] Y.-N. Zhang, A. S. Mokeev, and V. V. Dobrovitski. Shuttling-assisted dynamical decoupling: Protect qubit by exploiting non-stationary 1/f noise during spin shuttling. (To be published).

[26] QuTech/Quantum Inspire. Bloch sphere. https://www.quantum-inspire.com/kbase/blochsphere/. [Accessed 28-06-2025].

[27] C. Kittel. *Quantum theory of solids*. Wiley, 1963.

[28] Princeton. Silicon, Si. https://www.princeton.edu/~maelabs/mae324/glos324/silicon.htm. [Accessed 06-06-2025].

[29] J. R. Chelikowsky and M. L. Cohen. Erratum: Nonlocal pseudopotential calculations for the electronic structure of eleven diamond and zinc-blende semiconductors. *Physical Review B*, 30(8):4828, 1984.

[30] E. Suvar. *SiGeC Heterojunction Bipolar Transistors*. PhD thesis, KTH Microelectronics and Information Technology, 2003.

[31] R. M. White and B. Bayne. *Quantum theory of magnetism*, volume 1. Springer, 1983.

[32] R. Winkler. *Spin-orbit coupling effects in two-dimensional electron and hole systems*, volume 191. Springer, 2003.

[33] G. Scappucci, C. Kloeffel, F. A. Zwanenburg, D. Loss, M. Myronov, J.-J. Zhang, S. De Franceschi, G. Katsaros, and M. Veldhorst. The germanium quantum information route. *Nature Reviews Materials*, 6(10):926–943, 2021.

[34] B. I. Shklovskii and A. L. Efros. *Electronic properties of doped semiconductors*, volume 45. Springer Science & Business Media, 2013.

[35] J. M. Luttinger and W. Kohn. Motion of electrons and holes in perturbed periodic fields. *Physical Review*, 97(4):869, 1955.

[36] Y. U. Peter and M. Cardona. *Fundamentals of semiconductors: physics and materials properties*. Springer Science & Business Media, 2010.

[37] C. H. Yang, A. Rossi, R. Ruskov, N. S. Lai, F. A. Mohiyaddin, S. Lee, C. Tahan, G. Klimeck, A. Morello, and A. S. Dzurak. Spin-valley lifetimes in a silicon quantum dot with tunable valley splitting. *Nature communications*, 4(1):2069, 2013.

[38] C. Tahan and R. Joynt. Relaxation of excited spin, orbital, and valley qubit states in ideal silicon quantum dots. *Physical Review B*, 89(7):075302, 2014.

[39] W. I. L. Lawrie. *Spin Qubits in Silicon and Germanium*. PhD thesis, Delft University of Technology, 2022.

[40] L. A. Terrazos, E. Marcellina, Z. Wang, S. N. Coppersmith, M. Friesen, A. R. Hamilton, X. Hu, B. Koiller, A. L. Saraiva, D. Culcer, et al. Theory of hole-spin qubits in strained germanium quantum dots. *Physical Review B*, 103(12):125201, 2021.

[41] N. W. Hendrickx. *Qubit arrays in germanium*. PhD thesis, Delft University of Technology, 2021.

[42] J. H. Qvist and J. Danon. Anisotropic g-tensors in hole quantum dots: Role of transverse confinement direction. *Physical Review B*, 105(7):075303, 2022.

[43] N. W. Hendrickx, L. Massai, M. Mergenthaler, F. J. Schupp, S. Paredes, S. W. Bedell, G. Salis, and A. Fuhrer. Sweet-spot operation of a germanium hole spin qubit with highly anisotropic noise sensitivity. *Nature Materials*, 23(7):920–927, 2024.

[44] Z. Cai, A. Siegel, and S. Benjamin. Looped pipelines enabling effective 3d qubit lattices in a strictly 2d device. *PRX Quantum*, 4:020345, Jun 2023.

[45] W. Zhang, N. Konstantinidis, K. A. Al-Hassanieh, and V. V. Dobrovitski. Modelling decoherence in quantum spin systems. *Journal of Physics: Condensed Matter*, 19(8):083202, 2007.

[46] N. G. van Kampen. *Stochastic Processes in Physics and Chemistry*. Elsevier Science Publishers, Amsterdam, 1992.

[47] J. L. Doob. The Brownian movement and stochastic equations. *Annals of Mathematics*, 43(2):351–369, 1942.

[48] A. S. Mokeev and V. V. Dobrovitski. Shuttling of the electron spin in the magnetic field with varying direction. Unpublished work, 2025.

[49] C. P. Slichter. *Principles of magnetic resonance*, volume 1. Springer Science & Business Media, 2013.

[50] A. Brinkmann. Introduction to average Hamiltonian theory. i. basics. *Concepts in Magnetic Resonance Part A*, 45(6):e21414, 2016.

[51] E. L. Hahn. Spin echoes. *Physical review*, 80(4):580, 1950.

[52] V. V. Dobrovitski. Lecture notes - Qubit dynamics & Quantum control.

[53] T. Gullion, D. B. Baker, and M. S. Conradi. New, compensated carr-purcell sequences. *Journal of Magnetic Resonance (1969)*, 89(3):479–484, 1990.

[54] G. De Lange, Z.-H. Wang, D. Riste, V. V. Dobrovitski, and R Hanson. Universal dynamical decoupling of a single solid-state spin from a spin bath. *Science*, 330(6000):60–63, 2010.

[55] M. P. Losert, M. A. Eriksson, R. Joynt, R. Rahman, G. Scappucci, S. N. Coppersmith, and M. Friesen. Practical strategies for enhancing the valley splitting in si/sige quantum wells. *Physical Review B*, 108(12):125405, 2023.

[56] C. Déprez, M. Bassi, and Z. Ademi. Private communication, March 2025. Veldhorst group, QuTech, TU Delft.

[57] Z.-H. Wang, G. De Lange, D. Ristè, R. Hanson, and V. V. Dobrovitski. Comparison of dynamical decoupling protocols for a nitrogen-vacancy center in diamond. *Physical Review B—Condensed Matter and Materials Physics*, 85(15):155204, 2012.

Appendix A

Supplementary derivations

A.1 Decoherence due to a static random field

Suppose we have the Hamiltonian

$$H = \tilde{\mathbf{B}} \cdot \mathbf{S} \tag{A.1}$$

where the magnetic field $\tilde{\mathbf{B}} = (\tilde{B}_x, \tilde{B}_y, \tilde{B}_z)$ is a 3-component multivariate random normal distribution with each component having mean 0 and variance σ^2.

For a single realisation of the magnetic field $\boldsymbol{\beta}$, we can write the evolution operator as

$$U(t) = \cos(\theta) - i\sin(\theta)\boldsymbol{\sigma} \cdot \hat{\boldsymbol{n}} \tag{A.2}$$

where $\theta = \frac{1}{2}t|\boldsymbol{\beta}|$, and $\hat{\mathbf{n}} = (n_x, n_y, n_z)$, where $n_i = \beta_i/|\boldsymbol{\beta}|$. $\boldsymbol{\sigma}$ is the vector of Pauli matrices. This leads to

$$\begin{aligned}
\langle S_x(t)\rangle = \mathrm{Tr}\left(S_x U(t)^\dagger S_x U(t)\right) &= \frac{1}{2}\left(\cos^2(\theta) - \sin^2(\theta)(n_x^2 + n_y^2 - n_z^2)\right) && \text{(A.3)}\\
&= \frac{1}{2}\left(\cos^2(\theta) - \sin^2(\theta)(1 - 2n_z^2)\right) && \text{(A.4)}\\
&= \frac{1}{2}\left(\cos(|\boldsymbol{\beta}|t) + n_z^2 - n_z^2\cos(|\boldsymbol{\beta}|t)\right) && \text{(A.5)}
\end{aligned}$$

where we use that $n_x^2 + n_y^2 + n_z^2 = 1$.

We want to calculate the average projection of the x-component of the spin given by the average over all realisations $W_x = 2\mathbb{E}[\langle S_x(t)\rangle]$. We begin with the easier component, n_z^2. This component is a directional quantity, as n_z depends only on the direction of the randomly sampled β. We use the fact that $n_x^2 + n_y^2 + n_z^2 = 1$ and that n_x, n_y and n_z are independently and identically distributed to deduce that

$$\begin{aligned}
\mathbb{E}[n_x^2] + \mathbb{E}[n_y^2] + \mathbb{E}[n_z^2] &= 1 && \text{(A.6)}\\
\implies 3\mathbb{E}[n_z^2] &= 1 && \text{(A.7)}\\
\implies \mathbb{E}[n_z^2] &= 1/3 && \text{(A.8)}
\end{aligned}$$

Next we have $\cos(|\boldsymbol{\beta}t|)$. The joint probability distributon of $\boldsymbol{\beta}$ is given by a 3D isotropic Gaussian:

$$P(r,\theta,\phi)d^3\boldsymbol{\beta} = \left(\frac{1}{\sqrt{2\pi\sigma^2}}\right)^3 \exp\left(-\frac{r^2}{2\sigma^2}\right)\cdot r^2\sin(\theta)drd\theta d\phi \tag{A.9}$$

with $\beta_x = r\sin(\theta)\cos(\phi),\ \beta_y = r\sin(\theta)\sin(\phi),\ \beta_z = r\cos(\theta)$.

To calculate the expected value $\mathbb{E}[\cos(|\boldsymbol{\beta}|t)]$, we are interested in solving the integral

$$I_1 = \left(\frac{1}{\sqrt{2\pi\sigma^2}}\right)^3 \int_0^\infty r^2 e^{-ar^2}\cos(tr)dr\cdot 4\pi \tag{A.10}$$

with $a = 1/2\sigma^2$, and the 4π results from integration over θ, ϕ. We use derivatives under the integral signs, along with known integrals to derive that

$$I_1 = \sqrt{\frac{2}{\pi}}\frac{1}{\sigma^3}\frac{d}{da}\int_0^\infty -e^{-ar^2}\cos(tr)dr \tag{A.11}$$

$$= \sqrt{\frac{2}{\pi}}\frac{1}{\sigma^3}\frac{d}{da}\left(-\frac{1}{2}\sqrt{\frac{\pi}{a}}e^{-t^2/4a}\right) \tag{A.12}$$

$$= \frac{\sqrt{2}}{2\sigma^3}e^{-t^2/4a}\left(\frac{-1}{2a^{3/2}} + \frac{t^2}{4a^{5/2}}\right) \tag{A.13}$$

$$= e^{-\sigma^2t^2/2}(1-\sigma^2t^2) \tag{A.14}$$

Now all the remains is $\mathbb{E}[n_z^2\cos(|\boldsymbol{\beta}|t)]$, where we use $n_z = \cos(\theta)$ to obtain the integral

$$I_2 = \left(\frac{1}{\sqrt{2\pi\sigma^2}}\right)^3 \int_0^\infty\int_0^\pi r^2 e^{-ar^2}\cos(tr)\cos^2(\theta)\sin(\theta)d\theta dr\cdot 2\pi \tag{A.15}$$

$$= \frac{1}{2}I_1\cdot\int_0^\pi \cos^2(\theta)\sin(\theta)d\theta \tag{A.16}$$

$$= \frac{1}{2}I_1\cdot\frac{2}{3} \tag{A.17}$$

where we use the fact that the integral in r and θ are separable. This results in

$$W_x = \frac{1}{3} + \frac{2}{3}(1-\sigma^2t^2)\exp\left(-\sigma^2t^2/2\right) \tag{A.18}$$

A.2 Matrix exponential

We will prove that for any two matrices A, B we have

$$\exp\left(ABA^{-1}\right) = A\exp(B)A^{-1}. \tag{A.19}$$

By the definition of the matrix exponential we have

$$\exp\left(ABA^{-1}\right) = \sum_{k=0}^{\infty}\frac{1}{k!}(ABA^{-1})^k. \tag{A.20}$$

For each index k in the infinite sum, we have

$$(ABA^{-1})^k = ABA^{-1} \cdot ABA^{-1} \cdot ABA^{-1} \cdot ...(\text{k times}) \tag{A.21}$$
$$= ABIBIB \cdot ...A^{-1} \tag{A.22}$$
$$= AB^kA^{-1}, \tag{A.23}$$

resulting in

$$\exp\big(ABA^{-1}\big) = \sum_{k=0}^{\infty} \frac{1}{k!}(ABA^{-1})^k \tag{A.24}$$
$$= \sum_{k=0}^{\infty} \frac{1}{k!}AB^kA^{-1} \tag{A.25}$$
$$= A\left(\sum_{k=0}^{\infty} \frac{1}{k!}B^k\right)A^{-1} \tag{A.26}$$
$$= A\exp(B)A^{-1} \tag{A.27}$$

as required.

A.3 Average fidelity

We are interested in calculate the average fidelity over all initial states for a given evolution operator U. This means calculating

$$F = \int_{\psi} |\langle\psi|U|\psi\rangle|^2 d\psi \tag{A.28}$$

where the integral is taken uniformly over all possible initial state. This can be treated as an integral taken uniformly over the surface of the Bloch sphere giving

$$F = \frac{1}{4\pi}\int_0^{\pi}\int_0^{2\pi} |\langle\psi|U|\psi\rangle|^2 \sin(\theta) d\phi d\theta \tag{A.29}$$

where $|\psi\rangle = \cos\left(\frac{\theta}{2}\right)|0\rangle + e^{i\phi}\sin\left(\frac{\theta}{2}\right)$. We write the evolution operator as

$$U = \cos\left(\frac{k}{2}\right) - i\sin\left(\frac{k}{2}\right)(n_x\sigma_x + n_y\sigma_y + n_z\sigma_z) \tag{A.30}$$

We compute that

$$\langle\psi|U|\psi\rangle = \cos\left(\frac{k}{2}\right) - i\sin\left(\frac{k}{2}\right)(n_x\sin(\theta)\cos(\phi) + n_y\sin(\theta)\sin(\phi) + n_z\cos(\theta)) \tag{A.31}$$

and

$$|\langle\psi|U|\psi\rangle|^2 = \cos^2\left(\frac{k}{2}\right) + \sin^2\left(\frac{k}{2}\right) \cdot \tag{A.32}$$
$$[n_x^2\sin^2(\theta)\cos^2(\phi) + n_y^2\sin^2(\theta)\sin^2(\phi) + n_z^2\cos^2(\theta) + \tag{A.33}$$
$$2n_xn_y\sin^2(\theta)\sin(\phi)\cos(\phi) + 2n_xn_z\sin(\theta)\cos(\theta)\cos(\phi) \tag{A.34}$$
$$+ 2n_yn_z\sin(\theta)\cos(\theta)\sin(\phi)] \tag{A.35}$$

We use the solve the integrals:

$$I[f(\phi)] \equiv \int_0^{2\pi} f(\phi)d\phi \tag{A.36}$$
$$I[\cos^2(\phi)] = \pi \tag{A.37}$$
$$I[\sin^2(\phi)] = \pi \tag{A.38}$$
$$I[1] = 2\pi \tag{A.39}$$
$$I[\sin(\phi)\cos(\phi)] = I[\cos(\phi)] = I[\sin(\phi)] = 0 \tag{A.40}$$
$$J[g(\theta)] = \int_0^{\pi} g(\theta)\sin(\theta)d\theta \tag{A.41}$$
$$J[\sin^2(\theta)] = \frac{4}{3} \tag{A.42}$$
$$J[\cos^2(\theta)] = \frac{2}{3} \tag{A.43}$$

such that

$$F = \frac{1}{4\pi}\left[4\pi\cos^2\left(\frac{k}{2}\right) + \sin^2\left(\frac{k}{2}\right)\left(\frac{4}{3}\pi n_x^2 + \frac{4}{3}\pi n_y^2 + \frac{2\pi}{3}\cdot 2\pi\cdot n_z^2 +\right)\right] \tag{A.44}$$
$$= \cos^2\left(\frac{k}{2}\right) + \frac{1}{3}\sin^2\left(\frac{k}{2}\right) \tag{A.45}$$

where we use that $n_x^2 + n_y^2 + n_z^2 = 1$. Continuing,

$$F = \frac{1}{3} + \frac{2}{3}\cos^2\left(\frac{k}{2}\right) \tag{A.46}$$
$$= \frac{1}{3} + \frac{1}{6}\left(4\cos^2\left(\frac{k}{2}\right)\right) \tag{A.47}$$
$$= \frac{1}{3} + \frac{1}{6}|\mathrm{Tr}(U)|^2 \tag{A.48}$$

allowing us to easily calculate the average fidelity over all initial state for a given evolution operator U.

A.4 AHT with waiting times

We consider the following adjusted sequences, based on XY8, XY8-X, XY8-Z sequences, where a waiting time t_w is included either side of the midpoint of the evolution:

$$\begin{aligned}\mathrm{XY8}_w \equiv{}& (\tau - X - 2\tau - Y - 2\tau - X - 2\tau - Y - \tau) - 2t_w \\ &- (\tau - Y - 2\tau - X - 2\tau - Y - 2\tau - X - \tau),\end{aligned} \tag{A.49}$$
$$\begin{aligned}\mathrm{XY8\text{-}X}_w \equiv{}& (\tau - X - 2\tau - Y - 2\tau - X - 2\tau - Y - \tau) - t_w - X - t_w \\ &- (\tau - Y - 2\tau - X - 2\tau - Y - 2\tau - X - \tau) - X,\end{aligned} \tag{A.50}$$
$$\begin{aligned}\mathrm{XY8\text{-}Z}_w \equiv{}& (\tau - X - 2\tau - Y - 2\tau - X - 2\tau - Y - \tau) - t_w - Z - t_w \\ &- (\tau - Y - 2\tau - X - 2\tau - Y - 2\tau - X - \tau) - Z.\end{aligned} \tag{A.51}$$

The resulting toggling frame is shown in Tab. A.1. We observe that the first order effective Hamiltonian is non-zero for all three sequences. This is equivalent to considering the first-order effective Hamiltonian over the shuttling component of the sequence and the stationary component of the sequence separately.

Table A.1: Toggling frame during the $XY4_w$, $XY4\text{-}X_w$, and $XY4\text{-}Z_w$ pulse sequence. During shuttling, we distinguish between the toggling frame in the forward half (Blue) and the backwards half (Red). Summing up the terms in a column gives the first-order effective Hamiltonian.

		XY8			XY8-X			XY8-Z		
	Duration	H_x	H_y	H_z	H_x	H_y	H_z	H_x	H_y	H_z
	τ	+	+	+	+	+	+	+	+	+
	2τ	+	-	-	+	-	-	+	-	-
	2τ	-	-	+	-	-	+	-	-	+
	2τ	-	+	-	-	+	-	-	+	-
	τ	+	+	+	+	+	+	+	+	+
	t_w	+	+	+	+	+	+	+	+	+
	t_w	+	+	+	+	-	-	-	-	+
	τ	+	+	+	+	-	-	-	-	+
	2τ	-	+	-	-	-	+	+	-	-
	2τ	-	-	+	-	+	-	+	+	+
	2τ	+	-	-	+	+	+	-	+	-
	τ	+	+	+	+	-	-	-	-	+
Total	$16\tau + 2t_w$	$2t_wH_x$	$2t_wH_y$	$2t_wH_z$	$2t_wH_x$	0	0	0	0	$2t_wH_z$

Appendix B

Supplementary figures

B.1 Shuttling fidelity

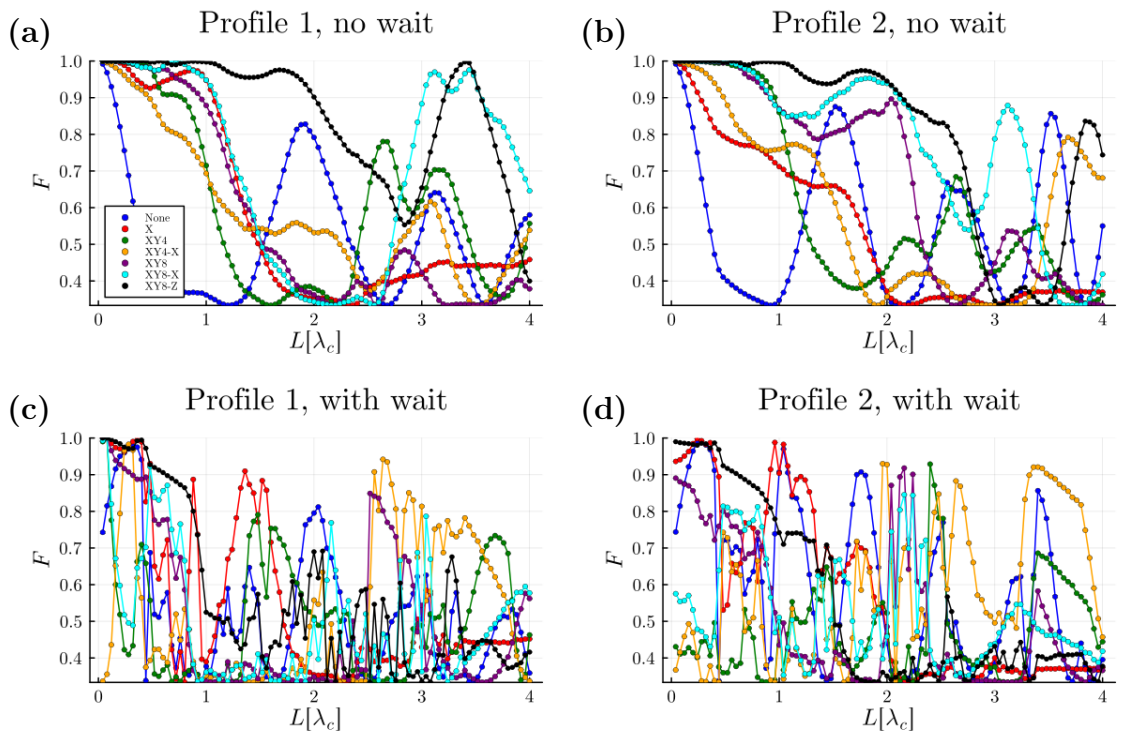

Figure B.1: Dependence of average fidelity F, measured at the end of a forth-back shuttling path, on the **shuttling length** L in different scenarios. During shuttling, the spin travels at a constant speed v, except when it is stationary for a duration $2t_w$ at $x = L =$. These figures involve **fast shuttling** with $v = 120\lambda_c/\tau_c$. The random magnetic field acting on the spin is given by the Hamiltonian in Eq. (7.3), with $\mathbf{B}_0(x)$ a profile-specific position-dependent deterministic magnetic field on the profile. **(a)**, **(c)** use Profile 1, with **(c)** containing an inset of the profile. **(b)**, **(d)**, use Profile 2, with **(d)** containing an inset of the profile. Parameters are listed in Tab. 7.1. Legend in **(a)** applies to all figures. **(a)**, **(b)**: no waiting time ($t_w = 0$). **(c)**, **(d)**: Includes waiting time $t_w = (1/60)\tau_c$. Results generated using $N = 1600$, $M = 10^2$. Error bars are shown in each figure, though may be too small to be visible.

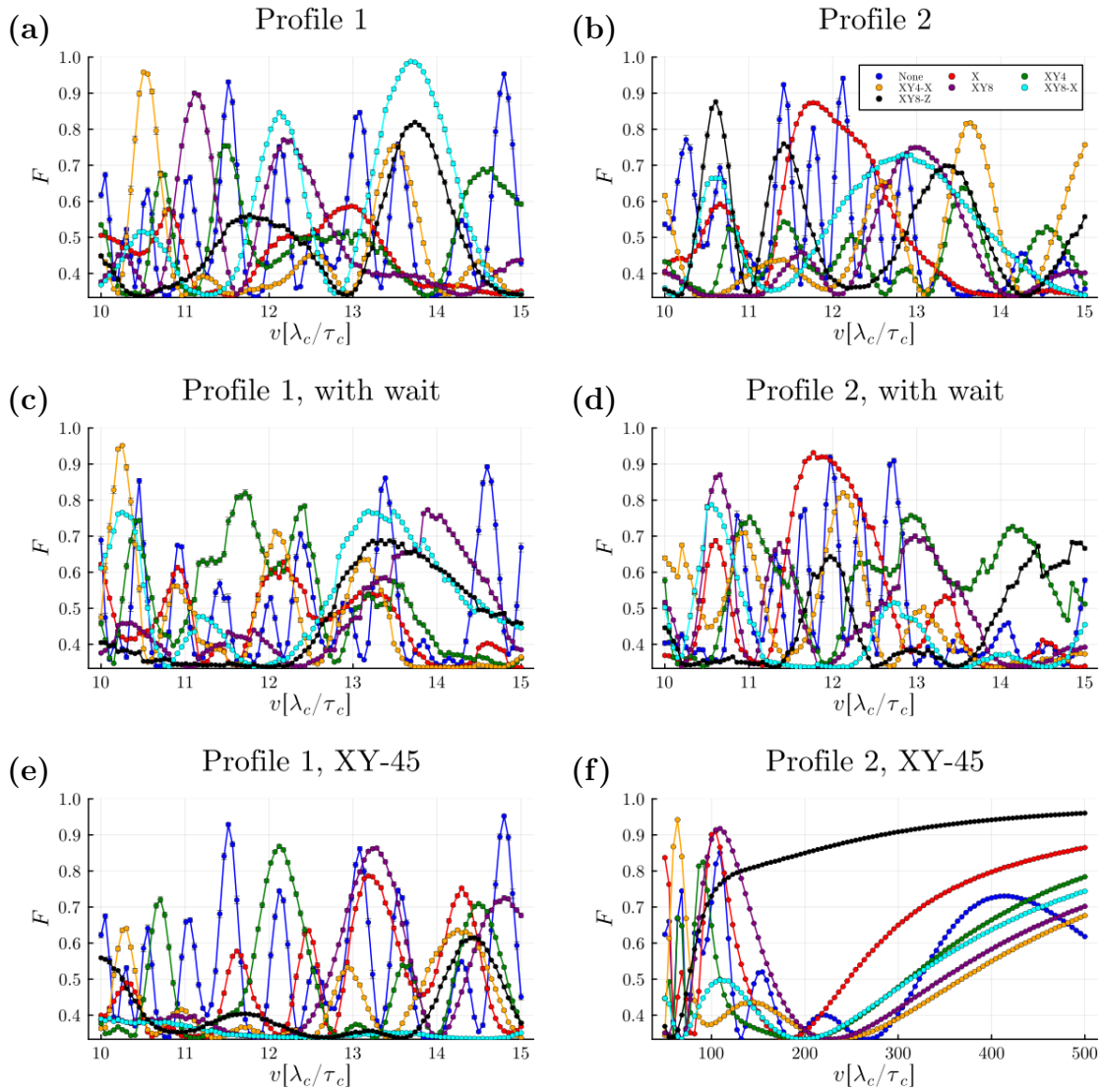

Figure B.2: Dependence of average fidelity F, measured at the end of a forth-back shuttling path, on the **shuttling velocity** $v = L/T$ in different scenarios. These figures focus on **slow shuttling velocities**. During shuttling, the spin travels at a constant speed v, except when it is stationary for a duration $2t_w$ at $x = L = 4\lambda_c$. The random magnetic field acting on the spin is given by the Hamiltonian in Eq. (7.3), with $\mathbf{B}_0(x)$ a profile-specific position-dependent deterministic magnetic field on the profile. Profile 1 and profile 2 are presented in Fig. 7.8. **(a)**, **(c)**, **(e)** use Profile 1. **(b)**, **(d)**, **(f)** use Profile 2. Parameters are listed in Tab. 7.1. Legend in **(a)** applies to all figures. **(a)**, **(b)**: no waiting time ($t_w = 0$). **(c)**, **(d)**: Includes waiting time $t_w = (1/60)\tau_c$. **(e)**, **(f)**: no waiting time ($t_w = 0$), but X and Y pulse axes in DD sequences are rotated 45°. Results generated using $N = 1600$, $M = 10^2$. Error bars are shown in each figure, though may be too small to be visible

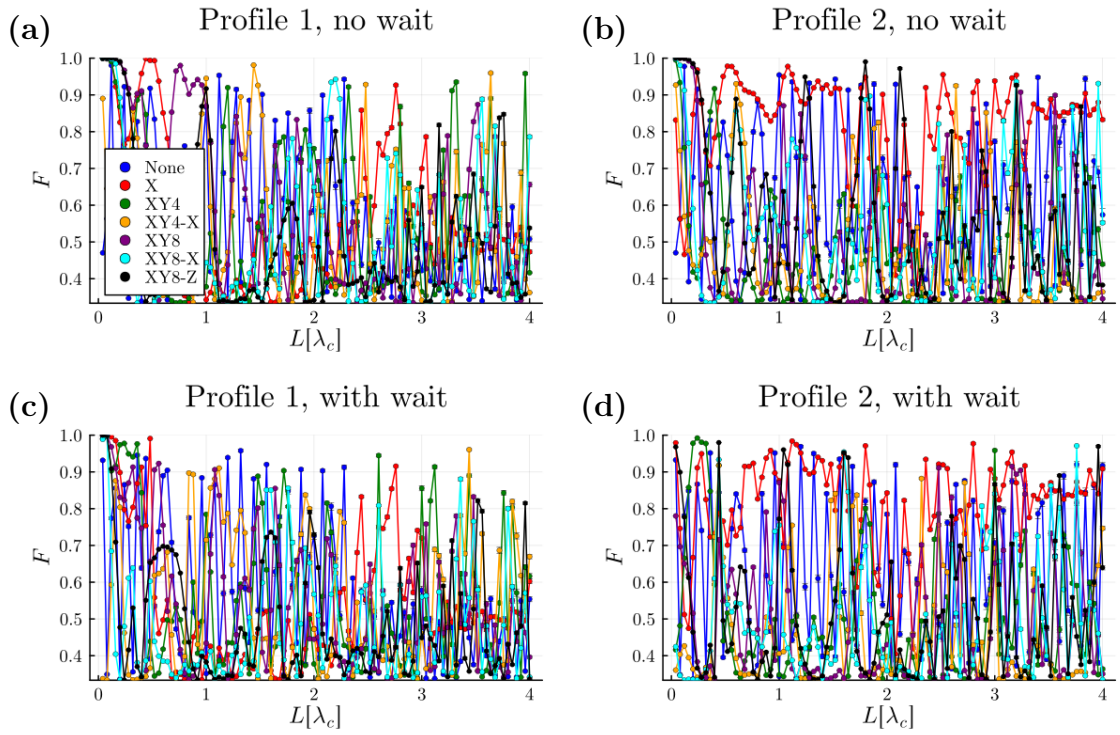

Figure B.3: Dependence of average fidelity F, measured at the end of a forth-back shuttling path, on the **shuttling length** L in different scenarios. During shuttling, the spin travels at a constant speed v, except when it is stationary for a duration $2t_w$ at $x = L =$. These figures involve **slow shuttling** with $v = 12\lambda_c/\tau_c$. The random magnetic field acting on the spin is given by the Hamiltonian in Eq. (7.3), with $\mathbf{B}_0(x)$ a profile-specific position-dependent deterministic magnetic field on the profile. **(a)**, **(c)** use Profile 1, with **(c)** containing an inset of the profile. **(b)**, **(d)**, use Profile 2, with **(d)** containing an inset of the profile. Parameters are listed in Tab. 7.1. Legend in **(a)** applies to all figures. **(a)**, **(b)**: no waiting time ($t_w = 0$). **(c)**, **(d)**: Includes waiting time $t_w = (1/60)\tau_c$. Results generated using $N = 1600$, $M = 10^2$. Error bars are shown in each figure, though may be too small to be visible

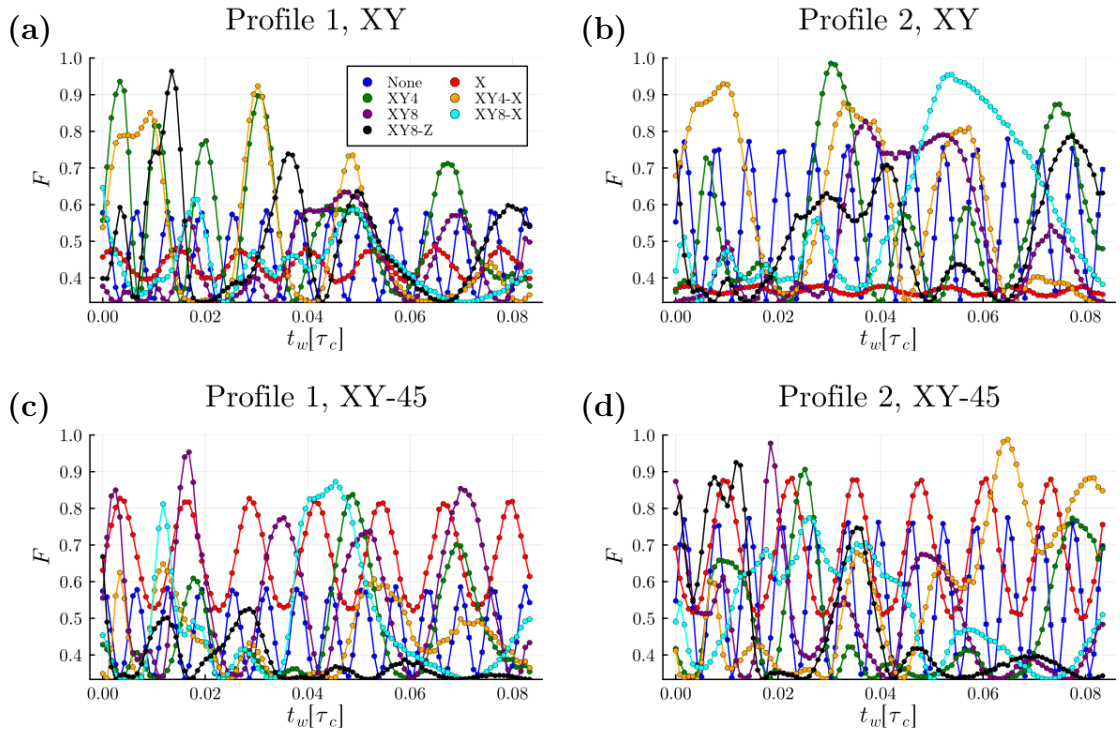

Figure B.4: Dependence of decoherence W of a spin initialised along the x-axis, measured at the end of a forth-back shuttling path, on the **waiting time** t_w in different scenarios. During shuttling, the spin travels at a constant speed $v = L/T$, with $L = 4\lambda_c$ the shuttling length and T the shuttling time, except when it is stationary for a duration $2t_w$ at $x = L$. These figures involve **slow shuttling** with $v = 12\lambda_c/\tau_c$. The random magnetic field acting on the spin is given by the Hamiltonian in Eq. (7.3), with $\mathbf{B}_0(x)$ a profile-specific position-dependent deterministic magnetic field on the profile. Profile 1 and profile 2 are presented in Fig. 7.8. **(a)**, **(c)** use Profile 1 **(b)**, **(d)**, use Profile 2. Parameters are listed in Tab. 7.1. Legend in **(a)** applies to all figures. **(a)**, **(b)**: X, Y pulses in the DD sequences are along the x- and y-axis. **(c)**, **(d)**: X, Y pulses in the DD sequences are along the lines $[1, 1, 0]$ and $[1, -1, 0]$ respectively. Results generated using $N = 1600$, $M = 10^2$. Error bars are shown in each figure, though may be too small to be visible.